POLITECNICO
MILANO 1863

SCUOLA DI INGEGNERIA INDUSTRIALE
E DELL'INFORMAZIONE

Expansion of the coupled solar radiation pressure-J_2 Hamiltonian model to account for the Sun gravitational perturbation and applications

Tesi di Laurea Magistrale in
Space Engineering - Ingegneria Spaziale

Author: **Andrea Cecconello**

Student ID: 970185
Advisor: Prof. Camilla Colombo
Co-advisors: Andrea Muciaccia
Academic Year: 2021-2022

Acknowledgements

I would like to express my sincere gratitude to my supervisor professor Camilla Colombo and co-supervisor Andrea Muciaccia, for their assistance at every stage of this research project an for her insightful comments and suggestions that made this thesis work scientifically valuable. My gratitude extends to the Department of Aerospace Science and Technology. It is the help and support of all the professors I had the pleasure to study with that have made my experience in Politecnico di Milano a wonderful time. I offer my special thanks to my friends and colleagues who accompanied me during the bachelor and master's degree years. Especially, I would like to thank Manfredi C., Davide D. Enrico B., and Gabriele D. I hope to share with you countless good moments as it was for all this years. I would like to thanks also my roommate Giuseppe C. for his support during our exams session and funny moments.

Thanks also to all my friends Giovanni, Sara, Beppe, Jessica, Mattia, Tullio, Jacopo, Anna, Nicolas, Pietro, Marta, Matilde, Simone, Alessandro, and Andrea from Pordenone city, for the many good moments passed together in that boring city.

I would also want to express my gratitude to my partner, Dora, for her support and encouragement throughout the last two years and through the various shifts in the focus of the thesis.

I would want to express my gratitude, in particular, to my family. I'd want to express my gratitude to my parents, Cinzia and Luca, for always having understanding and for allowing me to choose my own route. You will always have my admiration, and it would be a privilege for me to one day be able to say that I am like you. I want to express my gratitude to my grandparents, Tina and Bruno, for remembering me as often as they do themselves.

Abstract

The population of debris with High Area-To-Mass ratio (HAMR) is thought to have origins in the Geostationary Earth Orbit (GEO) region, proven by optical observations of space debris using a 1 m Ritchey-Chrétien telescope on Tenerife (Canary Islands). Many of these objects, with apparent area-to-mass ratios of up to 30 m^2/kg are not yet characterise. The orbits of HAMR objects are highly perturbed due to the combined effect of Solar Radiation Pressure (SRP), anomalies of the Earth gravitational field, and third-body gravitational interactions induced by the Sun and the Moon. Space situational awareness requires a comprehensive comprehension of their nature, orbital evolution, and possible origin. Considering both short- and long-period terms, the study of the orbital evolution of HAMR objects necessitates numerical integration of a precise set of differential equations and the investigation of a wide range of possible parameter values. However, such computations become prohibitively expensive when applied continuously over decades, as is required for HAMR debris.

Consequently, it is useful to investigate the equations that regulate the long-term behavior of orbits; such equations can be derived using the averaging method. Recent research has shown that a model based on singly-averaged equations of motion can be used to characterize the dynamics caused by the planetary oblateness in conjunction with the solar radiation pressure. However, this hypothesis, is valid within a certain range of altitude, inclination, eccentricity and for extremely high value of AMR ratio. The main scope of this thesis is to extend the state-of-art modeling by including also the effect of Sun gravitational perturbation on the dynamical evolution. The coupled perturbations affect the evolution of the eccentricity, inclination and orientation of the orbit with respect to the Sun–Earth line. Resonant interactions lead to non-trivial orbital evolution that can be exploited in mission design, however, the dynamics in the vicinity of each resonance can be analytically described by an extended resonant model that provides the location of the central and hyperbolic invariant manifolds which drive the phase space evolution. Once the new Hamiltonian model has been derived exploiting the same resonant term of the third-body perturbation of the Sun and the SRP, the classical tools of the dynamical systems theory can be applied to perform a complete dynamical analysis of the system.

At the end, exploiting the peculiar double-lobe phase space portrait induced by the gravitational perturbation of the Sun, we have derived conditions for resonance trapping of space debris as well as for spacecraft de-orbiting design.

Keywords: High Area-To-Mass ratio; Solar Radiation Pressure; Third-body perturbation; solar sails; Andoyer model;

Sommario

I detriti spaziali aventi un elevato rapporto tra area e massa (HAMR) sono ritenuti aver origine nella regione delle orbite terrestri geostrazionarie (GEO), dimostrato da osservazioni ottiche utilizzando un telescopio Ritchey-Chrétien di 1 m presso Tenerife (Isole Canarie). Molti di questi oggetti aventi rapporti area-massa fino a 30 m^2/kg non sono caratterizzati. Le orbite degli oggetti con HAMR sono fortemente perturbate dall'effetto combinato della pressione della radiazione solare (SRP), delle anomalie del campo gravitazionale della Terra e delle interazioni gravitazionali del terzo corpo indotte dal Sole e dalla Luna. Una solida comprensione della loro natura, evoluzione orbitale e possibile origine è fondamentale per la comprensione della loro distribuzione dello spazio. Lo studio dell'evoluzione orbitale degli oggetti aventi HAMR, tenendo conto sia dei termini di breve periodo che di lungo periodo, richiede una precisa integrazione numerica di sistemi di equazioni differenziali, e l'indagine di una vasta gamma di possibili valori dei parametri fisici e orbitali. Tuttavia, tali calcoli diventano computazionalmente costosi quando vengono applicati continuamente per un periodo di diversi decenni, come è necessario nel caso di detriti con HAMR.

E' pertanto ragionevole indagare le equazioni che governano il comportamento a lungo termine delle orbite; tali equazioni possono essere derivate dal metodo della mediazione dell'anomalia media dell'oggetto. Recenti lavori hanno dimostrato che la dinamica causata dall' oblateness terrestre accoppiata con la pressione della radiazione solare può essere descritta attraverso un modello basato sulla mediazione. Tuttavia, questa ipotesi è valida entro un certo intervallo di altitudine, inclinazione, eccentricità e per un valore estremamente alto del rapporto AMR. L'ambito principale di questa tesi è quello di estendere la modellazione includendo l'effetto della perturbazione gravitazionale del Sole sull'evoluzione della dinamica orbitale. Le perturbazioni accoppiate influenzano l'evoluzione dell'eccentricità, dell'inclinazione e dell'orientamento dell'orbita rispetto all'asse Sole-Terra. Le interazioni risonanti portano ad un'evoluzione orbitale non triviale che può essere sfruttata nella progettazione della missione, tuttavia, la dinamica nelle vicinanze di ciascuna risonanza può essere descritta analiticamente da un modello a singola risonanza esteso che fornisce la posizione dei punti di equilibrio e delle orbite che guidano l'evoluzione dello spazio delle fasi.

Una volta che il nuovo modello di Hamilton è stato derivato sfruttando lo stesso termine di risonanza della perturbazione del terzo corpo del Sole e del SRP, gli strumenti classici della teoria dei sistemi dinamici possono essere applicati per eseguire un'analisi dinamica completa del sistema. Alla fine, sfruttando il peculiare spazio delle fasi a fase doppia indotto dalla perturbazione gravitazionale del Sole, abbiamo derivato le condizioni per la cattura in risonanza dei detriti spaziali così come per la progettazione del de-orbiting di satelliti fuori uso.

Parole chiave: High Area-To-Mass ratio; pressione della radiazione solare; Perturbazione del terzo corpo; vele solari; modello di Andoyer;

Contents

List of Figures

List of Tables

List of Symbols

Variable	Description	SI unit
A	area	m^2
m	mass	kg
σ	area-to-mass ratio	m^2/kg
a	semimajor-axis	km
e	eccentricity	-
i	inclination	rad
f	true anomaly	rad
Ω	Right Ascension of the Ascending Node	rad
ω	Anomaly of the pericenter	rad
$P_\odot$	Solar constant at 1 AU	N/m^2
c_R	object reflectivity	-
n	orbital mean motion of Sun or S/C	rad/s
R	radius	km
r	position	km
v	velocity	km/s
ε	inclination of ecliptic plane	rad
J_2	Earth oblateness	-
N	Number	-
$\odot$	Sun	-
$\oplus$	Earth	-
ψ	longitude of the periapsis	rad
j	resonance	-
$\mathcal{H}$	Hamiltonian	km^2/s^2
$\mathcal{L}$	Lagrangian	km^2/s^2
$\mathcal{T}$	Kinetic energy	km^2/s^2
$\mathcal{V}$	Potential energy	km^2/s^2
$\mathcal{R}$	Perturbing function	km^2/s^2

Acronyms

Acronyms	Definition
AMR	Area Mass Ratio
HAMR	High Area Mass Ratio
GEO	Geostationary Earth Orbit
MEO	Mean Earth Orbit
LEO	Low Earth Orbit
TLE	Two-Lines Element
CNES	France space center
SRP	Solar Radiation Pressure
GNSS	Global Navigation Satellite System
GPS	Global Positioning System
MLI	Multi-Layer Insulator

1 | Introduction

The population of debris with High Area Mass Ratio (HAMR) is thought to have origins in the Geostationary Earth Orbit (GEO) region (formulated by Liou and Weaver [1], Anselmo and Pardini [2], Valk et al. [3], Lemaitre et al. [4], Rosengren and Scheeres [5]), proven by optical observations of space debris using a 1 m Ritchey-Chrétien telescope on Tenerife (Canary Islands, by Schildknecht et al. [6]). Many of these objects, with apparent Area Mass Ratios (AMR) of up to 30 m^2/kg are not yet characterised. Paint flakes and Multi-Layer Insulator (MLI) fragments were identified as potential sources for much larger populations of HAMR debris (see Flegel [7], Drolshagen et al. [8]). The orbits of HAMR objects are highly perturbed due to the combined effect of Solar Radiation Pressure (SRP), anomalies of the Earth gravitational field, and third-body gravitational interactions induced by the Sun and the Moon (see Anselmo and Pardini [2]). Knowing their nature, orbital evolution, and possible origin is critical for space situational awareness because it allows to accurately foreseen their spatial evolution in time and, if possible, find regions of the space where they tend to accumulate due to the interaction between the aforementioned perturbations. The study of the orbital evolution of HAMR objects, taking into account both short-period and long-period terms, requires numerical integration of the precise set of differential equations, and the investigation of a broad range of possible parameter values. However, such computations become very costly when continuously applied over a period of several decades, as is necessary in the case of HAMR debris.

Consequently, it is useful to investigate the equations that regulate the long-term behavior of orbits; such equations can be derived using the averaging method (McClain and Vallado [9], Battin [10], Curtis [11]). This method consists in averaging the keplerian elements over a fast angle (i.e., true anomaly) in order to eliminate fast dynamics and make the numerical integration faster.

Recent works (Krivov and Getino [12], Lucking et al. [13], Alessi et al. [14], Gkolias et al. [15]) demonstrated that the dynamics caused by the planetary oblateness coupled with the solar radiation pressure can be described through a model based on singly-averaged equations of motion. However, this hypothesis, as stated in Gkolias et al. [15] is valid

within a certain range of altitude, inclination, eccentricity and for extremely high value of AMR. The coupled perturbations affect the evolution of the eccentricity, inclination and orientation of the orbit with respect to the Sun–Earth line. Resonant interactions lead to non-trivial orbital evolution that can be exploited in mission design. However, the dynamics in the vicinity of each resonance can be analytically described by an extended resonant model that provides the location of the central and hyperbolic invariant manifolds which drive the phase space evolution.

1.1. Literature Review

In the following section, the examined literature is reported, organised by topic.

1.1.1. Solar radiation pressure-J_2 model

The effect of the solar radiation pressure (SRP) on Earth satellites was recognised since the first space flights of Vanguard I (Musen et al. [16]) and the Echo balloons (Shapiro and Jones [17]), which were found to be significantly influenced by SRP.
Musen [18], Boulton [19], were pioneers in identifying the role of the SRP effect coupled with the zonal harmonics J_2 of a primary body in the orbital evolution of a minor body. If the dynamics of the SRP perturbed orbit is treated as a perturbation problem, the singly averaged contribution of SRP is integrable and analytical solutions can be obtained (Mignard and Henon [20], Oyama et al. [21], Scheeres [22]).
Musen [16] and Cook [23] were the first to identify and locate six SRP resonances in the inclination and semimajor-axis plane (the singly averaged perturbing function decomposed in six distinct terms has also been reported in Kaula [24]), each of them dominating in a particular range of orbital elements. In particular, Cook [23] observed that, unlike lunisolar gravitational resonances, SRP resonances are able to produce variations in eccentricity even for circular orbits.
Nevertheless, when coupled with the effect of Earth's oblateness J_2 the system becomes a 2.5 degrees of freedom (DoF). An analytical insight can be recovered when treating locally the semi-secular SRP resonances.
The equation of motion have been derived as singly averaged disturbing Hamiltonian potential associated with the oblateness and the solar radiation pressure effect, as described by many authors (Mignard [25] for dust particles, Cook [23], Krivov and Getino [12], Colombo et al. [26] for communication spacecrafts, Alessi et al. [14], Colombo and McInnes [27] for smart dusts dynamics, and Colombo et al. [28] for Earth observation spacecrafts), considering some simplifying hypothesis, such as considering the cannonball

model for the SRP force acting on the object and neglecting the third-body perturbation. The disturbing potential associated with the SRP has also been reported in Casanova et al. [29] and in Scheeres [22].
The dynamics arising by combining each of the harmonics with the secular evolution due to J_2 can be reduced to a 1 DoF resonant model described by the only resonant angle (Krivov and Getino [12]; Lücking et al. [13]; Alessi et al. [14]).
Daquin et al. [30] provided the formalization for reducing the multi-resonant Hamiltonian formalism to the single-resonance. The first set of transformations developed in [30], were applied to the formulation of the Hamiltonian using Delaunay element in order to reduce the representation to a single-resonance model.
The derivation of the six different resonant models in the three-dimensional case and their effect on the long-term evolution of resident space objects has also been recently discussed in the literature by Alessi et al. [14].
In their paper, Gkolias et al. [15] and Alessi et al. [14] re-derive the resonant models in the Hamiltonian framework, providing also a non-singular representation of the resonant dynamics and bifurcation analysis of the dynamics exploiting the results obtained in the field of single-resonance modelled by Alessi et al. [14]. After the distillation of the Hamiltonian function to a 1-DoF, autonomous system, the authors have studied the bifurcation map in the plane of the semimajor-axis and inclination, providing the number and type of equilibrium point in each region of the space.
The solar radiation pressure, Earth oblateness model has also been used to design of frozen orbits for small-size objects in Alessi and Colombo [31] and Luo et al. [32].
These works assume that the spacecraft is always in sunlight; Lemaitre and Habaux [33] studied the impact of Earth shadow on the long-term evolution of space debris under the solar radiatio pressure, Earth oblateness framework. Recent numerical results were obtained in the context of the ReDSHIFT project in Rossi et al. [34].

1.1.2. Fundamental resonance Hamiltonian models and applications

As first approximations, the resonant interaction between the orbital perturbations plays a role in the dynamical evolution of the orbiting objects. This topic has been subjected to a thorough examination, as detailed below.
In the past, fundamental models were derived in order to have a simplified model capable of qualitatively describing the motion of orbiting objects. The fundamental models are derived from a reduction of Hamiltonian models to a description with the fewest param-

eters conceivable.
The first work on this topic is in Andoyer [35], on the motion of the Moons of Jupiter. Then Henrard and Lemaitre [36] proposed the second fundamental model, and Breiter [37], [38] the extended fundamental and the lunisolar resonance models (see also Celletti and Gales [39], they have studied the motion of debris in a resonance in the MEO region). Winter and Murray introduced in [40] and [41] the Andoyer Hamiltoinan model in the context of exterior resonance and asymmetric libration points, inspired by the works done in Andoyer [35] and Beauge et al. [42].
They have proven the existence of asymmetric equilibrium points in the $1 : n$ resonance in the context of planar, circular, restricted three body problem. Although this is a very interesting result, only the mathematical considerations about the asymmetric equilibrium point were used in this work. Together with Gkolias et al. [15], these authors have inspired this thesis, allowing to understand how to merge the contribute of the Sun gravitational perturbation into the state-of-art modelling, exploiting the same resonant terms of the Sun perturbations. In particular, the Sun perturbation and the SRP have, for certain resonances, the same resonant angle, which can be used to reduce the extended system to an autonomous system.
Gkolias et al. [43], described the double-averaged Hamiltonian in ecliptic variables of the Earth oblateness, lunisolar model providing also the bifurcation analysis.
Regarding the GNSS orbits, Scheeres et al. [44] applied the lunisolar Hamiltonian formulation to understand the long term evolution of spacecrafts in that region. Lara et al. [45], instead, studied the resonance $3 : 5$ affecting the motion of the Galileo operational orbits.
Regarding the Earth oblateness-lunisolar model, Celletti et al. provided in [46] the bifurcation analysis of the coupled J_2-Lunisolar multiply-averaged Hamiltonian whichs depend only on the inclination, and Scala et al. [47] for post-mission disposal of satellites in high-altitude orbits.

Space debris dynamics

The need to predict the spatial distribution of space debris has necessitated the development of a comprehensive dynamical model. The presence of HAMR debris in GEO, posed the starting condition for the research on analytical models able to describe the complex interaction between orbital perturbation and foreseen their accumulation in space.
The GEO region can be considered as a $1 : 1$ gravitational resonance, in which the debris are captured. In a pendulum-like model, a separatrix separates the inner and exterior circulation regions from the central libration region (Lemaitre [48]). If the dynamics of

HAMR debris is perturbed by the SRP, instability and chaos are introduced around the separatrix. Analyses with a numerical chaos indicator (MEGNO, Cincotta et al. [49]) were performed by Breiter et al. [50] and for large AMR, by Valk et al. [3]. The size of the chaotic region around the separatrix is increasing with the AMR, as expected, making the coupled dynamics complex to describe.

To this scope, Lemaitre [48] developed a "toy-model" based on the Hamiltonian formalism able to reproduce and explain the structure obtained by the previous authors. Following the works by Lemaitre, in Casanova et al. [51] they merged a synthetic population of debris with the solar radiation pressure, Earth gravitational, and lunisolar perturbation Hamiltonian model developed by the team of the University of Namur (Casanova et al. [29], Valk et al. [52]), to retrieve information regarding the placement of the debris in space. Also Celletti et al. [53] used proper elements of the solar radiation pressure, Earth gravitational, and lunisolar perturbation Hamiltonian (Celletti et al. [54], Celletti and Gales [55]), to reconstruct the evolutionary history of debris and possibly to associate the fragments to a parent body.

To investigate the long-term dynamical evolution of HAMR objects released, in each of the six orbital planes used by Global Positioning System (GPS) satellites, a large number of simulations, including all relevant perturbations, were performed by Anselmo and Pardini in [56], and by Wang et al. [57] in Geostationary Transfer Orbits, showing also the presence of resonance between solar radiation pressure and Sun gravity. In the context of the dynamics of space debris in Earth resonance, Gales and Celletti in [58] studied the dynamics in the $1:1$ and $2:1$ resonances, where geosynchronous and GPS satellites are located; and in [59] about resonances outside the geostationary ring, such as $1:2$, $1:3$, and $2:3$ (regions of XMM-Newton and Integral missions).

In the context of dynamical trapping of debris in resonances, Henrard [60] introduced the concept of adiabatic capture in resonance (see also Lemaitre et al. [48]) through a slowly decreasing parameter, such as the semimajor-axis due to weak non-conservative phenomena. From this work, the literature has been developed in the understanding on how asteroid and debris belts have been formed under the effect on non-conservative contributes, such as the Poynting-Robertson drag (the dissipative part of the solar radiation pressure, see Lhotka et al. [61] and Gomes [62]), or in the presence of migration (Mustill and Wyatt [63] and Batygin [64]) or due to equilibrium crossing in LEO caused by air drag dissipation (Celletti and Gales [65]).

This work, like Casanova et al. [51], explots a synthetic population of space debris. The synthetic population represents the actual population and preserves its characteristics. The concept strength resides in the ability to compute numerically the orbits of each piece of space debris constituting the synthetic population. This has been done imple-

menting the Standard NASA Breakup Model to generate a population of debris based on a gaussian distribution of Area-To-Mass ratio and Δv. The model implemented has been taken from Bade et al. [66], Johnson et al. [67], and Frey and Colombo [68].
A dynamical mapping campaign in distinct phase space planes (i.e. semimajor-axis versus inclination with eccentricity diameter as index) as done in Gkolias et al. [69], Alessi et al. [14], Alessi and Schettino [70] and Schaus et al. [71] was carried out using a semi-analytical propagator developed following the works done in Colombo [72], Colombo [73], Gkolias and Colombo [69] in order to detect unusual situations for debris entrapment. The statistical method was chosen over the analytical method due to the need to statistically demonstrate the accumulation of debris at stable points.

De-orbiting manoeuvre

The main contributes to the design of passive de-orbiting in the planar SRP-J_2 model have been given by Lucking, Colombo and McInnes in [74], [75], for Sun Synchronous orbits in [76], for communication spacecrafts in [26], by using deployable balloons in Colombo et al. [77], and by using pressure-augmented devices from high-altitude orbits in Colombo et al. [78]. Then, Gkolias et al. [15], Giovannini and Colombo in [79], have contributed to the design of solar sail deorbit manoeuvre, extending the planar Hamiltonian model to the inclined orbit Hamiltonian model. The first studies involved only a planar simplified version of the Hamiltonian, without including inclination of the orbit nor the tilt of the Earth axis. More recent studies, from Gkolias et al. and Giovannini and Colombo, otherwise included both these aspects. The fact of having a more comprehensive model implies more reliable results in terms of feasibility of the disposal technique adopted. The work in Gkolias et al. [15] regarding the deorbiting from an inclined orbit has been taken as a landmark for this thesis together with all the works of the previously cited articles. In particular, the formulation of the "two-point boundary value problem" connecting the initial condition of the de-orbiting spacecraft to its critical condition, was adopted and integrated together with the extended model developed in the thesis.
Moreover, it the framework of multiple-resonant model, natural highways generated by the coupled model have been exploited for de-orbiting by Alessi et al. [70], [80], and Schettino et al. [81]. Exploiting the interaction between the Earth oblateness and lunisolar perturbations, Scala et al. [47], [82] designed natural post-mission disposal trajectory of spacecrafts in high-altitude orbits.

1.2. Aims and contributes of the thesis

The research presented in the following thesis is aimed to formulate a new Hamiltonian model of the coupled SRP-Earth oblateness and Sun third-body perturbation and asses its potentiality in the field of mission analysis, de-orbiting trajectory design, debris dynamics as well as contribute the theoretical comprehension of the dynamics of the current model and of the new one. To summarise, this work has been developed to answer the following questions:

1. How is it possible to add the Sun gravitational perturbation to the current single-averaged single-resonance SRP-J_2 Hamiltonian model ?;
2. How can it be used to disposal manoeuvre of inactive spacecrafts ?;
3. How can it be used to comprehend the evolution of low AMR fragments after an explosion ?.

Contributes of the thesis

The most significant contribution of this thesis to the academic landscape of astrodynamics is the development of a single-averaged and single-resonance Hamiltonian model to include the gravitational perturbation of the Sun into the state-of-the-art coupled SRP-J_2 dynamical model. The contribution is not only theoretical but also practical, as it contributes to the understanding of debris dynamics and the preliminary design of a novel de-orbiting maneuver based on the insights acquired from the dynamical analysis of the expanded model.
In particular, in the field of space debris, conditions under which low and medium AMR may accumulate into equilibrium points in the space are formulated. Unfortunately, due to the lack of real data, the theory has only been validated with a synthetic debris population generated through the NASA Breakup Model. However, in order to make the validation as much realistic as possible, the debris population has been propagated with ad hoc semi-analytical propagator and specific conditions for debris trapping have been searched to validate the theoretical conditions.
Regarding the design of de-orbiting maneuver, two novel ways to exploit the solar radiation pressure to drive the spacecraft towards the Earth are proposed. In particular, instead of opening an area-augmented device, it has been found a way to de-orbit when the sail is closed, while it is opened during the mission life. However, while the theoretical contribute is disruptive, from the practical point of view, at the moment is rather unfeasible. This because, the manoeuvre exploits the peculiar dynamics of the extended

model, which can be only exploited if the spacecraft is initially placed on an equilibrium point near the critical eccentricity of its orbit.

1.3. Thesis outlines

The thesis work has been organised in six Chapters. A part from the first which includes the literature review and the contributes given to the scientific community, the other are:

- Chapter 2 summarises the fundamentals on the orbit propagation theories used in this work, together with usual validation with both TLEs and high-fidelity models;
- Chapter 3 describes the main results from the previous SRP-J_2 model;
- Chapter 4 develops and describes the contributes given in the extended model. together with its formulation and dynamical structure;
- Chapter 5 describes the application of the developed theory to the fields of de-orbiting manoeuvre and debris analysis;
- Chapter 6 outlines the conclusions and gives the route for future analyses.

2 | Perturbation theory

In the Section that follows, the approaches used to propagate orbits under the influence of conservative forces are described. Two propagators, one based on a high-fidelity force model and the other on a semi-analytical model, are coded and verified in comparison to known TLEs and the STELA propagator.

2.1. Semi-analytical propagator

The method used to analyse the long-term orbital evolution of debris orbits discussed here is mainly inspired by the work of Gkolias et al. [69]. A detailed description of the force model is given in Appendix A. Aiming for a several year integration time span, a single-averaged semi-analytical propagation was opted for, which is a typical practise for Earth satellite orbits (see Colombo et al. [72], [73]) because it can considerably reduce the computation time while maintaining good accuracy. For the main force model, the contributions of Earth's geopotential, third-body perturbation from the Sun and the Moon, and the effect of solar radiation pressure were considered:

- For the geopotential force the only oblateness of the Earth is considered, and the normalised coefficients $C_{n,m}, S_{n,m}$ are taken from Kaula [24].
- The third-body potential is expanded up to fourth order in the parallactic factor and is averaged in closed form over the mean anomaly of the satellite. This is more efficient computationally instead of using a series expansion representation. The positions of the perturbing bodies (i.e., the Sun and Moon) are computed from analytical time series; the ephemeris of the Moon are generated from the algorithm described in Simpson [83] and the ephemeris of the Sun are generated from the algorithms described in the Chapters 25 and 26 by Meeus [52]. (see Appendix A for details).
- The solar radiation pressure is also included under a cannonball approximation (Kaula [24], Krikov and Getino [12]).
- The eclipse has been neglected : during an eclipse, the spacecraft is in the Earth's

shadow and does not receive direct sunlight, which means that the force due to SRP is significantly reduced. However, the spacecraft may still experience a small force due to scattered light from the Earth's atmosphere or reflected sunlight from the Moon. As shown by Gkolias et al. [15], in the Hamiltonian function, which is a mathematical representation of the dynamics of a system, the effects of the SRP are typically modeled as a perturbation term. This means that the Hamiltonian function includes the effects of SRP, but only as a small correction to the dominant gravitational forces (see Figure 2.1). Because the force due to SRP during an eclipse is small compared to the force during periods of direct sunlight, it can be neglected without significantly affecting the accuracy of the Hamiltonian function. Therefore, for practical purposes, the eclipse can be ignored when modeling the effects of SRP on the dynamics of a spacecraft.

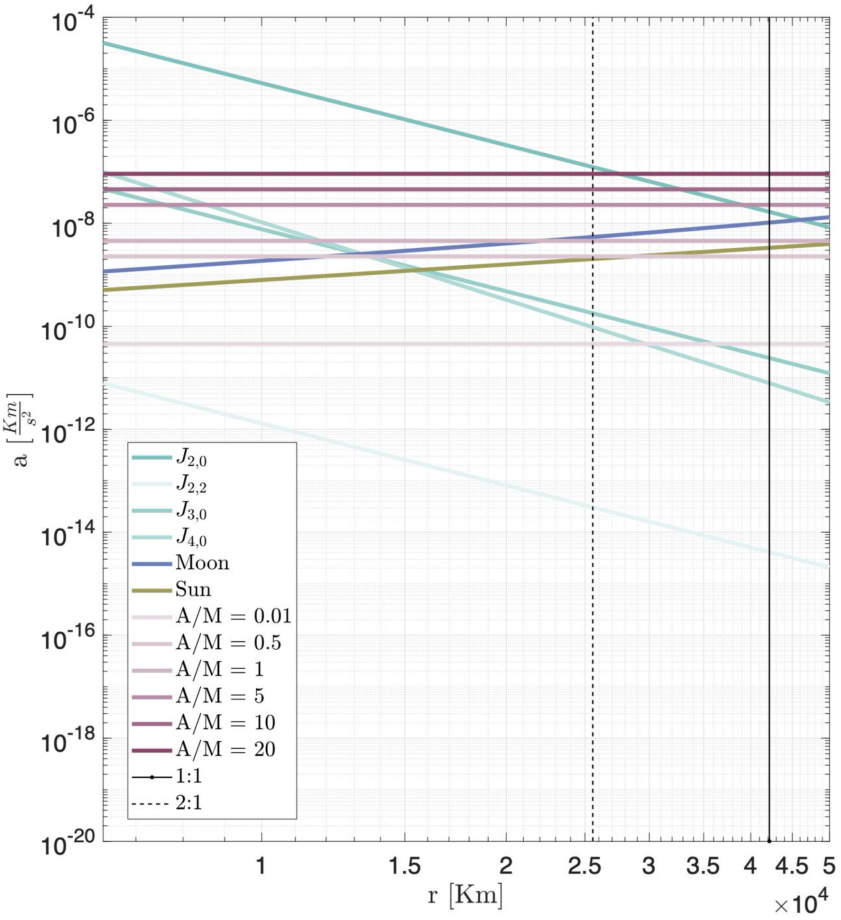

Figure 2.1: Comparison of order of magnitude of perturbation acceleration computed according to Montenbruck and Eberhard [84] with Equation (A.1). The SRP contribute is evaluated for different AMR.

The semi-analytical propagator used for all the simulations is based `ode45` which is based on an explicit Runge-Kutta (4,5) formula, the Dormand-Prince (see Dormand and Prince [85]) pair with `RelTol,AbsTol = 1e-7`.

2.2. High fidelity propagator

In addition, an high-fidelity full-dynamics propagator based on cartesian coordinates was developed for comparison with the semi-analytical propagators (for details on the formulation refer to Appendix A). The numerical integration is based on `ode78` which is an implementation of Verner's Runge-Kutta 8(7) pair with a 7^{th}-order continuous extension (Verner [86]) with `RelTol,AbsTol = 1e-8`. For the main force model, the contributions of Earth's geopotential, third-body perturbation from the Sun and the Moon, and the effect of solar radiation pressure were considered:

- For the geopotential force, the expansion of the geopotential disturbing function using the Legendre polynomial P_{nm} is used (Kaula [24]);
- The ephemeris of the Sun and the Moon, and the the transformation matrices related to the motion of Earth's rotation axis are retrieved from NASA's SPICE toolkit4 (see Acton [87]);
- The SRP force is intended aligned with the Sun-Earth line, and the object is considered under the cannonball hypothesis, that is to say that the solar rays are considered perpendicular to the surface of the satellite. The SRP force is the same as described in Lhotka et al. [61]

2.2.1. Semi-analytical propagator validation

The semi-analytical propagator model described in Appendix A was validated by comparison with the actual ephemerides of an artificial satellites in highly-elliptical orbit: XMM-Newton. The orbit of XMM-Newton was propagated in the time span from 1999/12/15 to 2013/01/01 with the initial Keplerian elements on 1999/12/15 at 15:00 UTC as reported in Table 2.1. The Figure 2.2 shows the comparison between the ephemeris taken from SpaceTrack [88]; in red the orbit propagated using the semi-analytical propagator, and in blu the ephemeris.
The semi-analytical propagator is also validated against the developed high-fidelity propagator and the semi-analytical propagator developed by CNES [89]. The Figure 2.3 shows the comparison between the propagators; in blu the orbit propagation computed by the STELA, in yellow by the high-fidelity, and in red by the semi-analytical propagators, re-

spectively. The initial conditions are integrated from 2000/01/01 to 2100/01/01 with the initial Keplerian elements on 2000/01/01 at 00:01 UTC as reported in Table 2.1. The developed propagator shows good agreement with the high-fidelity one, validating the force model selection and the use of a single-averaged formulation. However, the evolution of the semimajor axis as described by STELA is not constant due to the semi-analytical nature of the equations of motion. The right-hand sides of the averaged equations of motions must be truncated and then averaged over one period under certain simplifying hypotheses (typically, that the mean orbital elements are constant during the averaging operation).

This averaging error can be considered the contribution to the integration error caused by these simplifications (Rosengren et al. [90]). For similar reasons, the high-fidelity model shows a non-constant semimajor-axis. The numerical errors are responsible for few kilometers errors in the semimajor-axis propagation with respect to the initial condition. Instead, due to the extremely simplified equation of motion used in the semi-analytical propagator, it shows a constant altitude.

Regarding the computational time, the single-averaged formulation is orders of magnitudes faster (few seconds for the semi-analytical and up to 8h for the high-fidelity propagator), which allows us to proceed with a massive and accurate characterisation of the phase space.

Table 2.1: Initial Keplerian elements of Figure 2.2 and Figure 2.3

Test	a km	e	i rad	Ω rad	ω rad	f rad	AMR m^2/kg
Figure 2.2	67045	0.7951	0.67988	4.1192	0.99259	3.2299	0.012
Figure 2.3	42165	0.1	0.6981	0	0	0	2

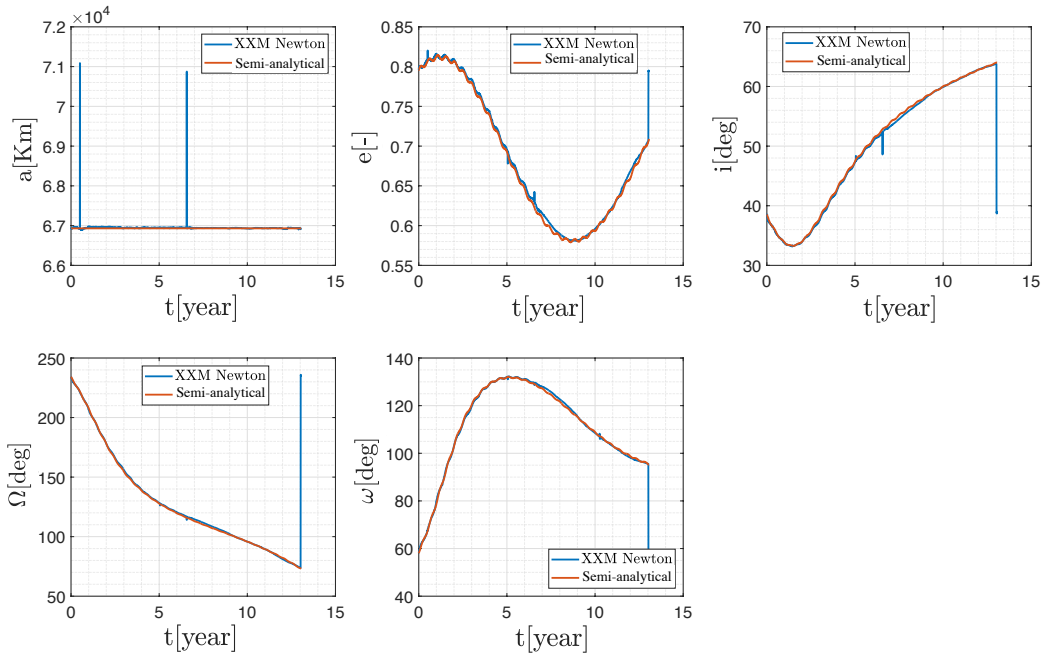

Figure 2.2: XMM Newton ephemerides: actual ephemerides and propagation with the semi-analytical propagator developed in this work.

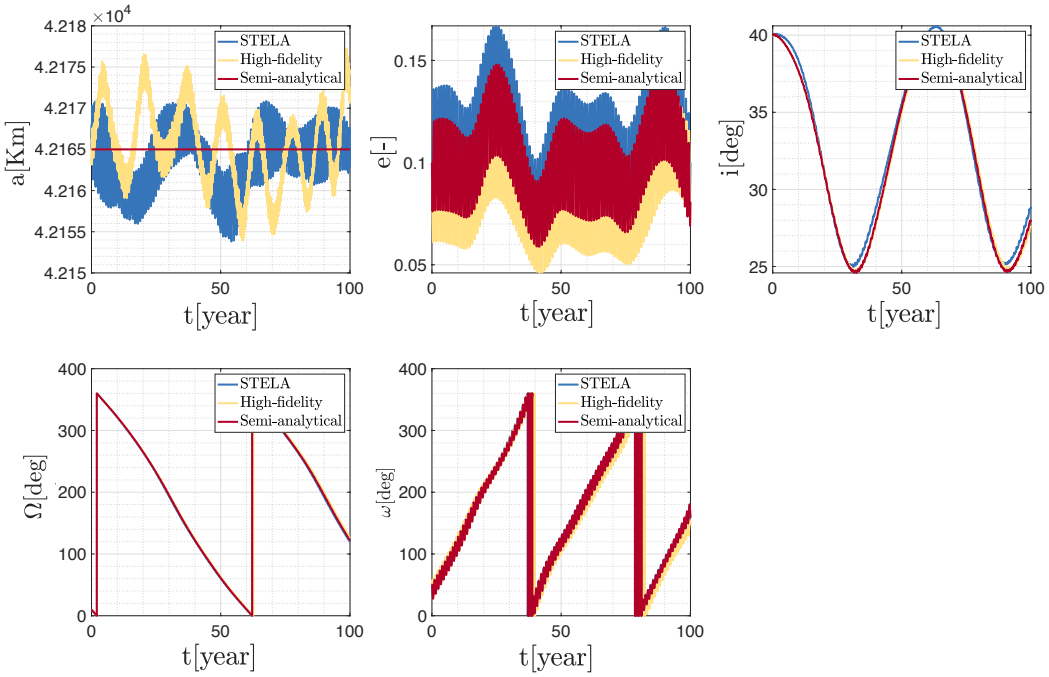

Figure 2.3: Comparison between the semi-analytical propagator, STELA and the high-fidelity propagator.

2.3. Hamiltonian approach

As stated by Celletti et al. [91], in the Hamiltonian framework, the natural approach is based on canonical perturbation theory. By using appropriate sets of canonical variables, the geopotential, the lunisolar attraction, and the SRP can be expressed in forms suitable for the series expansions needed in perturbation methods. Nonetheless, for each orbital region with its own hierarchy of perturbations, it is advantageous to select the principal contributions and perform a proper ordering of terms in order to comprehend the predominate dynamical behavior.
With this formalism, the system dynamics is completely described by a scalar function $\mathcal{H}$. Indeed, the Hamiltonian formulation is an energetic representation of the dynamical system. This function can be derived from the Lagrangian function $\mathcal{L}$ (Arnol'd, V.I. et al. [92], Lemaitre [48]):

$$\mathcal{L} = \mathcal{T} - \mathcal{V} \tag{2.1}$$

Supposing that the position of a mechanical system is described by the coordinate q, it can be said that $\mathcal{T}(q, \dot{q})$ is the kinetic energy while $\mathcal{V}(q)$ is the potential energy. If the conjugate momenta p is introduced such that (Arnol'd, V.I. et al. [92], Lemaitre [48]):

$$p_k = \frac{\partial \mathcal{L}(q, \dot{q})}{\partial \dot{q}_k}, \tag{2.2}$$

where k goes from 1 to the number of elements in the vector q. Now it is possible to define the Hamiltonian as (Arnol'd, V.I. et al. [92], Lemaitre [48]):

$$\mathcal{H} := p^T \dot{q} - \mathcal{L}(q, \dot{q}). \tag{2.3}$$

For Hamiltonian systems, the Hamiltonian function $\mathcal{H}(p, q)$ is a first integral, i.e. remains constant in time. Indeed it can be proven that the Hamiltonian is (Arnol'd, V.I. et al. [92], Lemaitre [48]):

$$\mathcal{H} = \mathcal{T} + \mathcal{V} \tag{2.4}$$

which is the total energy. Considering a general model of perturbation including the effect of Earth oblateness, Solar Radiation Pressure, and the gravitational influence of Sun and Moon, the Hamiltonian describing, the dynamics of the satellite in a geocentric equatorial inertial frame can be modelled by the Hamiltonian (Gkolias et al. [15], Celletti et al. [91], Lemaitre [48]):

$$\mathcal{H} = \mathcal{H}_{kep} + \mathcal{H}_{J_2} + \mathcal{H}_{SRP} + \mathcal{H}_{\odot} + \mathcal{H}_M + \mathcal{T}. \tag{2.5}$$

If the kinetic energy is constant (i.e., the force model is conservative), its contribute to the equation of motions is zero, therefore (Arnol'd, V.I. et al. [92], Lemaitre [48]):

$$\mathcal{H} = \mathcal{V}. \tag{2.6}$$

Knowing that, in a conservative framework the perturbing function $\mathcal{R} = -\mathcal{V}$, it is possible to say (Alessi et al. [14], (Arnol'd, V.I. et al. [92]), Lemaitre [48]):

$$\mathcal{R} = -\mathcal{H}. \tag{2.7}$$

From which it is possible to write the Langrange planetary equations (McClain, W.D. and Vallado, D.A. [9], Battin R.H. [10], Celletti et al. [91]):

$$\begin{aligned}
\frac{\mathrm{d}a}{\mathrm{d}t} &= -\frac{2}{na}\frac{\partial \mathcal{H}}{\partial M}, \\
\frac{\mathrm{d}e}{\mathrm{d}t} &= \frac{1}{na^2 e}\left(-(1-e^2)\frac{\partial \mathcal{H}}{\partial M} + \sqrt{1-e^2}\frac{\partial \mathcal{H}}{\partial \omega}\right), \\
\frac{\mathrm{d}i}{\mathrm{d}t} &= \frac{1}{na^2\sin(i)\sqrt{1-e^2}}\left(-\cos(i)\frac{\partial \mathcal{H}}{\partial \omega} + \frac{\partial \mathcal{H}}{\partial \Omega}\right), \\
\frac{\mathrm{d}\Omega}{\mathrm{d}t} &= -\frac{1}{na^2\sin(i)\sqrt{1-e^2}}\frac{\partial \mathcal{H}}{\partial i}, \\
\frac{\mathrm{d}\omega}{\mathrm{d}t} &= +\frac{1}{na^2\sin(i)\sqrt{1-e^2}}\cos(i)\frac{\partial \mathcal{H}}{\partial i} - \frac{\sqrt{1-e^2}}{na^2 e}\frac{\partial \mathcal{H}}{\partial e}, \\
\frac{\mathrm{d}M}{\mathrm{d}t} &= n + \frac{1-e^2}{na^2 e}\frac{\partial \mathcal{H}}{\partial e} + \frac{2}{na}\frac{\partial \mathcal{H}}{\partial a}.
\end{aligned} \tag{2.8}$$

Where, (a, e, i, ω, Ω) are the Keplerian orbital elements of the body measured with respect to the Earth equatorial plane, and n is the mean motion of the orbiting body.

3 | Fundamentals of the coupled solar radiation pressure and Earth oblateness dynamic

The following Chapter outlines the main results obtained from the literature review regarding the coupled SRP, Earth oblateness Hamiltonian model. Typically, the analysis of such a model is subdivided as follows :

- Definition of modelling hypothesis and the derivation of the dynamical model;
- Definition of the Hamiltonian model and its transformation to a single DoF autonomous function to which, the tools of system theory reported below, are applied;
- *Stability analysis*: for each equilibrium points, the stability properties are computed;
- *Bifurcation analysis*: for each resonance, the change in the dynamical the structure (i.e. the position of the equilibrium points) as a function of physical parameters (i.e. AMR) and obsculating parameters (i.e. a, e, i) is traced;
- *Phase space analysis*: the phase space in the plane (ψ, e) is analysed for each of the dynamical region identified.

3.1. Dynamical model

Henceforth, it is assumed that a small body (e.g., a spacecraft) moves under the following hypothesis:

- as perturbations only SRP and J_2 are taken into account: the third body effect up to MEO regions and for high values of AMR can be considered negligible (see Equation (A.1), Montenbruck and Gill [84], this hypothesis is dropped in the next Chapter);
- the Sun rays are considered perpendicular to the surface of the satellite (cannonball

model);

- albedo is not considered;
- the solar flux is considered constant;
- the satellite is considered in sunlight;
- the light aberration is neglected, hence the SRP can be considered as a conservative force.

Therefore, the dynamics of the satellite comes from the sum between the Keplerian dynamics, the SRP perturbation and the J_2 perturbation.
In the following equations, (a, e, i, ω, Ω) are the Keplerian orbital elements of the small body measured with respect to the Earth equatorial plane, $\lambda = \omega + f$ the argument of latitude, n the mean motion of the small body, μ the Earth gravitational parameter, J_2 the second zonal term of the geopotential, $R_\oplus$ the equatorial radius of the Earth, ε the obliquity of the ecliptic, $P_\odot$ the solar radiation pressure at 1 AU, c_R the reflectivity coefficient the area-to-mass ratio of the small body.

3.2. Hamiltonian formalism

Following the derivation by Gkolias et al.[15], the dynamics of the satellite in a geocentric equatorial inertial frame can be modelled by the Hamiltonian:

$$\mathcal{H} = \mathcal{H}_{kep} + \mathcal{H}_{J_2} + \mathcal{H}_{SRP} \tag{3.1}$$

The Keplerian part $\mathcal{H}_{\text{kep}}$ reads:

$$\mathcal{H}_{\text{kep}} = \frac{v^2}{2} - \frac{\mu}{r} \tag{3.2}$$

where μ is the gravitational parameter of the Earth, and r, v are the geocentric distance and velocity of the satellite, respectively.

The Earth's oblateness effect is modelled as (Gkolias et al. [15], Gkolias I. and Colombo C. [69]):

$$\mathcal{H}_{J_2} = \frac{\mathcal{C}_{J_2}\left(3\sin^2\phi - 1\right)}{2r^3} \tag{3.3}$$

where $\mathcal{C}_{J_2} = \mu R_\oplus^2 J_2$ with J_2 the oblateness parameter and ϕ the geographic latitude of the satellite. The sine of the latitude is expressed in terms of the orbital elements of the

satellite via (Gkolias et al. [15]):

$$\sin\phi = \frac{z}{r} \tag{3.4}$$

and

$$z = [0,0,1]R_3(-\Omega)R_1(-i)R_3(-\lambda)[r,0,0]^{\mathrm{T}} \tag{3.5}$$

Considering a generic angle u, the rotation matrices around the first (1) and third (3) axis, $(R_1(u), R_3(u))$ are defined as (Gkolias et al. [15]):

$$R_1(u) = \begin{pmatrix} 1 & 0 & 0 \\ 0 & \cos u & \sin u \\ 0 & -\sin u & \cos u \end{pmatrix}, \quad R_3(u) = \begin{pmatrix} \cos u & \sin u & 0 \\ -\sin u & \cos u & 0 \\ 0 & 0 & 1 \end{pmatrix} \tag{3.6}$$

The solar radiation pressure contribution is given by (Gkolias et al. [15]):

$$\mathcal{H}_{\mathrm{SRP}} = \mathcal{C}_{\mathrm{SRP}} X \tag{3.7}$$

where $\mathcal{C}_{\mathrm{SRP}} = \frac{3}{2} P_{\odot} c_R \frac{A}{m}$, X is the coordinate of the satellite in an Earth-centred system with the X-axis pointed towards the Sun. In terms of the orbital elements of the satellite it reads:

$$X = [1,0,0]R_3(\lambda_{\odot})R_1(\varepsilon)R_3(-\Omega)R_1(-i)R_3(-\theta)[r,0,0]^{\mathrm{T}} \tag{3.8}$$

with $\lambda_{\odot}$ the ecliptic longitude of the Sun. In Equation (3.7) and Equation (3.3) the true anomaly is the fast angle, hence the two equations are integrated over it for one period. The integrals can be carried out in closed form for both the J_2 and SRP contributions. In the case of J_2 the differential relationship $\mathrm{d}M = \frac{r^2}{a\sqrt{1-e^2}}\mathrm{d}f$ along with $r = a\frac{1-e^2}{1+e\cos f}$ are used to obtain (Gkolias et al. [15]):

$$\bar{\mathcal{H}}_{J_2} = \frac{\mathcal{C}_{J_2}(1-3c_i^2)}{4a^3(1-e^2)^{3/2}} \tag{3.9}$$

where $c_i = \cos i$. For SRP the integral with respect to the eccentric anomaly E is expressed

using the relations (Gkolias et al. [15]):

$$\begin{aligned} r\sin f &= a\sqrt{1-e^2}\sin E, \\ r\cos f &= a(\cos E - e), \\ r &= a(1-e\cos E), \\ \mathrm{d}M &= \frac{r}{a}\mathrm{d}E, \end{aligned} \tag{3.10}$$

resulting in (Gkolias et al. [15]):

$$\bar{\mathcal{H}}_{\mathrm{SRP}} = -ae\mathcal{C}_{\mathrm{SRP}}\sum_{j=1}^{6}\mathcal{T}_j\cos\psi_j \tag{3.11}$$

where the resonant argument is (Gkolias et al. [15], Alessi et al.[14]):

$$\psi_j = n_1\omega + n_2\Omega + n_3\lambda_\odot, \qquad \psi_j \in [0, 2\pi], \tag{3.12}$$

and $\mathcal{T}_j$ is the expansion term obtained from the expansion of the single-averaged model of the SRP (see Table 3.1 for each resonant term).

Table 3.1: Argument $\psi_j = n_1\omega + n_2\Omega + n_3\lambda_\odot$ of the periodic component in terms of n_1, n_2, n_3, and the coefficients $\mathcal{T}_j$ as in Gkolias et al. [15] and Alessi et al.[14].

j	n_1	n_2	n_3	$\mathcal{T}_j$
1	1	1	-1	$\frac{1}{4}(1+c_\varepsilon)(1+c_i)$
2	-1	1	-1	-$\frac{1}{4}(1+c_\varepsilon)(c_i-1)$
3	1	0	-1	$\frac{1}{1}s_i s_\varepsilon$
4	1	0	1	-$\frac{1}{1}s_i s_\varepsilon$
5	1	1	1	-$\frac{1}{4}(c_\varepsilon-1)(1+c_i)$
6	-1	1	1	-$\frac{1}{4}(c_\varepsilon-1)(c_i-1)$

The Equation (3.11) result is a well-known finding in the literature Krivov et al. [12], Lucking et al. [13], and Alessi et al. [14]. The approach proposed in Daquin et al. [30] for lunisolar gravitational perturbations, is adapted to the solar radiation pressure effect, under the assumption that only one periodic term j is driving the motion of the body at any given moment. This approach considers the first canonical transformations developed in [30] written in terms of classical Delaunay variables (L, G, H, l, g, h), and introducing

the set of resonant variables (Ψ, ψ) such that [30]:

$$\begin{aligned} \Psi &= \frac{G}{n_1}, & \psi &= n_1 g + n_2 h + n_3 \lambda_\odot, \\ \Pi &= -n_2 G + n_1 H, & \pi &= \frac{h}{n_1}, \\ K &= I_s - \frac{n_3 G}{n_1}. & \kappa &= \lambda_\odot. \end{aligned} \tag{3.13}$$

the Hamiltonian can be written in a 1-DoF autonomous form (Gkolias et al. [15]):

$$H_{\psi_j} = H_{\psi_j,J_2}(\Psi; L, \Pi) + H_{\psi_j,SRP}(\Psi, \psi; L, \Pi) + n_s(n_3\Psi + K), \tag{3.14}$$

where the part associated with J_2 is:

$$\mathcal{H}_{\psi_j,J_2}(\Psi; L, \Pi) = \frac{C_{J_2}\mu^3\left(n_1^4\Psi^2 - 3(\Pi + n_1 n_2 \Psi)^2\right)}{n_1^7 4L^3\Psi^5}, \tag{3.15}$$

and the one due to SRP is:

$$\mathcal{H}_{\psi_j,SRP}(\Psi, \psi; L, \Pi) = -\frac{C_{\mathrm{SRP}}}{\mu} L^2 \sqrt{1 - \frac{n_1^2\Psi^2}{L^2}}\mathcal{T}_j \cos\psi, \tag{3.16}$$

with the coefficients $\mathcal{T}_j$ are expressed in terms of the new variables using the equations $c_i = \frac{n_1 n_2 \Psi + \Pi}{n_2^2 \Psi}$ and $s_i = \sqrt{1 - c_i^2}$.

As a result of the resonant transformation, both π and κ are negligible; hence, Π and K are constants, and the term $n_\odot K$ can be eliminated from the Hamiltonian. The action variable Π is a resonant integral of the system; its value is determined by the initial conditions and stays constant during the orbital evolution (for the whole derivation, see Appendix C). Expressed in Keplerian orbital elements (Gkolias et al. [15]), Alessi et al. [14], Daquin et al. [30]):

$$\Pi = \sqrt{\mu a}\sqrt{1 - e^2}(-n_2 + n_1 \cos i) \tag{3.17}$$

represents the mathematical link between the oscillation of eccentricity and inclination of the orbit. Its value, which is associated to the inclination of an initially circular orbit (Π_0 or $\tilde{\Pi}_0 = \Pi_0/\sqrt{1000}\mu$) is used in this work to label the phase space.

For a satellite close to a resonance with argument ψ_j with initial elements:

$$(a_0, e_0, i_0, \omega_0, \Omega_0, \lambda_{\odot,0}), \tag{3.18}$$

the orbit evolution in the (Ψ ,ψ) plane, or equivalently in the (e,ψ) plane (substituting $\Psi = \sqrt{\mu a(1-e^2)}/n_1$), is given from the contour line of the implicit equation:

$$H_{\psi_j}(\Psi, \psi; L, \Pi) = H_{\psi_j}(\Psi(a_0, e_0), \psi(\omega_0, \Omega_0, \lambda_{\odot,0}); L, \Pi), \tag{3.19}$$

with $L = L(a_0)$ and $\Pi = \Pi(a_0, e_0, i_0)$. Note that Π depends on the resonance j through n_1 and n_2.

The equations of the motion related to the resonant models H_{ψ_j} are

$$\begin{aligned} \frac{\mathrm{d}\psi}{\mathrm{d}t} &= \frac{\partial H_{\psi_j}}{\partial \Psi}, \\ \frac{\mathrm{d}\Psi}{\mathrm{d}t} &= -\frac{\partial H_{\psi_j}}{\partial \psi}, \end{aligned} \tag{3.20}$$

where the first equation is called *commensurability equation*, because it describes the commensurability between the angles describing the motion of the object, while the second one is the equation of motion of the conjugated momentum linked to the eccentricity. The associated equilibria are given imposing null time derivative to both the equations:

$$\begin{aligned} \frac{\mathrm{d}\psi}{\mathrm{d}t} &= 0, \\ \frac{\mathrm{d}\Psi}{\mathrm{d}t} &= 0. \end{aligned} \tag{3.21}$$

The stationary solutions of the resonant model represent periodic orbits of the full equations of motion. Their stability is determined from the eigenvalues of the Hessian of the Hamiltonian $\mathcal{H}_{\psi_j}$ computed at each equilibrium point.

3.2.1. Dynamical equation of motion

In this Section the equations of motions written in terms of the Hamiltonian perturbing function are derived. The 1-DoF autonomous Hamiltonian Equation (3.16) can be exploited to describe the perturbing function $\mathcal{R}$ of the orbital dynamics driven by a single resonant term:

$$\mathcal{R} = -\mathcal{H}. \tag{3.22}$$

Hence, as described by Alessi et al. [14], the Lagrange equation of motion of the coupled SRP-J_2 dynamics expressed in mean Keplerian element is (Alessi et al. [14]):

$$\begin{aligned}
\frac{\mathrm{d}a}{\mathrm{d}t} &= 0, \\
\frac{\mathrm{d}e}{\mathrm{d}t} &= -C_{\mathrm{SRP}} \frac{\sqrt{1-e^2}}{na} \sum_{j=1}^{6} \mathcal{T}_j \frac{\partial \cos\psi_j}{\partial \omega}, \\
\frac{\mathrm{d}i}{\mathrm{d}t} &= -C_{\mathrm{SRP}} \frac{e}{na\sqrt{1-e^2}\sin i} \sum_{j=1}^{6} \mathcal{T}_j \left(\frac{\partial \cos\psi_j}{\partial \Omega} - \cos i \frac{\partial \cos\psi_j}{\partial \omega} \right), \\
\frac{\mathrm{d}\Omega}{\mathrm{d}t} &= \dot{\Omega}_{J_2} + \dot{\Omega}_{\mathrm{SRP}}, \\
\frac{\mathrm{d}\omega}{\mathrm{d}t} &= \dot{\omega}_{J_2} + \dot{\omega}_{\mathrm{SRP}},
\end{aligned} \tag{3.23}$$

3.2.2. Equilibrium

If it is assumed that the dynamics are driven by a single term j at a time, that means that only one periodic component (i.e. $\sin\psi_j$ for eccentricity and inclination; and $\cos\psi_j$ for Ω, ω) affects the motion, then the description of the dynamics can be simplified as (Alessi et al. [14]):

$$\begin{aligned}
\left.\frac{\mathrm{d}e}{\mathrm{d}t}\right|_j &= n_1 C_{\mathrm{SRP}} \frac{\sqrt{1-e^2}}{na} \mathcal{T}_j \sin\psi_j, \\
\frac{\mathrm{d}\psi_j}{\mathrm{d}t} &= n_1 \dot{\omega}_{(J_2,j)} + n_2 \dot{\Omega}_{(J_2,j)} + n_3 n_\odot,
\end{aligned} \tag{3.24}$$

The terms written in the equation are:

$$\begin{aligned}
\dot{\Omega}_{J_2} &= -\frac{3}{2} \frac{J_2 r_\oplus^2 n}{a^2(1-e^2)^2} \cos i, \\
\dot{\Omega}_{\mathrm{SRP}} &= C_{\mathrm{SRP}} \frac{e}{na\sqrt{1-e^2}\sin i} \sum_{j=1}^{6} \frac{\partial \mathcal{T}_j}{\partial i} \cos\psi_j, \\
\dot{\omega}_{J_2} &= \frac{3}{4} \frac{J_2 r_\oplus^2 n}{a^2(1-e^2)^2} \left(5\cos^2 i - 1\right), \\
\dot{\omega}_{\mathrm{SRP}} &= C_{\mathrm{SRP}} \frac{\sqrt{1-e^2}}{nae} \sum_{j=1}^{6} \mathcal{T}_j \cos\psi_j - \dot{\Omega}_{\mathrm{SRP}} \cos i.
\end{aligned} \tag{3.25}$$

For the resonances $j = 1, 2, 5, 6$, the commensurability equation $\dot{\psi}_j = 0$ can be reduced to (see Alessi et al.[14]):

$$c_1 \cos i^2 + c_2 \cos i + c_3 = 0. \tag{3.26}$$

with the coefficients c_i are reported in Table 3.2:

Table 3.2: Coefficients of the quadratic equation $c_1 \cos^2 i + c_2 \cos i + c_3 = 0$ associated with the equilibrium point at ψ_j for $j = 1, 2, 5, 6$. In the table, $\beta = \sqrt{1-e^2}$, $\gamma = \cos^2\left(\frac{\epsilon}{2}\right)$, $\rho = \sin^2\left(\frac{\epsilon}{2}\right)$ and $c_\psi = \cos\psi$. Note that Equation (3.26) is multiplied by $4a^5\beta^5 en$ to have the same notation as in Alessi et al. [14].

j	c_1	c_2	c_3
1	$15C_\oplus e\beta$	$-6C_\oplus e\beta + 2C_{\rm SRP}a^4\beta^4\gamma c_\psi$	$2C_{\rm SRP}a^4\beta^4\gamma(1-2e^2)c_\psi -$ $+e\beta\left(3C_\oplus + 4a^5\beta^4 nn_\odot\right)$
2	$-15C_\oplus e\beta$	$-6C_\oplus e\beta + 2C_{\rm SRP}a^4\beta^4\gamma c_\psi$	$-2C_{\rm SRP}a^4\beta^4\gamma(1-2e^2)c_\psi +$ $+e\beta\left(3C_\oplus - 4a^5\beta^4 nn_\odot\right)$
5	$15C_\oplus e\beta$	$-6C_\oplus e\beta + 2C_{\rm SRP}a^4\beta^4\rho c_\psi$	$2C_{\rm SRP}a^4\beta^4\rho(1-2e^2)c_\psi -$ $+e\beta\left(3C_\oplus - 4a^5\beta^4 nn_\odot\right)$
6	$-15C_\oplus e\beta$	$-6C_\oplus e\beta + 2C_{\rm SRP}a^4\beta^4\rho c_\psi$	$-2C_{\rm SRP}a^4\beta^4\rho(1-2e^2)c_\psi +$ $+e\beta\left(3C_\oplus + 4a^5\beta^4 nn_\odot\right)$

Instead, for the resonant terms $j = 3, 4$, the commensurability $\dot{\psi}_j = 0$ can be reduced to (Alessi et al. [14]) :

$$\sin i^3 + s_1 \sin i^2 + s_2 \sin i + s_3 = 0, \tag{3.27}$$

with the coefficients c_i are reported in Table D.2:

Table 3.3: Coefficients of the quadratic equation $\sin i^3 + s_1 \sin i^2 + s_2 \sin i + s_3 = 0$ associated with the equilibrium point at ψ_j for $j = 3, 4$. In the table, $\beta = \sqrt{1-e^2}$, $\gamma = \cos^2\left(\frac{\epsilon}{2}\right)$, $\rho = \sin^2\left(\frac{\epsilon}{2}\right)$ and $c_\psi = \cos\psi$. Note that Equation (3.26) is multiplied by $4a^5\beta^4 n/15\mathcal{C}_\oplus$ to have the same notation as in Alessi et al. [14].

j	s_1	s_2	s_3
3	$-\frac{2C_{\rm SRP}}{15C_\oplus e}a^4\beta^3\sin\epsilon c_\psi$	$-\frac{4}{15C_\oplus}\left(3C_\oplus - a^5\beta^4 nn_s\right)$	$\frac{2C_{\rm SRP}}{15C_\oplus}ea^4\beta^3\sin\epsilon c_\psi$
4	$\frac{2C_{\rm SRP}}{15C_\oplus e}a^4\beta^3\sin\epsilon c_\psi$	$-\frac{4}{15C_\oplus}\left(3C_\oplus + a^5\beta^4 nn_s\right)$	$-\frac{2C_{\rm SRP}}{15C_\oplus}ea^4\beta^3\sin\epsilon c_\psi$

If the orbiting object is in an equilibrium point, such as $(\dot{e}, \dot{\psi}) = 0$, its orbit is characterised

by a constant eccentricity, inclination, semi-major axis and, depending on the resonant term j (Alessi et al. [14]):

- if $j = 1$ and it is on a prograde orbits, the longitude of the periapsis is sun-synchronous: $\dot{\Omega} + \dot{\omega} = n_{\odot}$;
- if $j = 2$ and it is on a retrograde orbits, the longitude of the periapsis is sun-synchronous: $\dot{\Omega} - \dot{\omega} = n_{\odot}$;
- if $j = 3$, the argument of periapsis is sun-synchronous: $\dot{\omega} = n_{\odot}$;
- if $j = 4$, the argument of periapsis is sun-antisynchronous: $\dot{\omega} = -n_{\odot}$;
- if $j = 5$ and it on a prograde orbits, then the longitude of the periapsis is sun-antisynchronous: $\dot{\Omega} + \dot{\omega} = -n_{\odot}$;
- if $j = 6$ and it is on a retrograde orbits, then the longitude of the periapsis is sun-antisynchronous: $\dot{\Omega} - \dot{\omega} = -n_{\odot}$.

3.3. Stability analysis

The stability of an equilibrium point can be evaluated following the procedure outlined by Alessi et al. [14], by computing the eigenvalues of the Hessian matrix evaluated at the equilibrium point:

$$\text{Hess}(\mathcal{H}_j) = \left(\begin{array}{cc} \frac{\partial \dot{e}}{\partial e} & \frac{\partial \dot{e}}{\partial \psi} \\ \frac{\partial \dot{\psi}}{\partial e} & \frac{\partial \dot{\psi}}{\partial \psi} \end{array} \right) \Bigg|_{e_{eq}, \psi_{eq}} \tag{3.28}$$

with partial derivatives $\frac{\partial \dot{e}}{\partial e}$ and $\frac{\partial \dot{\psi}}{\partial \psi}$ are zero if evaluated at the equilibrium. Therefore, the information about the stability of the point can be easily retrieved evaluating the eigenvalues of the Hessian:

$$\lambda^2 - \frac{\partial \dot{e}}{\partial \psi} \frac{\partial \dot{\psi}}{\partial e} = 0 \quad \rightarrow \quad \lambda_{1,2} = \pm \sqrt{\frac{\partial \dot{e}}{\partial \psi} \frac{\partial \dot{\psi}}{\partial e}} \tag{3.29}$$

if the sign of the term under the square root is positive, the eigenvalues are positive, hence it is unstable. On the other hand, if it is negative, the eigenvalues are complex conjugated, thus the orbit is periodic, therefor it is stable. The partial derivatives are the sum of the Earth oblateness and SRP and reported below:

$$\begin{aligned}
&\frac{\partial \dot{e}_{|j}}{\partial e} = 0,\\
&\frac{\partial \dot{e}_{|j}}{\partial \psi_j} = n_1 C_{\mathrm{SRP}} \frac{\sqrt{1-e^2}}{na} \mathcal{T}_j \cos\psi_j,\\
&\frac{\partial \dot{\psi}_j}{\partial e} = n_2 \frac{\partial \dot{\Omega}_{(J_2,j)}}{\partial e} + n_1 \frac{\partial \dot{\omega}_{(J_2,j)}}{\partial e},\\
&\frac{\partial \dot{\psi}_j}{\partial \psi_j} = 0.
\end{aligned} \tag{3.30}$$

where, the terms of the Hessian matrix of the commensurability equation are are reported in Appendix B in Equation (B.1).

3.4. Bifurcation analysis

By definition (see Guardia et al. [93], and Arnol'd [94]), the bifurcation analysis is the study of changes in the qualitative or topological structure of a given family of curves, such as the integral curves of a family of vector fields and the solutions of a family of differential equations. A bifurcation takes place when a small and continuous change in the parameter values (the bifurcation parameters) of a system results in an abrupt qualitative or topological change in its dynamical behavior. There are two primary types of bifurcations: *local*, which can be completely analysed through changes in the local stability properties of equilibria, periodic orbits, and other invariant sets when parameters exceed critical thresholds, and *global*, which frequently occur when larger invariant sets (i.e. periodic orbits) of the system *collide* with each other, or with equilibria of the system. Given an Hamiltonian function, as that defined in Equation (3.14), it is possible to choose one or more *bifurcation parameters* (see Sadovskii and Delos [95]), the change of which, cause the qualitative change of the topological structure of the phase space describing the Hamiltonian function. For the analysis performed in this work, the Hamiltonian structure can change varying mainly three parameters, the semi-major axis a, the inclination of the initially circular orbit i_0 (or similarly the second integral of motion Π_0) and the physical parameter AMR. Henceforth, i_0 (or Π_0) is considered the first bifurcation parameter and a the second, keeping the AMR fixed.

Solving Equation (3.26) in correspondence of $\psi = 0$ and $\psi = \pi$ at a fixed AMR and semi-major axis, the resulting *bifurcation diagram* represents the position of the dynamical equilibrium in the plane (e, Π_0).[1] A *bifurcation map* in the plane of the bifurcation parameters (a, i_0) is made computing the position of the bifurcations in that plane. For

[1] Generally indicated as $\tilde{\Pi}_0 = \Pi_0 \sqrt{1000\mu}\ \sqrt{km}$, or equivalently the corresponding i_0 at a fixed a.

each critical point in the bifurcation diagram, its stability is evaluated computing the eigenvalues of the Hessian matrix defined in Equation (3.28) evaluated at the critical point. A local bifurcation occurs when the Hessian has null eigenvalues. The bifurcations can be of different types:

1. *saddle-point* in which two fixed points (or equilibria) of a dynamical system collide and annihilate each other. If the phase space is one-dimensional, one of the equilibrium points is unstable (the saddle), while the other is stable (the node). As already stated by Breiter in [37], the number of equilibria can increase only through the saddle-node bifurcations;

2. *saddle-point connection* occurs when the values of the Hamiltonian at both unstable points are equal. This kind of bifurcation was firs depicted by Arnold et al. [94] and applied to the Extended Fundamental model by Breiter [37]. Also Gkolias et al. [15] have pointed out the presence of this kind of bifurcation in the framework of the couple SRP-J_2 Hamiltonian;

3. *trans-critical* in which a fixed point exists for all values of a parameter and is never destroyed. However, such a fixed point interchanges its stability with another fixed point. This point has already been discovered in the work by Gkolias et al. [15];

4. *pitchfork* where the system goes from one fixed point to three fixed points. This bifurcation is not present in the system under study;

5. *imperfect pitchfork* bifurcation occurs when a symmetry-breaking term is added to the pitchfork. Differently from the pitchfork one, this is possible to find in the system under study.

The bifurcation characteristic is evaluated only numerically, since an analytical investigation is cumbersome. In the following section, it is outlined the bifurcation analysis of the first resonance only (see Gkolias et al. [15] for all the others).

3.4.1. Bifurcation analysis of resonance $j = 1$

In the following section it is outlined the detailed bifurcation analysis of the first resonance of the mean anomaly averaged SRP-J_2 Hamiltonian model. Although this analysis has been already done by Gkolias et al. [15] and Alessi et al. [14], it is presented as basis for more advanced analysis and for deepen our knowledge on this topic. Moreover, there are reported some new insights on the dynamics of sub-critical, imperfect pitchfork and saddle-point connection bifurcations.

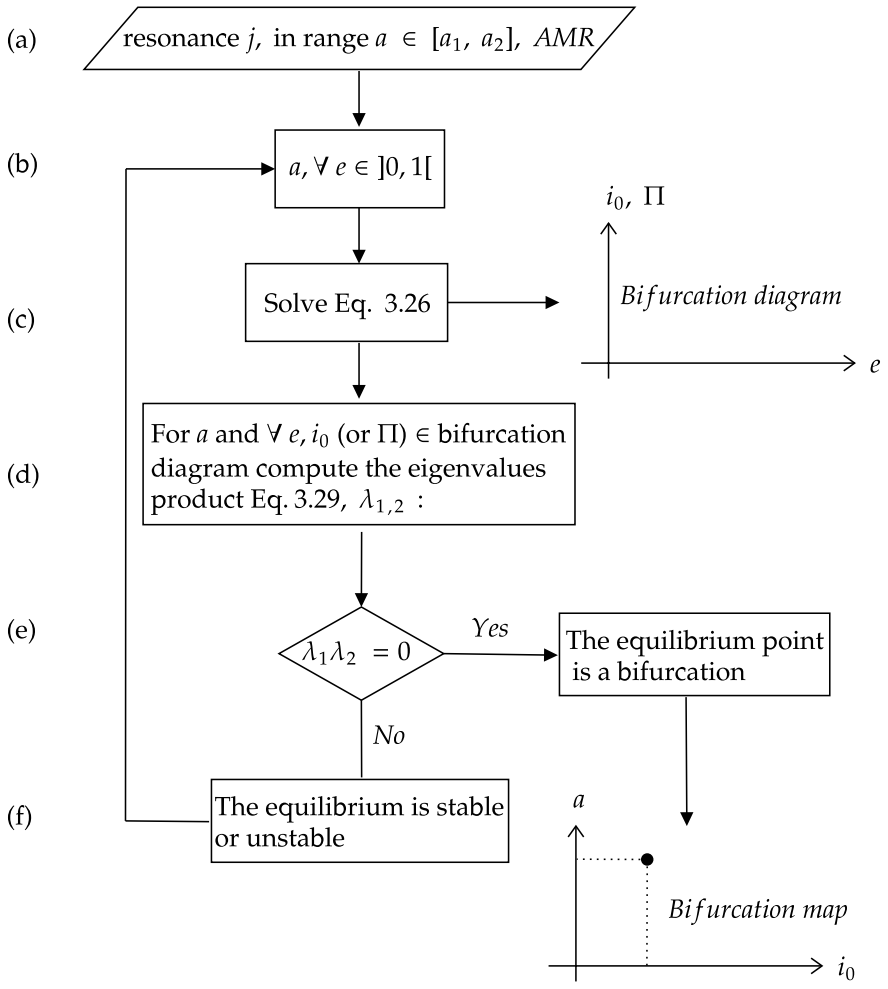

Figure 3.1: Flow diagram for the generation of a bifurcation map for a given resonance, in range $[a_1, a_2]$ and a given AMR.

The bifurcation analysis follows two major steps:

- the generation of bifurcation diagrams for each semi-major axis considered in the analysis;
- the assembly of the bifurcation map on the basis of the stability analysis carried on the bifurcation diagrams just derived.

Following the flow diagram in Figure 3.1, the bifurcation diagram at a specific semi-major axis and AMR is computed solving for each eccentricity in the range $e \in]0, 1[$ the Equation (3.26). Once the position of the equilibrium is identified for each semimajor-axis (in range 8000 km, 30000 km) and prescribed AMR, their stability is evaluated by looking at the sign of the eigenvalues of the equilibrium points (Equation (3.29)). A bifurcation

occurs when the product between the eigenvalues is zero ($\lambda_1\lambda_2 = 0$), or equivalently when the product changes sign. The bifurcation point coordinates $(\tilde{\Pi}_0, e)$ are then reported in the plane (a, i_0) to build up the complete bifurcation map, where i_0 is the inclination of the corresponding circular orbit:

$$\cos i_0 = \frac{\tilde{\Pi}_0\sqrt{1000\mu}}{n_1\sqrt{\mu a(1-e^2)}} + \frac{n_2}{n_1} \tag{3.31}$$

To distinguish between the saddle and the trans-critical bifurcation, two different bifurcation point search methods have been applied:

- saddle-point search method: for each bifurcation diagram, the saddle-point of the curve are found by computing the position of the zero derivative of the curve. This method is pretty fast and accurate, however it can detect only points were the number of equilibria change;
- stability-change-point search method: this method exploits the concept of stability depicted before.

Case study results

In Figure 3.2 the bifurcation diagram at $a = 12078$ km and AMR $= 1\ m^2$/kg is reported. It is possible to note that the Equation (3.26) admits at maximum two solutions (indicated with apex (1) and (2), respectively) for each critical angle considered ($\psi = 0, \pi$), reported in the plot with bluish colors for $\psi = \pi$ and reddish colors for $\psi = 0$. In the enlargements of Figure 3.2 (see Figure 3.3), on the left there are reported the stability characteristics of the equilibrium points: the points characterised by a change in the stability are called bifurcation points, and those are populating the bifurcation map.
In this work, additional equilibrium points in first resonance are identified, which are not yet present in the literature (see Gkolias et al. [15] and Alessi et al. [14]). Those points are located typically at very high eccentricities; even if they are not of a practical interest, they are reported in this work for the sake of completeness. As an example, lets examine the Figure 3.2 and Figure 3.3. As already stated before, Equation (3.26) has at maximum two solution, this resulting in two pairs of bifurcation diagrams (see the figure). Referring to the plot on the left of Figure 3.3, along the first solution (upper pair in the figure) for $\tilde{\Pi}_0 = -10\ \sqrt{km}$, there are five equilibria: three in $\psi = \pi$ and two in $\psi = 0$. Instead, zooming in the far right part of that diagram (see right plot Figure 3.3) it is possible to appreciate other two equilibria: one in $\psi = 0$ and one in $\psi = \pi$, for very high eccentricities (see also an additional example of bifurcation diagram at $a = 8078$ km, AMR $= 1\ m^2$/kg

in Figure 3.4). These latter were not present in the papers by Gkolias et al. [15] and Alessi et al. [14].

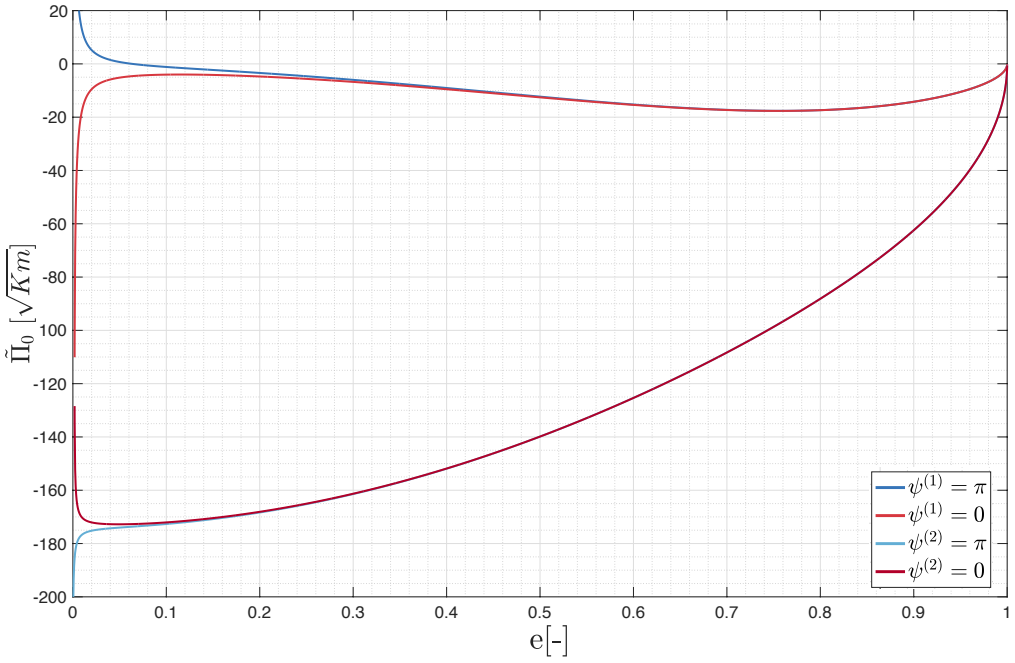

Figure 3.2: Bifurcation diagram of equilibrium points at $\psi = 0$ and $\psi = \pi$ at $a = 12078$ km and AMR $= 1\ m^2/\text{kg}$. With (1) and (2) are identified the first and the second solutions.

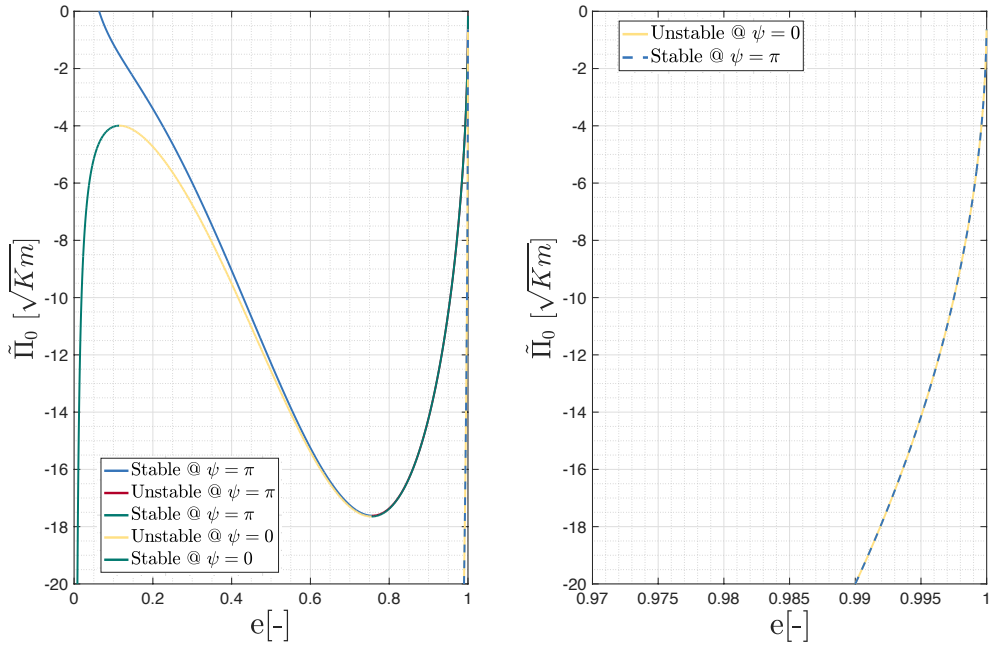

Figure 3.3: Enlargements of Figure 3.2. On the left on $\tilde{\Pi}_0 \in [-20, 0]\ \sqrt{km}$ and on the right enlarged on very high eccentricity ranges to see the 6th and 7th equilibrium.

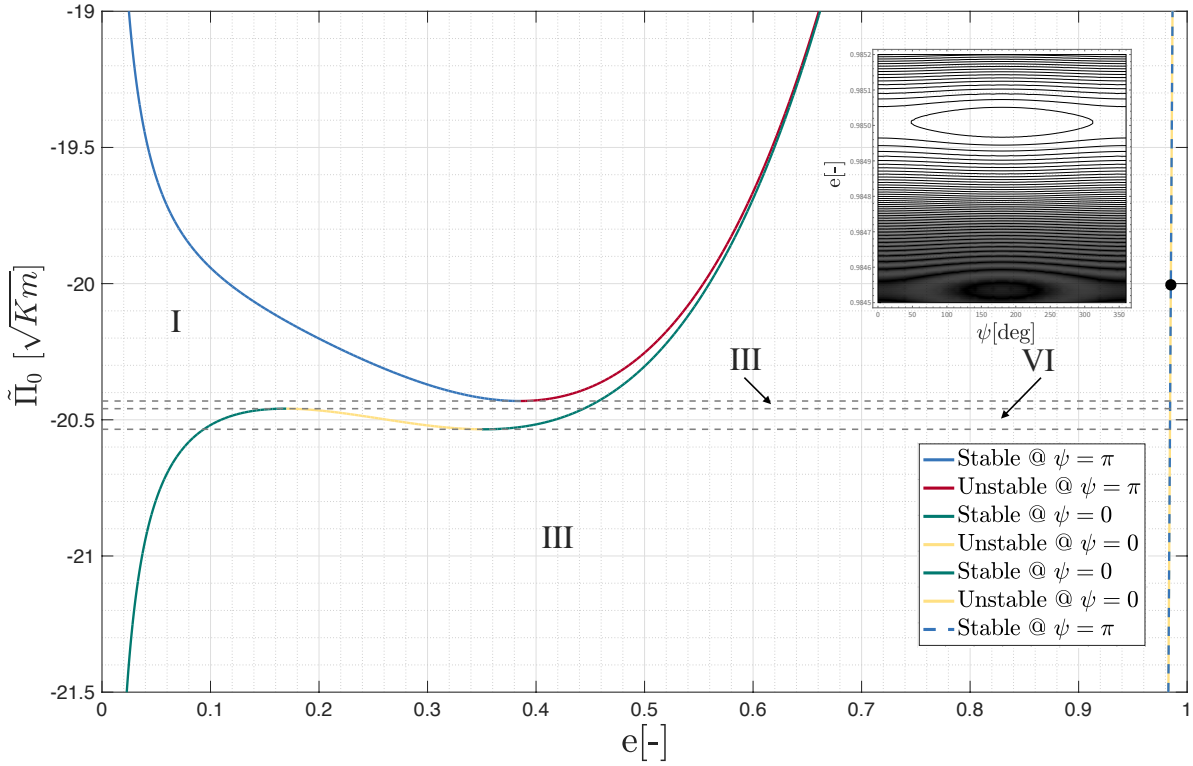

Figure 3.4: Bifurcation diagram of equilibrium points at $\psi = 0$ and $\psi = \pi$ at 8078 km and AMR $= 1\ m^2/\text{kg}$. On the plot the phase space at $\tilde{\Pi}_0 = -20\ \sqrt{km}$, highlighting the equilibria at very high eccentricity.

Figure 3.5 shows the complete bifurcation map at AMR $= 1\ m^2/\text{kg}$, with red lines are reported the bifurcations occurring along the first solution of Equation (3.26) and with blue lines the ones occurring at the second solution. With dashed lines are identified the saddle-points type bifurcations, instead, with bold line the trans-critical.
In Figure 3.6a, Figure 3.6b and Figure 3.7, the bifurcation map is depicted in detail. In addition, the phase spaces at $a = 7900$ km, 8078 km, and 8400 km are depicted to the right of each plot.
The first diagram depicts the bifurcation phase spaces at (A) and (B), where (A) describes the transition between regions I and III and (B) between regions VI and III. Similarly, the phase spaces of the bifurcation between regions I and III, III and VI, and VI and III are reported in Figure 3.6b. In the latter, the transitions between I and II, II and VI, and VI and III are shown.
Each of the aforementioned transitions causes a change in the dynamical structure; specifically, it affects the number and stability of equilibrium points.

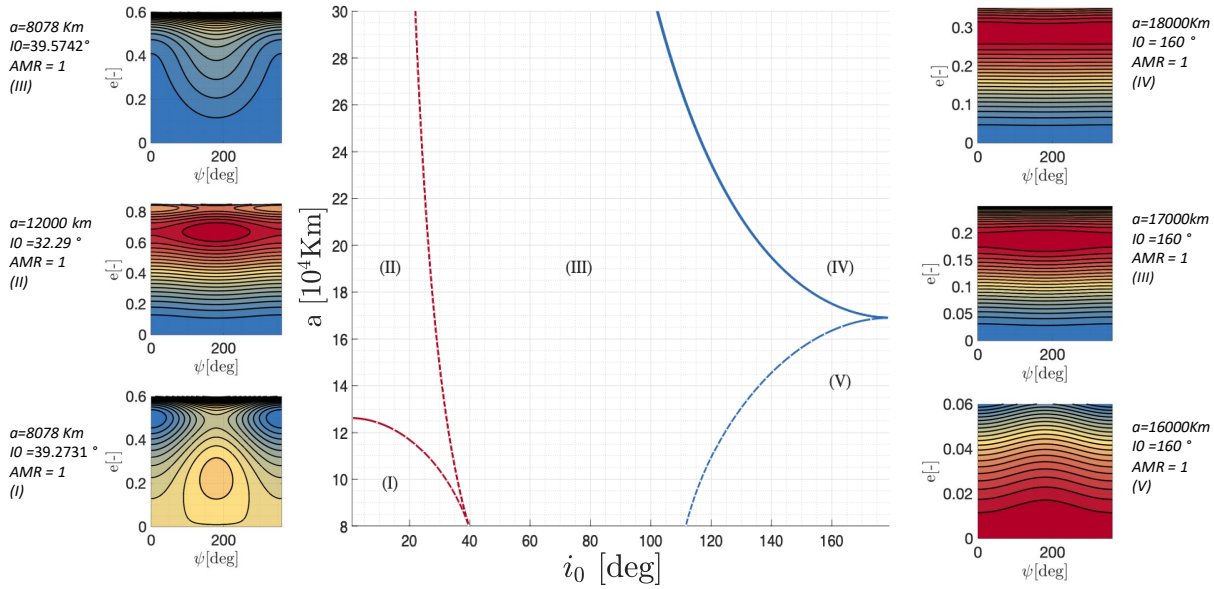

Figure 3.5: Bifurcation map of the resonant term ψ_1 with AMR $= 1\ m^2/\text{kg}$. On the sides are reported the peculiar phase space appearing in the five identified regions.

In detail, from these plots the dynamical characteristics of the regions I, III and VI, can be explained:

- region (I) is characterised by two stable points in $\psi = \pi$, one unstable point in $\psi = \pi$, one stable point in $\psi = 0$ and one unstable point in $\psi = 0$. It is possible to see in Figure 3.8a a representative phase space portrait of this region, for $\tilde{\Pi}_0 = -20.3\ \sqrt{km}$;
- region III is characterised by one stable point in $\psi = \pi$, one stable point in $\psi = 0$ and one unstable point in $\psi = 0$. In Figure 3.8b and Figure 3.9b are reported the representative phase space portraits of this region, for $\tilde{\Pi}_0 = -20.45\ \sqrt{km}$ and $\tilde{\Pi}_0 = -20.6\ \sqrt{km}$;
- region VI is characterised by one stable point in $\psi = \pi$, two stable point in $\psi = 0$ and two unstable point in $\psi = 0$. It is possible to see in Figure 3.9a a representative phase space portrait of this region, for $\tilde{\Pi}_0 = -20.5\ \sqrt{km}$.

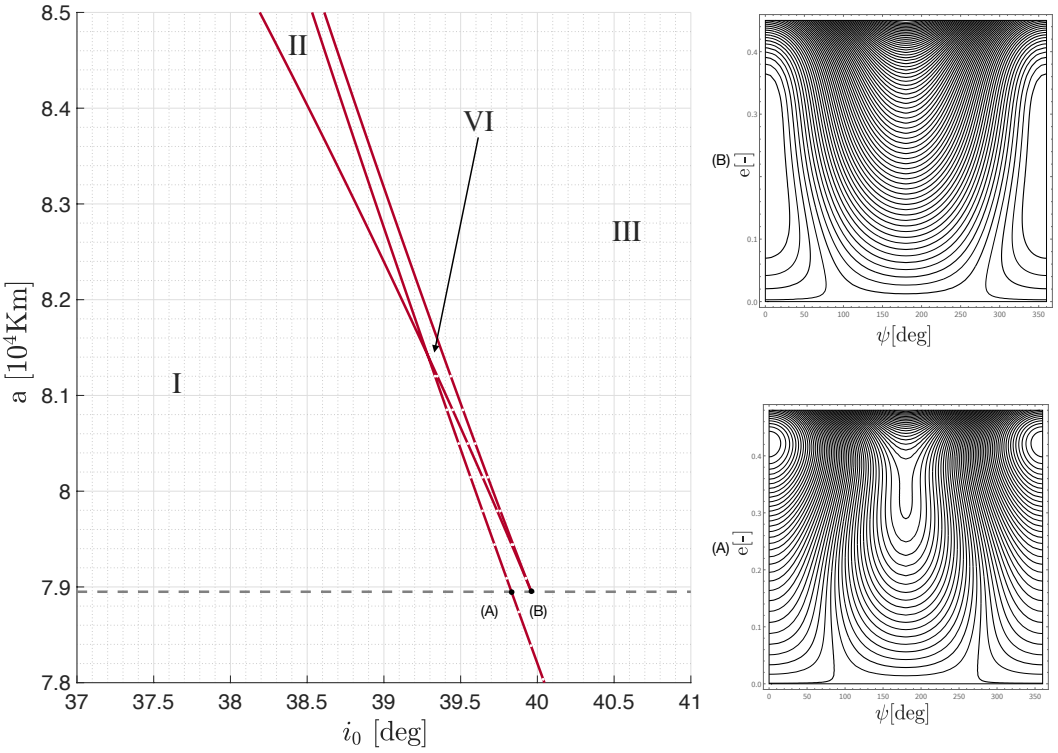

(a)

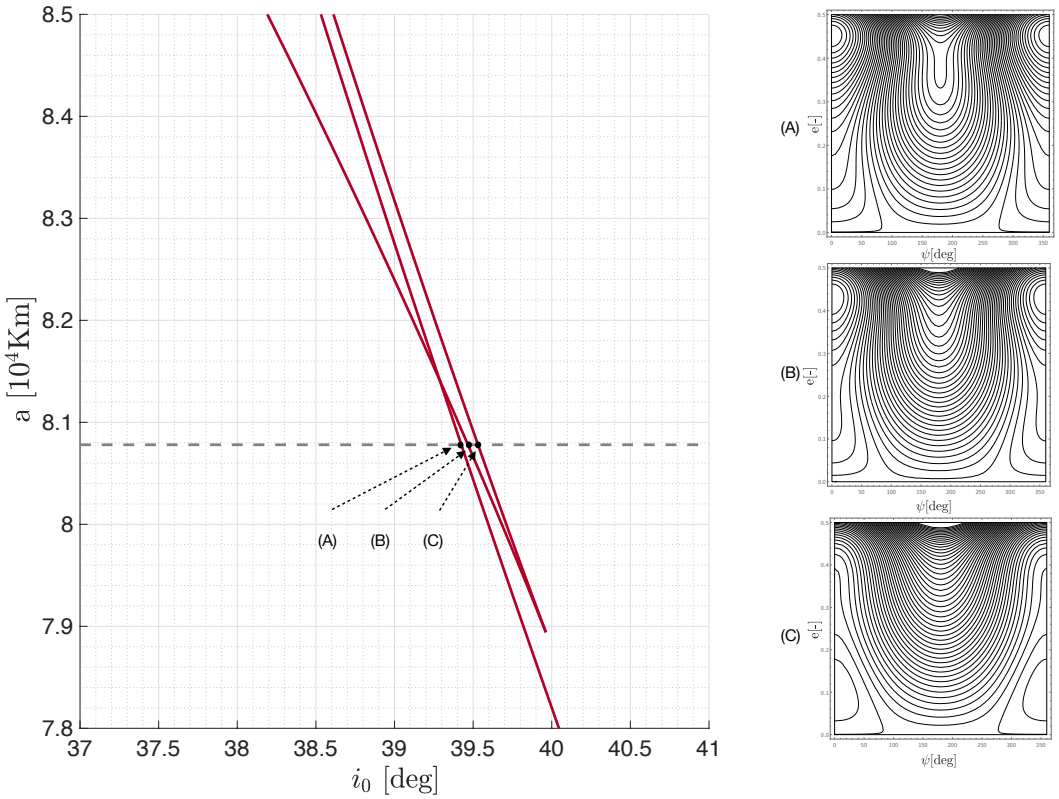

(b)

Figure 3.6: On Figure 3.6a phase space of the bifurcation appearing at $a = 7900$ km and on Figure 3.6b at $a = 8078$ km.

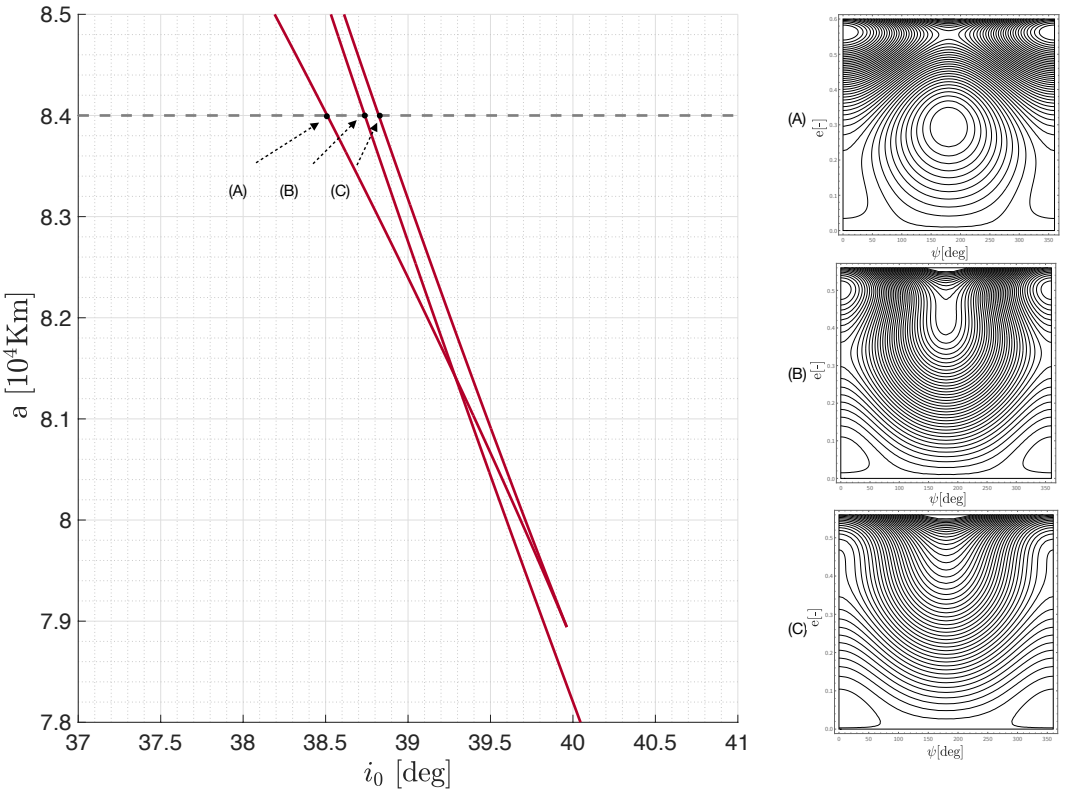

Figure 3.7: Bifurcation map detail at semi-major axis of 8400 km and AMR = 1 m^2/kg

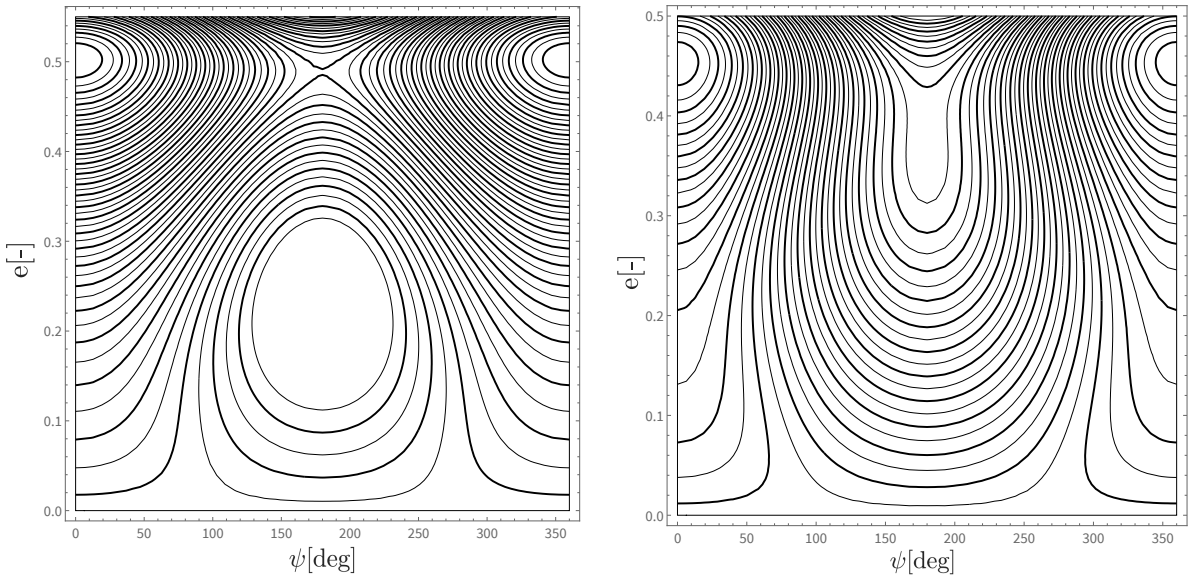

(a) (b)

Figure 3.8: Figure 3.8a the phase space at a = 8078 km at $\tilde{\Pi}_0 = -20.3\ \sqrt{km}$ and in Figure 3.8b at $\tilde{\Pi}_0 = -20.45\ \sqrt{km}$ and AMR = 1 m^2/kg.

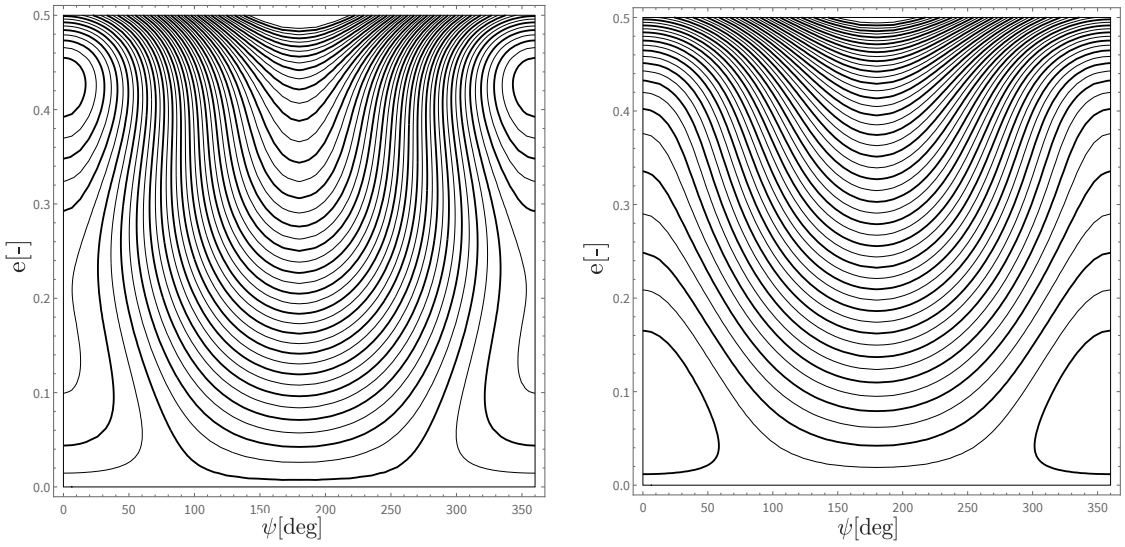

(a) (b)

Figure 3.9: Figure 3.9a the phase space at $a = 8078$ km at $\tilde{\Pi}_0 = -20.5\ \sqrt{km}$ and in Figure 3.9b at $\tilde{\Pi}_0 = -20.6\ \sqrt{km}$ and AMR= 1 m^2/kg.

As stated above, the first difference with the literature is that, referring to Figure 3.7, at $a = 8400$ km, the phase space has seven points, rather than five: two stable points in $\psi = 0$ and $\psi = \pi$, two unstable points in $\psi = 0$ and one unstable in $\psi = \pi$.
The second novelty introduced by this work, is one new dynamical region in the bifurcation map, labelled as VII in Figure 3.10. The diagrams on the right of Figure 3.10 depict the bifurcation phase spaces: A represents the phase space of the bifurcation that divides region IV from region VII, B divides region VII from region III, and V divides region III from region V. In detail, from these plots the dynamical characteristics of the regions IV and VII, can be explained:

- region IV is characterised by one stable point in $\psi = \pi$, one unstable point in $\psi = \pi$ and one stable in $\psi = 0$. The phase space is represented in the left plot of Figure 3.11 at $a = 17240$ km and $\tilde{\Pi}_0 = -260\ \sqrt{km}$;
- region VII is characterised by two stable points in $\psi = 0$ and one stable point $\psi = \pi$. The phase space is represented in the right plot of Figure 3.11 at $a = 17240$ km and $\tilde{\Pi}_0 = -258.1\ \sqrt{km}$;

The bifurcation separating the region III from IV is called trans-critical, and it is characterised by a change only in the stability characteristics of the equilibrium points, not in their number. In particular, the transformation from III to IV is achieved through the transition region VII.

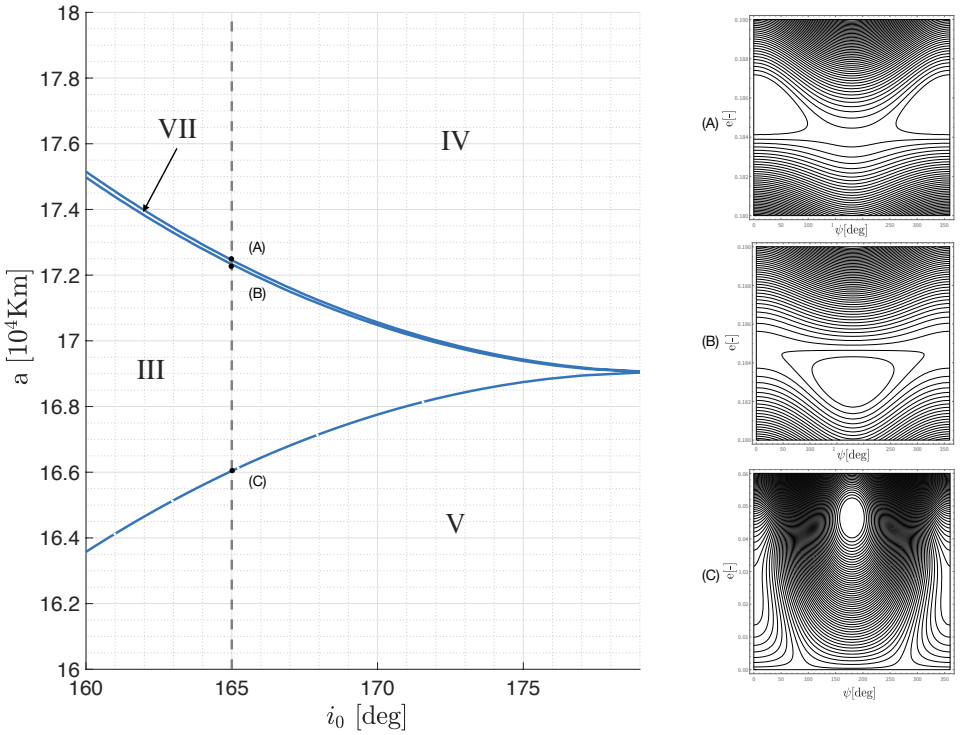

Figure 3.10: Trans-critical bifurcation at $i_{e=0} = 165°$, AMR $= 1\ m^2$/kg. On the right the phase space appearing in the bifurcation points.

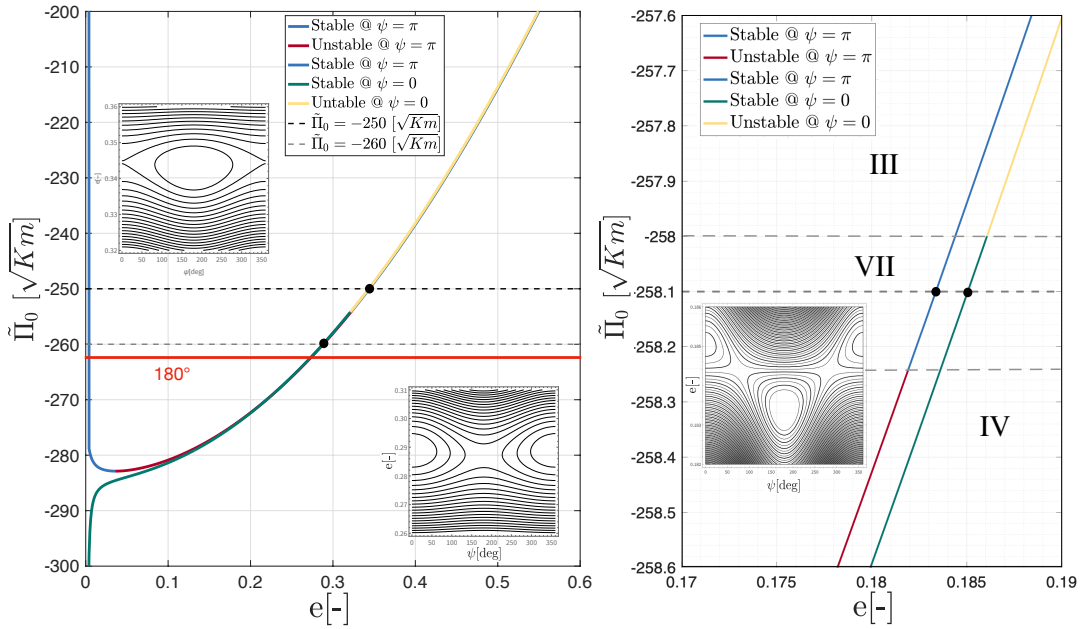

Figure 3.11: Left: bifurcation diagram at semi-major axis of 17240 km and AMR $=$ $1\ m^2$/kg showing the trans-critical bifurcation and the imperfect pitchfork bifurcation (with phase space). Right: zoom in of the bifurcation diagram showing the trans-critical bifurcation (with phase space).

It is possible to appreciate in this last graph (Figure 3.12) at $a = 10000$ km and $\tilde{\Pi} = -145.6\ \sqrt{km}$, the presence of an *imperfect pitchfork* bifurcation. It separates the region III from the region V, in which there is only one stable point in $\psi = \pi$.

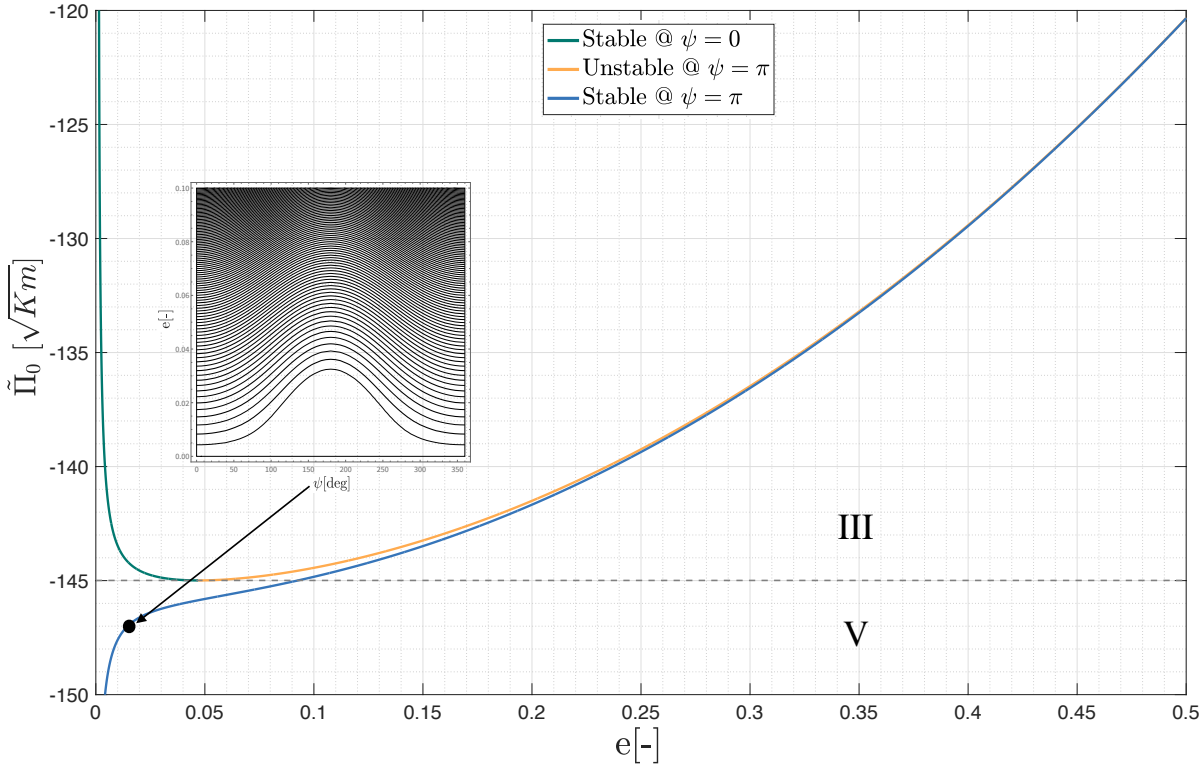

Figure 3.12: Bifurcation diagram at semi-major axis of 10000 km and AMR = 1 m^2/kg showing the imperfect pitchfork bifurcation separating the region III from (V).

In Table 3.4 the characteristics of the regions identified in Figure 3.5 are summarised:

Table 3.4: Number of equilibria and their stability (S: stable, U: unstable) for the resonance with argument ψ_1, corresponding to the seven regions of Figure 3.5.

Region	Total	$\psi = 0$	$\psi = \pi$
I	5	1S and 1U	2S and 1U
II	7	2S and 2U	2S and 1U
III	3	1S and 1U	1S
IV	3	1S	1S and 1U
V	1	-	1S
VI	5	1S	2S and 2U
VII	3	2S	1S

Dependence of the bifurcation map on AMR

Despite the bifurcations depend on the AMR, in Figure 3.13, were bifurcation map of AMR $= 1\ m^2/\text{kg}$ and AMR $= 10\ m^2/\text{kg}$ are compared, it is possible to see that, globally, the shape of the bifurcation map does not change.

The effect of increasing the AMR is reflected in the amplification and shifting towards higher altitude of some regions: on the left side of the map it is possible to see that the intersection of the diagram with the inclination $i_0 = 0°$ shifts towards higher semi-major axis, while the trans-critical bifurcation region amplifies. However, the phase space characteristic shapes are the same in the regions identified.

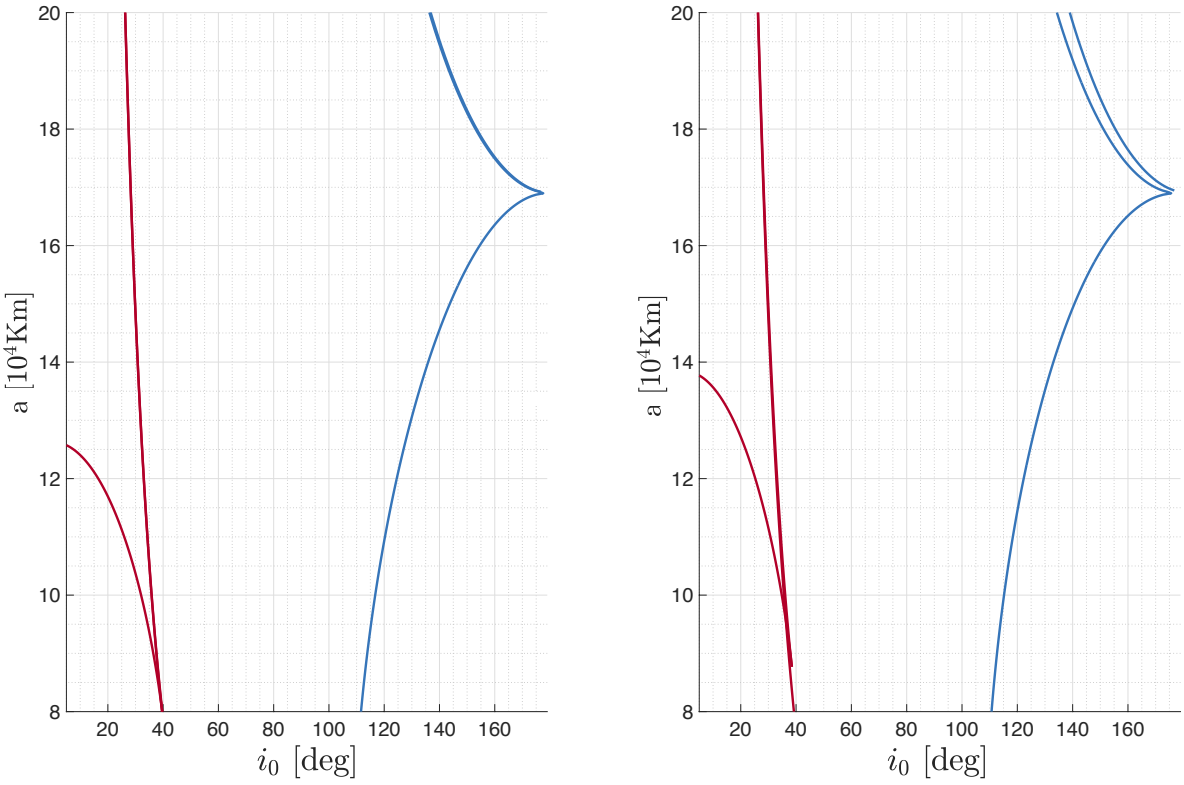

Figure 3.13: Left: bifurcation map of the resonant term ψ_1 with AMR $= 1\ m^2/\text{kg}$, right: bifurcation map of the resonant term ψ_1 with AMR $= 10\ m^2/\text{kg}$.

Saddle-point connection

The saddle-point connection bifurcation shown in Figure 3.14 takes place when, at a certain inclination i_0 (or $\tilde{\Pi}_0$), the Hamiltonian $\mathcal{H}_j$ evaluated at an unstable point $\mathcal{U}_0$ at $\psi = 0$ has the same value of the unstable point $\mathcal{U}_\pi$ at $\psi = \pi$.

The resulting phase space (see Figure 3.14) presents a trajectory which connects those points.

At the bottom right the specific case of the intersection point connecting the unstable curves in the plane $(\tilde{\Pi}_0, \mathcal{H}_j)$, is reported. The aforementioned bifurcation has already been investigated in Gkolias et al. [15], however, they have not reported in the bifurcation map the line corresponding to the bifurcation.

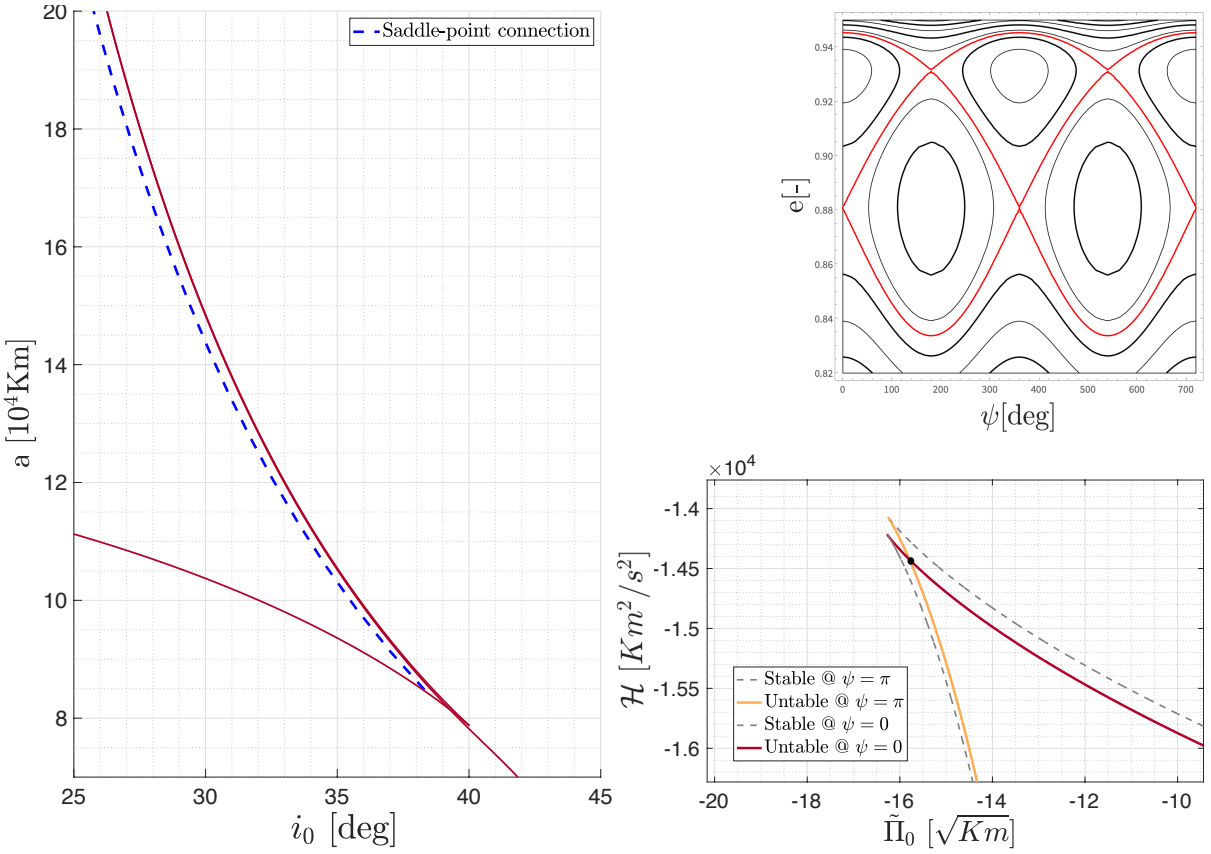

Figure 3.14: Left: Position of the bifurcation points associated to the saddle-point connection in the plane (a, i_0). On the top right, the phase space with in red line the saddle-point connection line associated to the semi-major axis of 20000 km at AMR = 1 m^2/kg and on the bottom right the bifurcation point in the plane ($\tilde{\Pi}_0$, $\mathcal{H}$).

3.4.2. Notes on the other resonances

The bifurcation analysis of the remaining resonances is not conducted for the purposes of this thesis. This is because the purpose of this paper is to describe the methodology underlying this analysis so that other readers can continue these studies. In the subsequent chapters, all analyses and results must be interpreted as pertaining to the first resonance only.

4 | Extended model of the coupled solar radiation pressure, J_2 and Sun gravity dynamic

In this Chapter the state-of-art single-resonance Hamiltonian model is extended including also the effect of Sun gravitational perturbation.
Many authors (see Section 1.1.1), have studied the dynamics of HAMR objects subject only to SRP and Earth oblateness forces. This hypothesis, as stated in Gkolias et al. [15], is valid within certain range of altitude, inclination, eccentricity and, for high value of AMR. In Gkolias et al. [15], for the value of (a, e, i) and AMR considered, the contribute of the Hamiltonian of the Sun gravitational perturbation $\mathcal{H}_{\odot}$ is negligible with respect to the one of the SRP following $\mathcal{H}_{SRP}$. Therefore, the following relation holds :

$$\left| \frac{\mathcal{H}_{\odot j}}{\mathcal{H}_{SRP,j}} \right| << 1 \tag{4.1}$$

where j is the resonance considered. However for some specific ranges of the elements mentioned abode the relation is no longer valid, hence a more complete model has to be considered.

4.1. Taxonomy of extended solar radiation pressure, Earth oblateness and Sun gravity Hamiltonian model

The following Chapter outlines the hypothesis and the derivation of the extended Hamiltonian model mentioned above. The analysis are composed of the following topics :

- Definition of modelling hypothesis and the derivation of the dynamical model;
- Definition of the Hamiltonian model and its transformation to a single DoF au-

tonomous function to which, the tools of system theory reported below, are applied;

- *Stability analysis*: for each equilibrium points, the stability properties are computed;
- *Bifurcation analysis*: for each resonance, the change in the dynamical the structure (i.e. the position of the equilibrium points) as a function of physical parameters (i.e. AMR) and obsculating parameters (i.e. a, e, i) is traced;
- *Phase space analysis*: the phase space in the plane (ψ, e) is analysed for each of the dynamical region identified.

4.1.1. Hamiltonian formulation

In the following Section, the Hamiltonian function of the gravitational perturbation is derived following the derivation by Lara et al. [45]. Then, the single-averaged autonomous Hamiltonian model is derived using the mathematical tools presented in Chapter 3.

Hypotheses

The hypotheses behind the formulation of the Sun third-body extension of the SRP-J_2 model are the same stated in Chapter 3. In addition to that:

- the Sun is lying on a circular orbit on the ecliptic plane at 1AU distance from the center of the Earth;
- the precession of the equatorial plane over the ecliptic is neglected, which is known (see Lara et al. [45]) to have a long-term effect, on time scales of decades.

The presence of the Moon is neglected because it has not the same resonant term of the Sun, however it is possible to reduce it to an autonomous 1 DoF Hamiltonian only after a double-average process around two subsequent fast-angles as done by Gkolias et al. and Lara et al. in [43]. This statement is not always valid because its effect depends highly on the initial Keplerian parameters and AMR value (see Casanova et al. [29]); however, as stated by Wang et al. in [96], near the Sun apsidal resonance its effect is really negligible. In the following, the SRP-J_2 Hamiltonian is expanded with the singly-averaged second-order Hamiltonian components of the Sun gravitational perturbation having the same resonant argument of the SRP as Gkolias et al [15] have previously reported.

Hamiltonian of the Sun gravity perturbation

The perturbing potential of a third-body on spacecraft close to a central body can be expressed as a power series of the parallactic factor (r/r_{3b}) (see Lara et al. [45]):

$$\mathcal{V}_{3b} = -\frac{\mu_{3b}}{r_{3b}} \sum_{j\geq 2} \left(\frac{r}{r_{3b}}\right)^j P_j \cos\gamma = -\beta \frac{n_{3b}^2 a_{3b}^3}{r_{3b}} \sum_{j\geq 2} \left(\frac{r}{r_{3b}}\right)^j P_j \cos\gamma \tag{4.2}$$

where $\beta = m_{3b}/(m_{3b}+m)$ is the third-body reduced mass, a_{3b} is the semi-major axis of the third-body orbit, n_{3b} is the mean motion of the third-body orbit, P_j are Legendre polynomials, and $\cos\gamma$ the scalar product between the position of the object and the Sun. Note that the term $-\mu_{3b}/r_{3b}$ has been neglected because it has no effect on the equations of motion in the restricted problem approximation.
Then, the position of the perturber $\vec{r}_{3b} = \vec{r}_\odot$ is written in the Earth equatorial frame:

$$(x_\odot, y_\odot, z_\odot)^{\mathrm{T}} = R_3(-h_\odot) R_1(-\varepsilon) R_3(-\theta_\odot)(r_\odot, 0, 0)^{\mathrm{T}} \tag{4.3}$$

where $h_\odot = -\dot{\theta} t$ is the argument of the node of the Sun apparent orbit about the Earth in the rotating frame, ε is the obliquity of the ecliptic, and θ is the Sun argument of the latitude. The Sun disturbing potential is then obtained from Equation (4.3) by computing:

$$\cos\gamma = \frac{x x_\odot + y y_\odot + z z_\odot}{r r_\odot} \tag{4.4}$$

where $x_\odot, y_\odot, z_\odot, r_\odot$ and x, y, z, r are the Sun and spacecraft coordinates in Earth equatorial frame, respectively. The coordinates of the spacecraft can be written in term of Keplerian parameters:

$$(x, y, z)^{\mathrm{T}} = R_3(-\Omega) R_1(-i) R_3(-\theta)(r, 0, 0)^{\mathrm{T}}. \tag{4.5}$$

Then, the Equation (4.4),Equation (4.5) are replaced in Equation (4.2) and only the first order expansion, is retained.
The secular and long-periodic terms of the Sun potential are derived by averaging the satellite mean anomaly over one period under the assumption that the Sun remains stationary throughout this interval. This averaging can be done in closed form by introducing the elliptic anomaly of the satellite E, by using the known ellipse relations: $r\sin(f) = a(1-e^2)\sin(E)$, $r\cos(f) = a(\cos(E) - e)$, $r = a(1-e^2)/(1+e\cos(f))$ and $\mathrm{d}M = (r/a)\mathrm{d}E$. The averaging process results in (see Lara et al. [45]):

$$\bar{\mathcal{H}}_{\odot} = -\frac{a^2 n_{\odot}^2}{64} \sum_{i=0}^{2} \sum_{j=-2i}^{2} \sum_{p=-1}^{1} \mathcal{Y}_i K_{2i,l,2p} \times \cos(2i\omega + l\Omega + 2p\lambda_{\odot}) \tag{4.6}$$

where the coefficients $\mathcal{Y}_i, K_{2i,l,2p}$ are reported in Table 4.1,

Table 4.1: Sun gravity resonant terms. Coefficient $\mathcal{Y}_i$ and $\mathcal{K}_{2i,l,2p}$ in Equation (4.6) taken from Lara et. al. [45].

i	l	p	$\mathcal{K}_{2i,j,2p}$	$\mathcal{Y}_i$	ϕ	j
1	2	-1	$\frac{1}{4}(1+c_\epsilon)^2(1+c_i)^2$	$30e^2$	$2\omega + 2\Omega - 2\lambda_\odot$	1
1	-2	1	$\frac{1}{4}(1+c_\epsilon)^2(1-c_i)^2$	$30e^2$	$2\omega - 2\Omega + 2\lambda_\odot$	2
2	0	-2	$\frac{3}{2}s_\varepsilon^2 s_i^2$	$30e^2$	$2\omega - 2\lambda_\odot$	3
2	0	2	$\frac{3}{2}s_\varepsilon^2 s_i^2$	$30e^2$	$2\omega + 2\lambda_\odot$	4
1	1	1	$-\frac{1}{4}(c_\epsilon-1)^2(c_i+1)^2$	$30e^2$	$2\omega + 2\Omega + 2\lambda_\odot$	5
-1	1	1	$\frac{1}{4}(c_\epsilon-1)^2(c_i-1)^2$	$30e^2$	$-2\omega + 2\Omega + 2\lambda_\odot$	6

which for specific values of integers (i, l, p) contains the same resonant terms as Equation (3.14). The Equation (4.6) just derived is the same reported in Gkolias et al. [15]. In this work, this contribute is added to the state-of-art model and then analysed using the tool of the bifurcation analysis.

Extended model of coupled SRP, J_2 and Sun gravity dynamics

The coupled SRP, Earth oblateness and Sun gravitational perturbation model (from here SRP-J_2-Sun) is derived summing up Equation (3.14) and Equation (4.6):

$$\bar{\mathcal{H}} = \bar{\mathcal{H}}_{J_2} + \bar{\mathcal{H}}_{\text{SRP}} + \bar{\mathcal{H}}_{\odot} \tag{4.7}$$

which is, highlighting all the terms:

$$\begin{aligned} \bar{\mathcal{H}} = \bar{\mathcal{H}}_{J_2} + \bar{\mathcal{H}}_{\text{SRP}} + \bar{\mathcal{H}}_{\odot} = \frac{\mathcal{C}_{J_2}(1-3c_i^2)}{4a^3(1-e^2)^{3/2}} - ae\mathcal{C}_{SRP} \sum_{j=1}^{6} \mathcal{T}_j \cos\psi_j + \\ - \frac{a^2 n_{\odot}^2}{64} \sum_{j=1}^{6} \mathcal{Y}_j K_j \cos 2\psi_j \end{aligned} \tag{4.8}$$

with $j = 1$ to 6 is the index associated to the resonances. The Equation (4.8) has already been derived in literature (see Casanova et al. [29], Lemaitre [48], Celletti et al. [54], and Valk et al. [52]). However, neither the single-resonance formalism nor the bifurcation analysis of the Hamiltonian have been provided.

Isolated resonance model

The most interesting thing to note is the shape of this new extended model. As shown in Breiter [38], Winter and Murray [41], it has the form of a Second Andoyer Fundamental Model of resonance, in the shape of :

$$\mathcal{K} = \mathcal{A}(\Phi, \Psi) + \mathcal{B}_1(\Phi, \Psi)\cos\phi + \mathcal{B}_2(\Phi, \Psi)\cos 2\phi \tag{4.9}$$

where, $\mathcal{A}$ is associated with the contribute of the secular J_2, and the $\mathcal{B}_{1,2}$ are associated to the contribute of SRP and Sun gravity, respectively.

Following the same procedure in Gkolias et al. [15] and Breiter [38], the Hamiltonian can be expressed in terms of the canonical Delaunay elements (L, G, H, l, g, h) such that:

$$L = \sqrt{\mu a},\;\; l = M;\;\; G = L\sqrt{1-e^2},\;\; g = \omega;\;\; H = G\cos i,\;\; h = \Omega \tag{4.10}$$

to obtain:

$$\begin{aligned}\bar{\mathcal{H}} = \frac{\mathcal{C}_{J_2}\mu^3(G^2-3H^2)}{4G^5L^3} - \frac{\mathcal{C}_{\mathcal{SRP}}\sqrt{1-G^2/L^2}L^2}{\mu}\sum_{j=1}^{6}\mathcal{T}_j\cos\psi_j + \\ -\frac{L^4 n_\odot^2}{64\mu^2}\sum_{j=1}^{6}\mathcal{Y}_j K_j\cos 2\psi_j\end{aligned} \tag{4.11}$$

where for the coefficients $\mathcal{T}_j$, K_j and $\mathcal{Y}_j$ the relationships $c_i = H/G$, $s_i = \sqrt{1-H^2/G^2}$ and $e^2 = 1 - G^2/L^2$ holds and with the resonances reported in Table 4.1. Due to the averaging process, Equation (4.11) does not depend on the mean anomaly $M = l$ and thus the Delaunay action L, as well as the semi-major- axis, is constant. The system has two DoFs and one explicit time dependence through $\lambda_\odot(t) = \lambda_{\odot,0} + n_\odot t$. Considering an extended phase space, a dummy action I_s with frequency $n_\odot$ is added to the Hamiltonian:

$$\bar{\mathcal{H}} = \bar{\mathcal{H}}_{J_2} + \bar{\mathcal{H}}_{\text{SRP}} + \bar{\mathcal{H}}_\odot + n_\odot I_s \tag{4.12}$$

which yields a three DoFs autonomous system. For each resonance with argument ψ_j a resonant set of variables $(\Psi\ ,\ \psi)$ is introduced via a unimodular transformation of the Delaunay elements $(\Psi, \psi, \Pi, \pi, K, \kappa)$ as done in Gkolias et al. [15]. The transformed Hamiltonian is described by the single degree of freedom ψ and by its conjugate momentum Ψ:

$$\begin{aligned}\bar{\mathcal{H}} = \bar{\mathcal{H}}_{J_2}(\Psi; L, \Pi) + \bar{\mathcal{H}}_{\mathrm{SRP,j}}(\Psi, \psi; L, \Pi) + \\ + \bar{\mathcal{H}}_{\odot,j}(\Psi, \psi; L, \Pi) + n_\odot(n_3\Psi + K)\end{aligned} \tag{4.13}$$

where :

$$\bar{\mathcal{H}}_{\odot,j}(\Psi, \psi; L, \Pi) = -\frac{L^4 n_\odot^2}{64\mu^2}\mathcal{Y}_r K_r \cos 2\psi_j \tag{4.14}$$

Using the same notation as Equation (4.9):

$$\bar{\mathcal{H}} = \mathcal{A}_{J_2} + \mathcal{B}_{\mathrm{SRP},j}\cos\psi_j + \mathcal{B}_{\odot,j}\cos 2\psi_j + n_\odot(n_3\Psi + K) \tag{4.15}$$

The coefficients $\mathcal{T}_r$, K_r and $\mathcal{Y}_r$ are expressed in terms of the new variables using the equations $c_i = \frac{n_1 n_2 \Psi + \Pi}{n_2^2 \Psi}$, $s_i = \sqrt{1 - c_i^2}$ and $e^2 = 1 - n_1^2\Psi^2/L^2$. Due to the resonant transformation both π and κ are ignorable, hence $\mathit{\Pi}$ and K are constants. The action variable $\mathit{\Pi}$ is a resonant integral of the system which is useful to recover the inclination from the eccentricity and the resonance considered. The second integral of motion $\mathit{\Pi}$ is the same defined for the SRP-J_2 model; to prove it, Equation (4.13) is substituted in Equation (C.6) the. Using the same notation as in Equation (4.9), the partial derivatives of $\mathcal{R}$ with respect to ω and Ω are:

$$\begin{aligned}\frac{\partial\mathcal{H}}{\partial\omega} &= n_1\mathcal{B}_{\mathrm{SRP}}\sin\psi_j + 2n_1\mathcal{B}_\odot\sin 2\psi_j, \\ \frac{\partial\mathcal{H}}{\partial\Omega} &= n_2\mathcal{B}_{\mathrm{SRP}}\sin\psi_j + 2n_2\mathcal{B}_\odot\sin 2\psi_j,\end{aligned} \tag{4.16}$$

and hence, their quotient :

$$\frac{\partial\mathcal{R}/\partial\Omega}{\partial\mathcal{R}/\partial\omega} = \frac{\partial\mathcal{H}/\partial\Omega}{\partial\mathcal{H}/\partial\omega} = \frac{n_2}{n_1}, \tag{4.17}$$

which is the same argument as in Equation (C.1), proving that the extended single-resonant autonomous Hamiltonian has the same second integral of motion as the SRP-J_2 model.

4.1.2. Equilibrium points

From the Hamiltonian formalism, it is known that apart from $\mathcal{H}$, the isolated resonance system has two constants of motion: the semi-major- is constant due to averaging, and the

second integral Π. The inclination of the corresponding circular orbit can be used to label the values of Π. A phase space is uniquely identified given a set of values for the dynamical parameters (a, i_{circ}) and the engineering parameter AMR. The number of equilibrium points and their stability can be defined in this phase space and thus a bifurcation diagram can be computed by varying the parameters and tracking the structural changes in the system. Elliptic and saddle points appear, as well as disappear, based on the classical bifurcation theory for 1-DoF systems.

Equilibrium points in (Ψ, ψ) and (e,ψ)

The equation of motions relative to the coordinate (Ψ, ψ) can be derived from the resonant Hamiltonian Equation (4.15):

$$\dot{\psi} = \frac{\partial \mathcal{H}}{\partial \Psi}, \quad \dot{\Psi} = -\frac{\partial \mathcal{H}}{\partial \psi} \tag{4.18}$$

or, substituting the variable (ψ, e):

$$\dot{\psi} = -n_1 \frac{\sqrt{1-e^2}}{e\sqrt{\mu a}} \frac{\partial \mathcal{H}}{\partial e}, \quad \dot{e} = n_1 \frac{\sqrt{1-e^2}}{e\sqrt{\mu a}} \frac{\partial \mathcal{H}}{\partial \psi} \tag{4.19}$$

The equilibrium are computed imposing null gradient:

$$\dot{\psi} = 0 \rightarrow \frac{\partial \mathcal{H}}{\partial e} = 0, \quad \dot{e} = 0 \rightarrow \frac{\partial \mathcal{H}}{\partial \psi} = 0 \tag{4.20}$$

Making explicit the gradients in Equation (4.19):

$$\begin{aligned} \nabla \mathcal{H}_{\psi,j} &= -\mathcal{B}_{\mathrm{SRP},j} \sin \psi_j - 2\mathcal{B}_{\odot,j} \sin 2\psi_j, \\ \nabla \mathcal{H}_{e,j} &= \frac{\partial \mathcal{H}_{J_2}}{\partial e} + \frac{\partial \mathcal{B}_{\mathrm{SRP},j}}{\partial e} \cos \psi_j + \frac{\partial \mathcal{B}_{\odot,j}}{\partial e} \cos 2\psi_j + n_3 n_\odot \frac{\partial \Psi}{\partial e}. \end{aligned} \tag{4.21}$$

It is intuitive to see that, from the equation of $\nabla \mathcal{H}_{\psi,j}$ the critical angles are at $\psi = 0, \pi$ (here called *symmetric* equilibrium points), and at intermediate value (from here called *asymmetric* equilibrium points, pointed out only numerically by Wang et al. [57]).

Symmetric equilibrium points

Regarding the symmetric libration points, substituting $\psi = 0, \pi$ in Equation (4.20) (using the same notation as Equation (4.15) for convenience), the following equations have to be

verified separately:

$$\begin{aligned}\dot{\psi}_0 = 0 \rightarrow \frac{\partial \mathcal{A}_{J_2}}{\partial e} + \frac{\partial \mathcal{B}_{SRP,j}}{\partial e} + \frac{\partial \mathcal{B}_{\odot,j}}{\partial e} + n_3 n_\odot \frac{\partial \Psi}{\partial e} = 0,\\ \dot{\psi}_\pi = 0 \rightarrow \frac{\partial \mathcal{A}_{J_2}}{\partial e} - \frac{\partial \mathcal{B}_{SRP,j}}{\partial e} + \frac{\partial \mathcal{B}_{\odot,j}}{\partial e} + n_3 n_\odot \frac{\partial \Psi}{\partial e} = 0\end{aligned} \tag{4.22}$$

With reference to Figure 4.1 it has been plotted the phase space in the plane (ψ, e) at $a = 12000$ km, $i_{e=0} = 19.5°$ and AMR $= 0.1\ m^2/\text{kg}$. The symmetric points are spotted with red dots.

Asymmetric equilibrium points

Regarding the asymmetric libration points, the Equation (4.21) can be simplified dividing by $\sin\psi$ (avoiding $\psi = 0, \pi$) and therefore the following non-linear system has to be solved:

$$\begin{aligned}\dot{e}_{(+/-)} = 0 \rightarrow \mathcal{B}_{SRP,j} + 4\mathcal{B}_{\odot,j}\cos\psi = 0,\\ \dot{\psi}_{(+/-)} = 0 \rightarrow \frac{\partial \mathcal{A}_{J_2}}{\partial e} + \frac{\partial \mathcal{B}_{SRP,j}}{\partial e}\cos\psi + \frac{\partial \mathcal{B}_{\odot,j}}{\partial e}\cos 2\psi + n_3 n_\odot \frac{\partial \Psi}{\partial e} = 0\end{aligned}. \tag{4.23}$$

In Figure 4.1 the *asymmetric* points are labelled with blue dots. Due to the coupling with the SRP dynamics, they are not located at $\psi = \pi/2$ but rather in between $\psi = \pi/2$ and $\psi = \pi$. In particular, from the first equation of Equation (4.23):

$$\cos\psi = -\frac{\mathcal{B}_{\text{SRP}_j}}{4\mathcal{B}_{\odot,j}}, \tag{4.24}$$

which has at two pairs of solution in the form of $(\psi, e)^+$ and $(\psi, e)^-$. The signs $+$, $-$ are used to differentiate the solutions. The angles ψ^+ and ψ^- are symmetric with respect to the axis $\psi = \pi$, while their associated eccentricities (e^+ and e^-), are the same.
Later in the course of the Chapter it is proven that, although are very similar, the eccentricity of the symmetric points and asymmetric points differ.

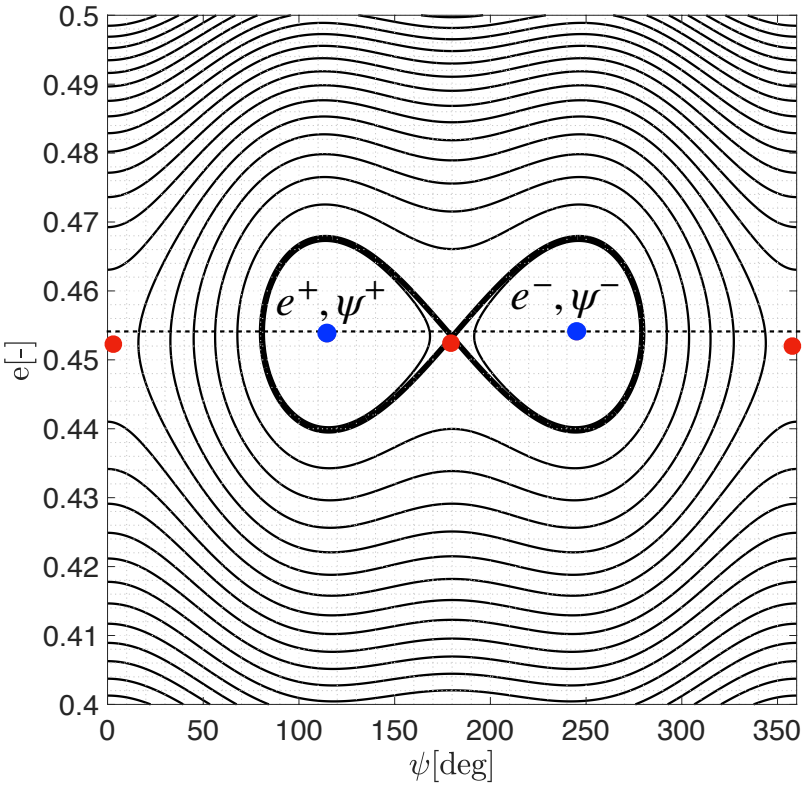

Figure 4.1: Phase space of the extended SRP-J_2-Sun model relative to the first resonance at $a = 12000$ km, $i_{e=0} = 19.5°$ and AMR $= 0.1$ $[m^2/\text{kg}]$.

4.2. Dynamical model, resonances and bifurcation analysis

The semi-analytical equation of motion of the coupled SRP-J_2 model based on the single-averaged Hamiltonian has been defined in Chapter 3. Here, considering the Hamiltonian of the extended SRP-J_2-Sun model defined in Equation (4.11), the Lagrangian equations of motion become:

$$\begin{aligned}
\frac{\partial \dot{e}_{|j}}{\partial e} &= 0, \\
\frac{\partial \dot{e}_{|j}}{\partial \psi_j} &= n_2 C_{\text{SRP}} \frac{\sqrt{1-e^2}}{na} \mathcal{T}_j \cos\psi_j + \frac{15}{8} \frac{\sqrt{1-e^2}}{n} n_2 n_\odot \mathcal{K}_j \cos 2\psi_j, \\
\frac{\partial \dot{\psi}_j}{\partial e} &= n_1 \frac{\partial \dot{\Omega}_{(J_2,\odot_j,SRP_j)}}{\partial e} + n_2 \frac{\partial \dot{\omega}_{(J_2,\odot_j,SRP_j)}}{\partial e} + n_3 n_\odot, \\
\frac{\partial \dot{\psi}_j}{\partial \psi_j} &= 0,
\end{aligned} \tag{4.25}$$

with $\dot{\Omega}_{(J_2,\odot_j,SRP_j)} = \dot{\Omega}_{J_2} + \dot{\Omega}_{SRP_j} + \dot{\Omega}_{\odot_j}$ and $\dot{\omega}_{(J_2,\odot_j,SRP_j)} = \dot{\omega}_{J_2} + \dot{\omega}_{SRP_j} + \dot{\omega}_{\odot_j}$, therefore:

$$\begin{aligned}
\dot{\Omega}_{J_2} &= -\frac{3}{2}\frac{J_2 r_\oplus^2 n}{a^2(1-e^2)^2}\cos i, \\
\dot{\Omega}_{\text{SRP}} &= C_{\text{SRP}}\frac{e}{na\sqrt{1-e^2}\sin i}\sum_{j=1}^{6}\frac{\partial \mathcal{T}_j}{\partial i}\cos\psi_j, \\
\dot{\Omega}_{\odot} &= \frac{15}{32}\frac{e^2\csc i}{\sqrt{1-e^2}}\frac{n_\odot^2}{n}\sum_{j=1}^{6}\frac{\partial \mathcal{K}_j}{\partial i}\cos 2\psi_j, \\
\dot{\omega}_{J_2} &= \frac{3}{4}\frac{J_2 r_\oplus^2 n}{a^2(1-e^2)^2}\left(5\cos^2 i - 1\right), \\
\dot{\omega}_{\text{SRP}} &= C_{\text{SRP}}\frac{\sqrt{1-e^2}}{nae}\sum_{j=1}^{6}\mathcal{T}_j\cos\psi_j - \dot{\Omega}_{\text{SRP}}\cos i, \\
\dot{\omega}_{\odot} &= \frac{15}{16}\frac{n_\odot^2}{n}\sqrt{1-e^2}\sum_{j=1}^{6}\mathcal{K}_j\cos 2\psi_j - \dot{\Omega}_{\odot}\cos i.
\end{aligned} \tag{4.26}$$

The equilibrium orbit, depending on the resonance, describes the same kind of orbit listed in Section 3.2.2, with the difference that the argument of periapsis is $n_1\dot{\Omega}_{(J_2,\odot_j,SRP_j)} + n_2\dot{\omega}_{(J_2,\odot_j,SRP_j)}$.

4.2.1. Dynamical regimes

In this Section, the basic technique for calculating the location and stability of equilibrium points associated with the extended model as a function of both physical parameters and initial elements is detailed.
A part from the obsculating Keplerian parameters, the dynamics is strongly influenced by the AMR; hence, the dynamics is classified according to the AMR of the object :

- AMR = 0 m^2/kg, thus only the dynamics due to J_2 and Sun gravity effects are retained;
- low AMR such that the contribute of SRP does not overwhelm that of the Sun gravity, but can not be neglected;
- high values of AMR such that the dynamics is mainly driven by the coupled effect of SRP and Earth oblateness.

For this scope a new parameter $\sigma_{i,j}^*$ is defined, and used to identify as the critical value of AMR such that, under certain circumstances defined below, the dynamical model collapse to the coupled SRP, J_2 model. To derive this parameter, the gradient of $\mathcal{H}$

(Equation (4.21)) with respect to (ψ, e) is explicited :

$$\begin{aligned} \nabla\mathcal{H}_{\psi,j} &= aeC_{SRP}\mathcal{T}_j \sin\psi_j + \frac{15}{16}a^2 n_\odot^2 e^2 \mathcal{K}_j \sin 2\psi_j, \\ \nabla\mathcal{H}_{e,j} &= \frac{\partial \mathcal{H}_{J_2}}{\partial e} - aC_{SRP}\mathcal{T}_j \cos\psi_j - \frac{15}{16}a^2 n_\odot^2 e\mathcal{K}_j \cos 2\psi_j + n_3 \frac{n_\odot\sqrt{\mu a}e}{\sqrt{1-e^2}}. \end{aligned} \tag{4.27}$$

From the first the critical equilibrium angle is defined as:

$$\begin{aligned} \psi &= 0, \pi \quad \text{and} \\ \cos\psi_j &= -\frac{8}{15}\frac{C_{SRP}}{an_\odot^2 e}\frac{\mathcal{T}_j}{\mathcal{K}_j} \end{aligned} \tag{4.28}$$

From the second of Equation (4.28), it is intuitive to conclude that, if $\cos\psi = -1$, the asymmetric equilibrium point is located at π, this condition is satisfied for:

$$\sigma^*_{i,j} = \frac{5}{4}\frac{\mathcal{K}_j}{\mathcal{T}_j}\frac{n_\odot^2}{P_\odot c_R} a e^{eq}_{i,j} \tag{4.29}$$

where $\sigma^*_{i,j}$ is the discriminant AMR associated to the i-th equilibrium and j-th resonance. If AMR $= \sigma^*_{i,j}$, the condition constitutes the generation of a peculiar kind of **bifurcation** which has not yet described in literature.
As a result of the dynamical regimes stated before, from here, are defined as:

- first dynamical regime for AMR $= 0$ m^2/kg;
- second dynamical regime for $0 <$ AMR $< \sigma^*_{i,j}$;
- third dynamical regime for AMR $\geq \sigma^*_{i,j}$.

Dynamical structure for AMR $= 0$

If it is assumed the spacecraft has a negligible area, the dynamics can be described by the coupled Sun gravity and Earth oblateness model. Considering the second equation of Equation (4.21), and putting $C_{\text{SRP}} = 0$:

$$\nabla\mathcal{H}_{\psi_j} = 2\mathcal{B}_{\odot,j}\sin 2\psi_j = 0, \tag{4.30}$$

it is possible to observe that the equilibrium points are at critical angles $\psi_{\odot,J_2} = 0, \frac{\pi}{2}, \pi, \frac{3\pi}{2}$, and π with corresponding eccentricity computed satisfying:

$$\dot{\psi}_{J_2,\odot_j} = n_1\dot{\omega}_{J_2,\odot_j} + n_2\dot{\Omega}_{J_2,\odot_j} + n_3 n_\odot = 0, \tag{4.31}$$

which can be conveniently reduced to a quadratic equation in the unknown $\cos i$ rearranging Equation (4.25) with $\mathcal{C}_{\mathrm{SRP}} = 0$:

$$(c_{1,J_2} + c_{1,\odot_j})\cos i^2 + (c_{2,J_2} + c_{2,\odot_j})\cos i + (c_{3,J_2} + c_{3,\odot_j}) = 0. \tag{4.32}$$

The coefficients c_1, c_2, c_3 are defined above in the dedicated resonance Section 4.2.3.

Dynamical structure for $0 <$ AMR $< \sigma^*_{i,j}$

For objects with low value of AMR the effect of the SRP on the orbital dynamics is not negligible. Under this hypothesis, the orbital dynamics is driven by the coupled SRP, Earth oblateness and Sun gravity perturbations. As already studied in Section 4.1.2, the contemporary presence of the Sun gravity, SRP and Earth oblateness effect, leads to a more complicate dynamical structure with an increased number of equilibrium points. The asymmetric equilibrium points arising from the equilibrium points at $\psi = \pi/2, 3\pi/2$, belonging to the coupled J_2-Sun gravity model, are not more located at that peculiar angular position but have to be computed solving a non-linear system of two equations Equation (4.27).

The peculiarity of this coupled model is that, as long as it is possible to consider the dynamics of an equilibrium driven by the three effects, its eccentricity positions does not depend on AMR, remaining the same computed in the J_2-Sun gravity model until its discriminant $\sigma^*_{i,j}$ is reached.

This can be demonstrated by substituting the second Equation (4.28) in the equation of $\nabla\mathcal{H}_e$:

$$\begin{aligned}\nabla\mathcal{H}_{e,j} = \frac{\partial\mathcal{H}_{J_2}}{\partial e} - aC_{SRP}\mathcal{T}_j\cos\psi - \frac{15}{16}a^2n_\odot^2 e\mathcal{K}_j\cos 2\psi + n_3n_\odot\frac{\partial\Psi}{\partial e} = \\ = \frac{\partial\mathcal{H}_{J_2}}{\partial e} + \frac{15}{16}a^2n_\odot^2 e\mathcal{K}_j - \cos\psi\left(aC_{SRP}\mathcal{T}_j + \frac{15}{8}a^2n_\odot^2 e\mathcal{K}_j\cos\psi\right) + n_3n_\odot\frac{\partial\Psi}{\partial e} = \\ = \frac{\partial\mathcal{H}_{J_2}}{\partial e} + \frac{15}{16}a^2n_\odot^2 e\mathcal{K}_j + n_3n_\odot\frac{\partial\Psi}{\partial e}.\end{aligned} \tag{4.33}$$

The term inside round brackets simplifies, therefore the gradient does not depend on the SRP contribute. The proof is valid regardless of the resonance considered; however, for the sake of clarity, in Figure 4.5, Figure 4.6, and Figure 4.7 is reported the computation done for the first resonance. Indeed, below the value of the respective discriminant AMR, the asymmetric equilibrium point eccentricity position do not change increasing the AMR of the object.

The inclination of the *asymmetric* equilibrium points for $0 <$ AMR $\leq \sigma^*_{i,j}$ is the same of

the corresponding asymmetric point computed at AMR $= 0\ m^2/\text{kg}$. This because, if the eccentricity does not change, also the inclination remains constant, because the second integral of motion is conserved.
Instead, for the *symmetric* points it is the contrary. This because, in Equation (4.27), $\nabla\mathcal{H}_{e,j}$, still depends on AMR if $\psi = 0, \pi$.
Similar to what has been done for Equation (4.32), the commensurability equation can be written as :

$$\begin{aligned}(c_{1,J_2} + c_{1,\odot_j} + c_{1,\text{SRP}_j})\cos i^2 + (c_{2,J_2} + c_{2,\odot_j} + c_{2,\text{SRP}_j})\cos i + \\ +(c_{3,J_2} + c_{3,\odot_j} + c_{3,\text{SRP}_j}) = 0.\end{aligned} \tag{4.34}$$

If it is solved for each value of (a, e, AMR) and for $\psi = 0$ or π, it is possible to compute the resonant inclination of the symmetric points [1], which now depends on AMR.
The *bifurcation* map for the points in $\psi = 0, \pi$ has been computed in the same way as the one in Chapter 3 . The stability evaluation now differs because it has to include the contribute of the Sun third-body.
In addition to the bifurcations associated to the symmetric points, a bifurcation relative to the asymmetric points arises when the AMR of the object considered is the same as the critical one. Therefore, for each value of the semi-major axis considered and in the range of eccentricities between 0 and 1, at $\psi = \pi/2$ and AMR $= 0\ m^2/\text{kg}$, together with the corresponding value of $\tilde{\Pi}_{e=0}$, the discriminant $\sigma^*_{i,j}$ is computed and compared with the considered AMR. Then, if a bifurcation exists, it is plotted in the plane (a, $i_{e=0}$).

Dynamical structure for AMR $\geq \sigma^*_{i,j}$

In the case of objects with AMR $\geq \sigma^*_{i,j}$, the asymmetric equilibrium point collapse to $\psi = \pi$, and the contribute of the Sun gravity Hamiltonian becomes negligible. Therefore, the objects motion can be considered as driven by the coupled SRP-J_2 dynamics, extensively described by many authors and also in this thesis (see Chapter 3).

4.2.2. Stability analysis

The stability of the equilibrium points can be evaluated by computing the eigenvalues of the Hessian matrix evaluated at the equilibrium point:

$$\text{Hess}(\mathcal{H})_j = \begin{pmatrix} \frac{\partial \dot{e}}{\partial e} & \frac{\partial \dot{e}}{\partial \psi} \\ \frac{\partial \dot{\psi}}{\partial e} & \frac{\partial \dot{\psi}}{\partial \psi} \end{pmatrix} \tag{4.35}$$

[1] the values of c_i are reported in the resonant-specific section

The partial derivatives $\frac{\partial \dot{e}}{\partial e}$ and $\frac{\partial \dot{\psi}}{\partial \psi}$ are zero if evaluated at the equilibrium. Therefore, the information about the stability of the point can be retrieved by evaluating the eigenvalues of the Hessian :

$$\lambda^2 - \frac{\partial \dot{e}}{\partial \psi}\frac{\partial \dot{\psi}}{\partial e} = 0 \quad \rightarrow \quad \lambda_{1,2} = \pm\sqrt{\frac{\partial \dot{e}}{\partial \psi}\frac{\partial \dot{\psi}}{\partial e}}. \tag{4.36}$$

If the sign of the term under the square root is positive, the eigenvalues are positive, hence unstable. On the other hand, if it is negative, the eigenvalues are complex conjugated, thus the orbit is periodic. The partial derivatives are the sum of the Earth oblateness, SRP and Sun gravity contribute and reported below:

$$\begin{aligned}
&\frac{\partial \dot{e}_{|j}}{\partial e} = 0,\\
&\frac{\partial \dot{e}_{|j}}{\partial \psi_j} = n_1 C_{\mathrm{SRP}}\frac{\sqrt{1-e^2}}{na}\mathcal{T}_j \cos\psi_j + \frac{15}{8}a\frac{\sqrt{1-e^2}}{n}n_1 n_\odot e \mathcal{K}_j \cos 2\psi_j,\\
&\frac{\partial \dot{\psi}_j}{\partial e} = n_2\frac{\partial \dot{\Omega}_{(J_2,j,\odot)}}{\partial e} + n_1\frac{\partial \dot{\omega}_{(J_2,j,\odot)}}{\partial e},\\
&\frac{\partial \dot{\psi}_j}{\partial \psi_j} = 0.
\end{aligned} \tag{4.37}$$

where, the terms of the Hessian matrix of the commensurability equation are reported in Appendix B in Equation (B.4).

4.2.3. Dynamical structure of the resonance $j = 1$

In the following two sections dynamical structure analysis for the first resonance only, is reported. The coefficients of the quadratic equations for the other resonances are reported in Appendix D.

Under the hypothesis of dynamics driven by a single resonance, the resonant Hamiltonian corresponding to the first resonance is :

$$\begin{aligned}
\bar{\mathcal{H}}_1 = \frac{\mathcal{C}_{J_2}\mu^3(G^2-3H^2)}{4G^5L^3} + \\
-\frac{1}{4}\frac{\mathcal{C}_{\mathcal{SRP}}\sqrt{1-G^2/L^2}}{\mu}L^2(1+c_\varepsilon)(1+c_i)\cos(\omega+\Omega-\lambda_\odot) + \\
-\frac{15}{128}\frac{L^4 n_\odot^2}{\mu^2}e^2(1+c_\varepsilon)^2(1+c_i)^2\cos(2\omega+2\Omega-2\lambda_\odot) - n_\odot\sqrt{\mu a}\sqrt{1-e^2}
\end{aligned} \tag{4.38}$$

In the following, the bifurcation maps is drawn under the hypothesis of dynamics driven by J_2-Sun (AMR $= 0\ m^2/\mathrm{kg}$), SRP-J_2-Sun and SRP-J_2 (AMR $\geq \sigma^*_{i,j}$) models.

Dynamical structure at AMR $= 0\ m^2/\text{kg}$

If it is assumed that the spacecraft has negligible area, the dynamics can be described by the coupled Sun gravity and Earth oblateness model. The equilibrium points are at critical angles $\psi_{\odot,J_2} = 0, \frac{\pi}{2}, \pi, \frac{3\pi}{2}$, and π with corresponding eccentricity computed satisfying:

$$\dot{\psi}_{J_2,\odot_1} = \dot{\omega}_{J_2,\odot_1} + \dot{\Omega}_{J_2,\odot_1} - n_\odot = 0, \tag{4.39}$$

which can be conveniently reduced to a quadratic equation in the unknown $\cos i$ by elaborating Equation (4.25) with $\mathcal{C}_{SRP} = 0$:

$$(c_{1,J_2} + c_{1,\odot_1}) \cos i^2 + (c_{2,J_2} + c_{2,\odot_1}) \cos i + (c_{3,J_2} + c_{3,\odot_1}) = 0. \tag{4.40}$$

The coefficients are reported in Table 4.2 (note that the Equation (4.31) is multiplied by $4a^5\beta^5 en$ to have the same notation as in Alessi et al. [14]):

Table 4.2: Coefficients of the quadratic equation $c_1 \cos^2 i + c_2 \cos i + c_3 = 0$ associated to the extended model for $j = 1$ and AMR $= 0\ m^2/\text{kg}$. In the table, $\beta = \sqrt{1-e^2}$, $\gamma = \cos^2\left(\frac{\epsilon}{2}\right)$, $\rho = \sin^2\left(\frac{\epsilon}{2}\right)$.

	c_1	c_2	c_3
J_2	$15C_\oplus e\beta$	$-6C_\oplus e\beta$	$-e\beta\,(3C_\oplus + 4a^5\beta^4 n n_\odot)$
$\odot$	$+15/4a^5\gamma^2 e\beta^4 n_\odot^2 \cos 2\psi$	$+30/4a^5\gamma^2 e\beta^6 n_\odot^2 \cos 2\psi$	$-15/4a^5\gamma^2 e\beta^4(2e^2-1) n_\odot^2 \cos 2\psi$

The procedure followed to draw the bifurcation map (Figure 4.4), is reported in the flowchart Figure 4.2.
For each semi-major axis in the range under study, and for the resonance considered, the Equation (4.40) is solved for AMR $= 0\ m^2/\text{kg}$, $\psi = 0, \pi/2$ and π. As for example, the bifurcation diagram at $a = 16000$ km for the three angular configuration considered, the inclination range ($\tilde{\Pi}_0$) is in $[0, 180°]$ in Figure 4.3, has been reported in the plane (e, $\tilde{\Pi}_0$). Then, for each equilibrium point along the plot, if the eigenvalue product $\lambda_1\lambda_2$ according to Equation (4.36), results zero, the equilibrium point is a bifurcation.

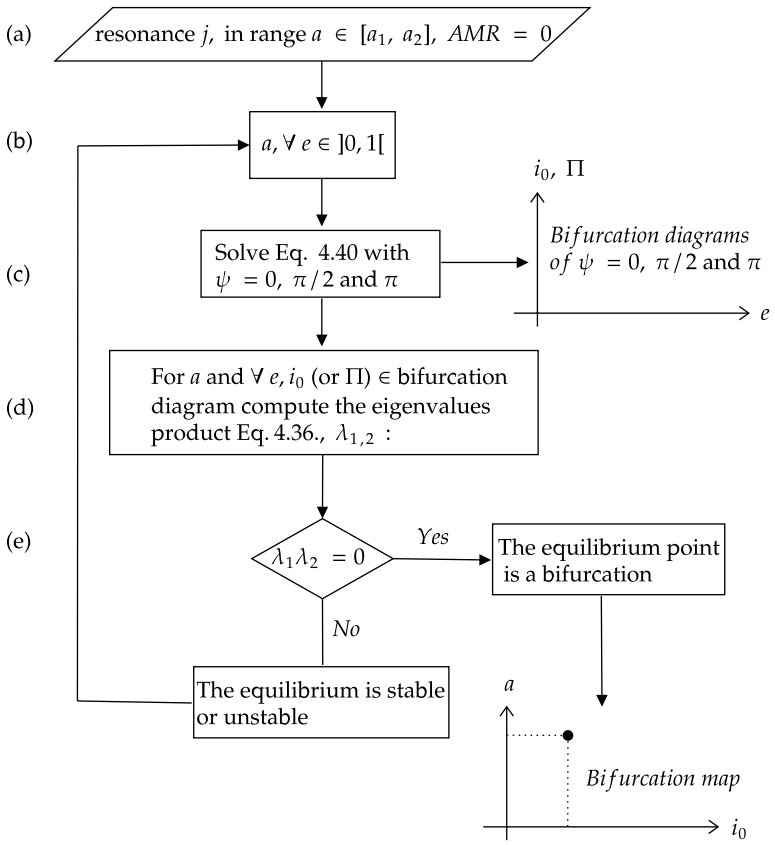

Figure 4.2: Flowchart of the procedure used to compute the bifurcation map (Figure 4.4) in the J_2-Sun coupled dynamics.

The populated bifurcation map of the dynamics is reported in Figure 4.4. In the figure, labelled with point (A) it has been reported reported the phase space characteristic of this region: it presents nine equilibrium points (three for each angular configuration). In region (B), instead, the dynamics presents only three equilibrium (one for each angle). The transition between (A) and (B) is reported in the bottom right phase spce of Figure 4.4, where the bifurcation for $a = 16000$ km occurs at $i_0 = 29.0085°$.
Table 4.3 summarises the number and behaviour of the equilibria appearing in Figure 4.4.

Table 4.3: Number of equilibria and their stability (S: stable, U: unstable) for the resonance with argument ψ_1, corresponding to the two regions of Figure 4.4

Region	Total	$\psi = 0$	$\psi = \pi/2$	$\psi = \pi$
(A)	9	2 U and 1S	1 U and 2 S	2 U and 1S
(B)	3	1 U	1 S	1 U

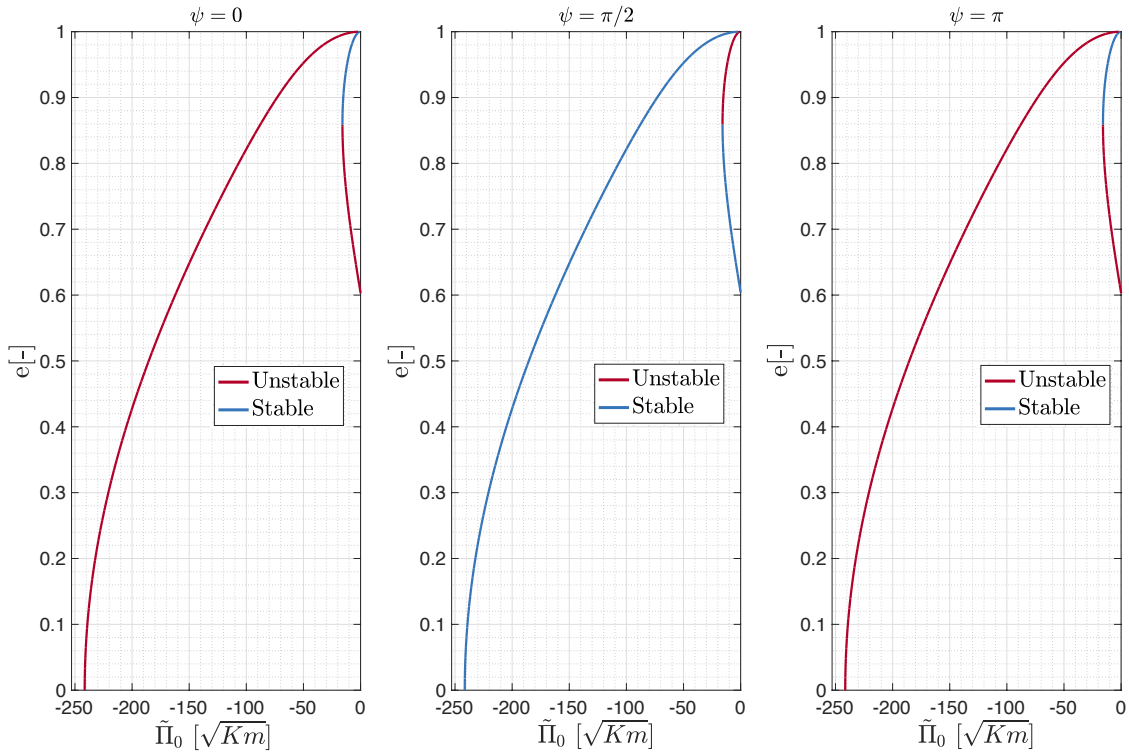

Figure 4.3: Bifurcation diagram for AMR $= 0$ m^2/kg, $a = 16000$ km and $j = 1$ for the $\odot, J_2$ model.

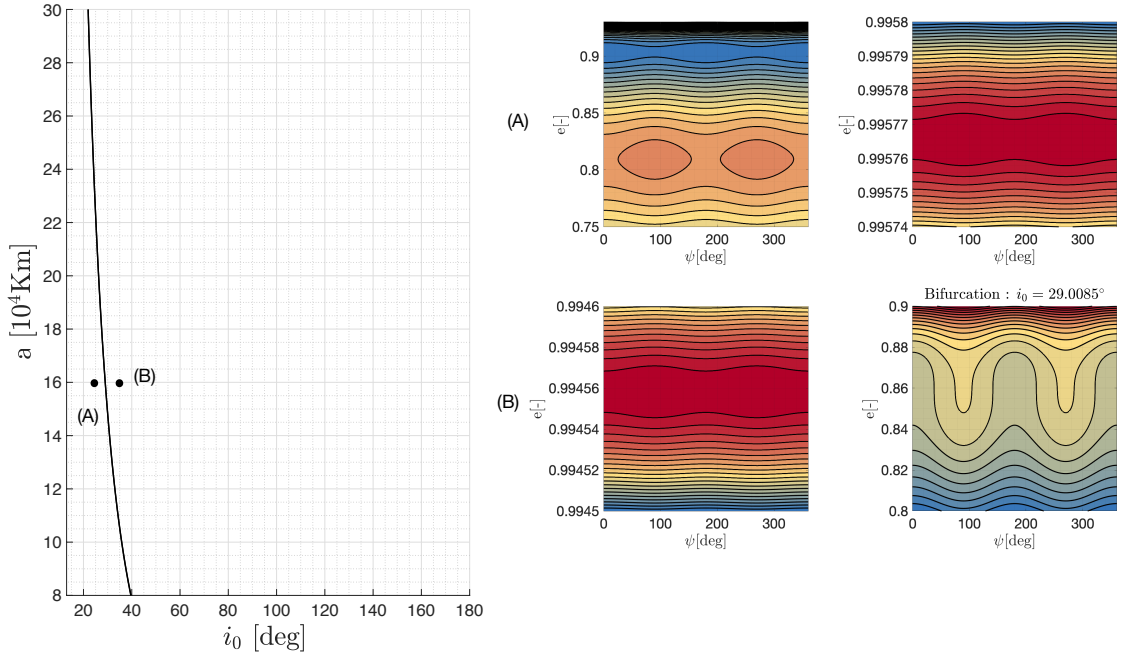

Figure 4.4: Bifurcation analysis plot for the $\odot, J_2$ model with i_0 from 0° to 180°, a from 8000 km to 30000 km and $j = 1$. Bifurcation at $i_0 = 29.0085°$ for $a = 16000$ km.

Dynamical structure at $0 <$ AMR $< \sigma^*_{i,j}$

For objects with low value of AMR the effect of the SRP on the orbital dynamics is not negligible. Under this hypothesis the dynamics is considered as driven by coupled SRP, Earth oblateness and Sun gravity perturbations. From Equation (4.29), the discriminant AMR for the first resonance is defined:

$$\sigma^*_{i,1} = \frac{5}{4}\frac{(1+c_\varepsilon)}{P_\odot c_R}(1+c_i)n_\odot^2 a e^{eq}_{i,j=1} \tag{4.41}$$

which drives the change of dynamical regime.

Figure 4.5, Figure 4.6 and Figure 4.7 display the equilibrium position (e, ψ) of the three asymmetric equilibrium points in $a = 10078$ km, $\tilde{\Pi}_0 = -17$ $[\sqrt{km^2}]$ ($i_0 = 33.8335°$), and varying the AMR ratio in the range $[0; 0.5]$ m^2/kg. It is possible to appreciate that, below $\sigma^*_{i,1}$, the eccentricity does not change as proven by Equation (4.33).

Note : the concept just studied is used to identify the bifurcation lines on the bifurcation map for the extended Hamiltonian model. In particular, if the AMR of the object under study, for a coordinate (a, i_0), is the same as that associated to the discriminant value $\sigma^*_{i,1}$, hence the equilibrium point is on a bifurcation.

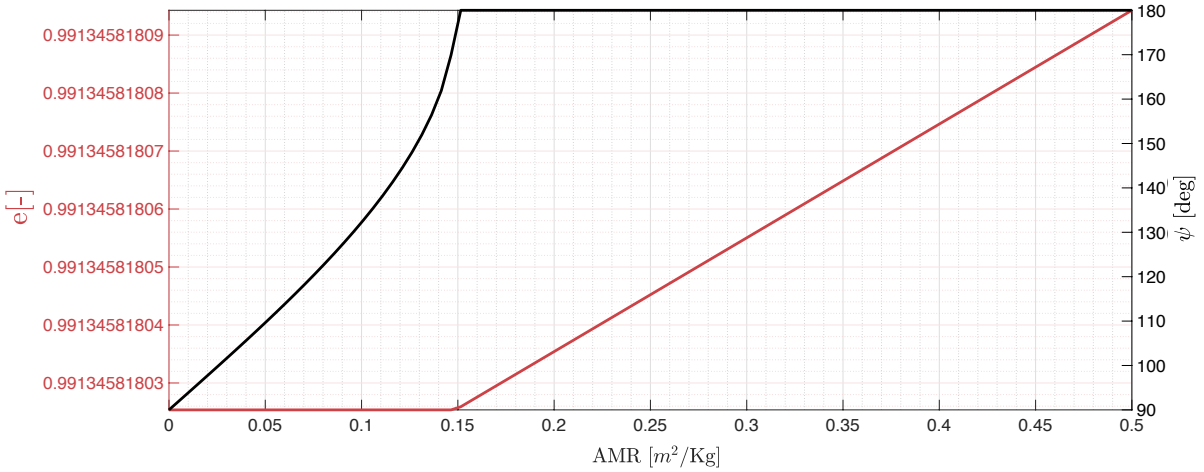

Figure 4.5: Position of the stable *asymmetric* equilibrium points of the extended model model at $a = 10078$ km, $\tilde{\Pi}_0 = -17.0\sqrt{km}$ with increasing values of AMR and $j = 1$.

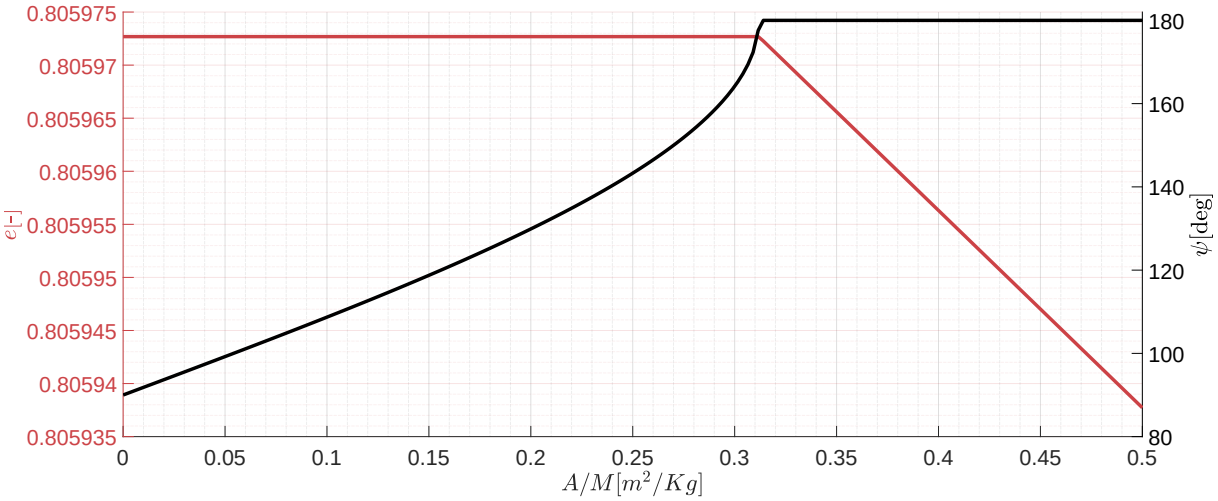

Figure 4.6: Position of the unstable *asymmetric* equilibrium points of the extended model model at $a = 10078$ km, $\tilde{\Pi}_0 = -17.0\ \sqrt{km}$ with increasing values of AMR and $j = 1$.

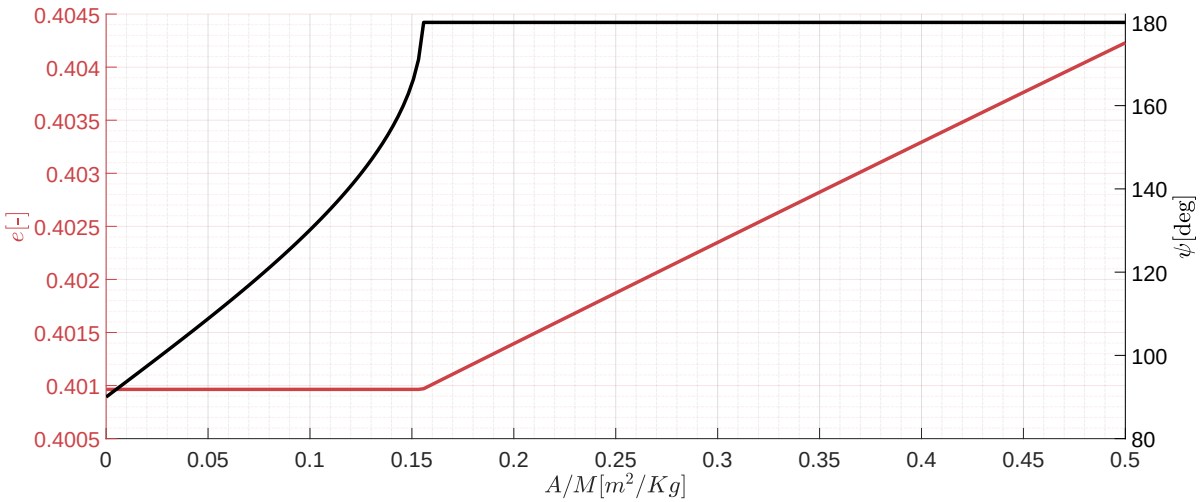

Figure 4.7: Position of the stable *asymmetric* equilibrium points of the extended model model at $a = 10078$ km, $\tilde{\Pi}_0 = -17.0\ \sqrt{km}$ with increasing values of AMR and $j = 1$.

Regarding the equilibrium points at $\psi = 0, \pi$ their equilibrium eccentricity can be easily computed by verifying the commensurability equation:

$$\begin{aligned}(c_{1,J_2} + c_{1,\odot_1} + c_{1,\mathrm{SRP}_1})\cos i_0{}^2 + (c_{2,J_2} + c_{2,\odot_1} + c_{2,\mathrm{SRP}_1})\cos i_0 + \\ +(c_{3,J_2} + c_{3,\odot_1} + c_{3,\mathrm{SRP}_1}) = 0.\end{aligned} \tag{4.42}$$

The coefficients c_i are reported in Table 4.4.

Table 4.4: Coefficients of the quadratic equation $c_1 \cos^2 i + c_2 \cos i + c_3 = 0$ associated to the extended model for $j = 1$. In the table, $\beta = \sqrt{1-e^2}$, $\gamma = \cos^2\left(\frac{\epsilon}{2}\right)$, $\rho = \sin^2\left(\frac{\epsilon}{2}\right)$. Note that Equation (4.40) is multiplied by $16a^5\beta^5 en$.

Effect	c_1	c_2	c_3
J_2	$60C_\oplus e\beta$	$-24C_\oplus e\beta$	$-4e\beta\,(3C_\oplus + 4a^5\beta^4 n n_\odot)$
SRP		$+8C_{\text{SRP}}a^4\beta^4\gamma\cos\psi$	$+8C_{\text{SRP}}a^4\beta^4\gamma(1-2e^2)\cos\psi$
$\odot$	$+15a^5\gamma^2 e\beta^4 n_\odot^2\cos 2\psi$	$+30a^5\gamma^2 e\beta^6 n_\odot^2\cos 2\psi$	$-15a^5\gamma^2 e\beta^4(2e^2-1)n_\odot^2\cos 2\psi$

Bifurcation map generation algorithm

The algorithm used to compute the bifurcation maps presented in Figure 4.12, Figure 4.11, Figure 4.13 and Figure 4.14 is reported in Figure 4.8 for an easier understanding of the procedure.

In addition to the bifurcation diagram presented in Chapter 3 (in Figure 3.5), bifurcations connected to the points $\psi = 0, \pi$ are added those associated to the asymmetric points. In fact, for the first, the procedure to obtain their position is the same as in Figure 3.1, but rather than using the Equation (3.26), it uses Equation (4.42) and the coefficients are reported in Table 4.4.

Regarding the asymmetric points, the technique is rather more laborious. First of all, for each semi-major axis in the range under study and for $e \in]0, 1[$ the position of the equilibrium points of the Sun-J_2 model with the equation Equation (4.42) is computed. As already remarked before, a bifurcation occurs when for the triplet (a, i_0, AMR) the asymmetric point has $\cos\psi_{asym} = -1$ (see Equation (4.28)), that is to say $\psi_{asym} \to \pi$. The bifurcation takes place when, for the coordinate (a, i_0) and for the eccentricity of the asymmetric equilibrium point just computed, satisfies the condition :

$$\sigma^*_{i,j} = \text{AMR}. \tag{4.43}$$

To better summarise, let us refer to the plot in Figure 4.7: for (a, i_0) indicated, the angular position of the equilibrium point, continuously increase from $\psi = \pi/2$ until reach $\psi = \pi$ when AMR $= \sigma^*_{1,1}$. Conversely, the eccentricity remains constant until the bifurcation condition is reached. In conclusion, for the couple (a, i_0) reported in the plot, if the AMR of the orbiting object is the same of the discriminant AMR, that point populates the bifurcation diagram. The delineate procedure has to be repeated for each asymmetric

equilibrium point reported in Table 4.3.

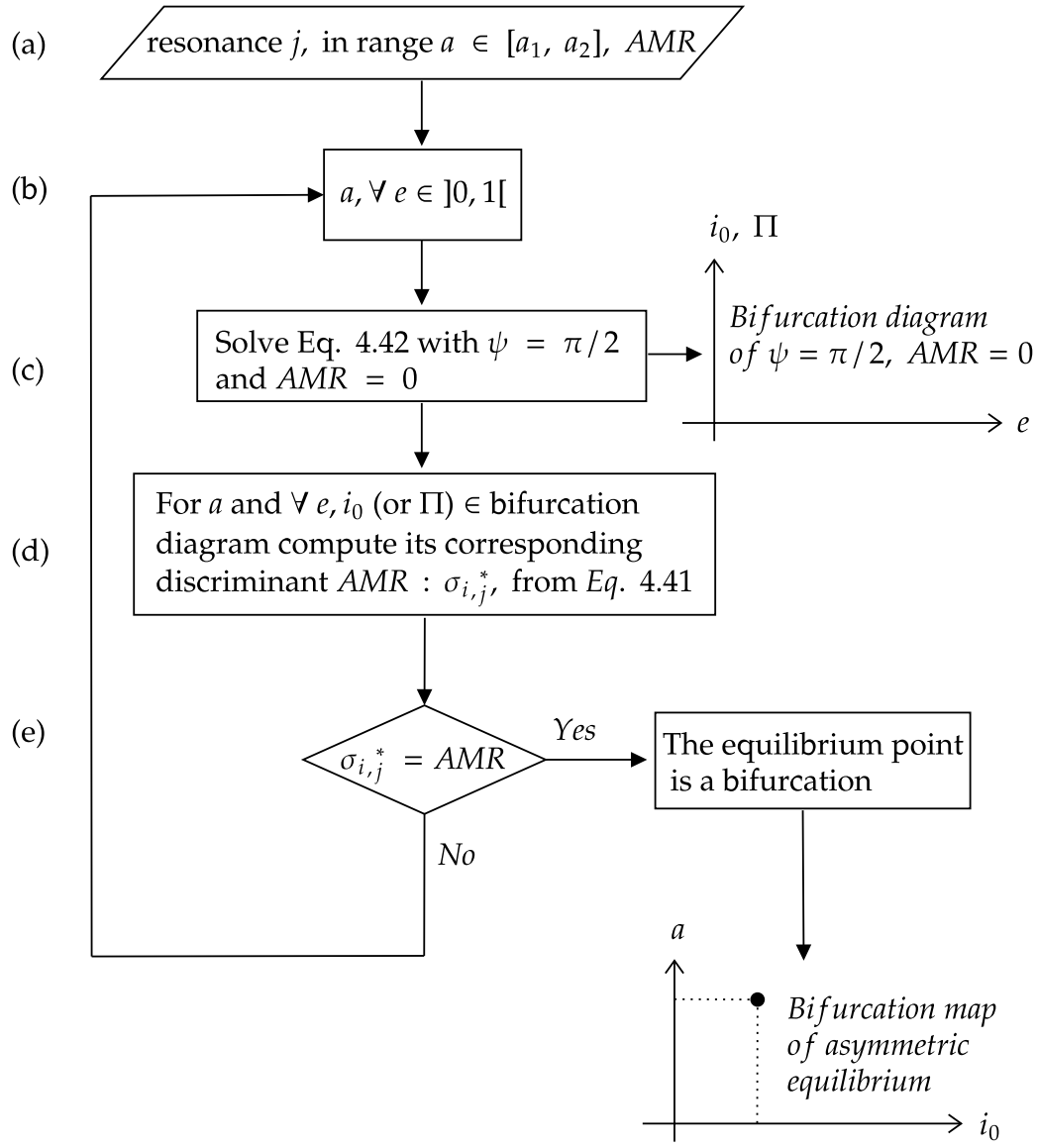

Figure 4.8: Flowchart of the algorithm used to identify the bifurcation points associated to the asymmetric equilbria.

Figure 4.9 shows the position of the bifurcation lines as function AMR. Specifically, when AMR rises, the bifurcations shift to higher altitudes and lower inclination, indicating that the influence of the third-body disturbance is more significant at higher altitudes. In the following sections, are shown two examples of bifurcation maps for two different AMR.

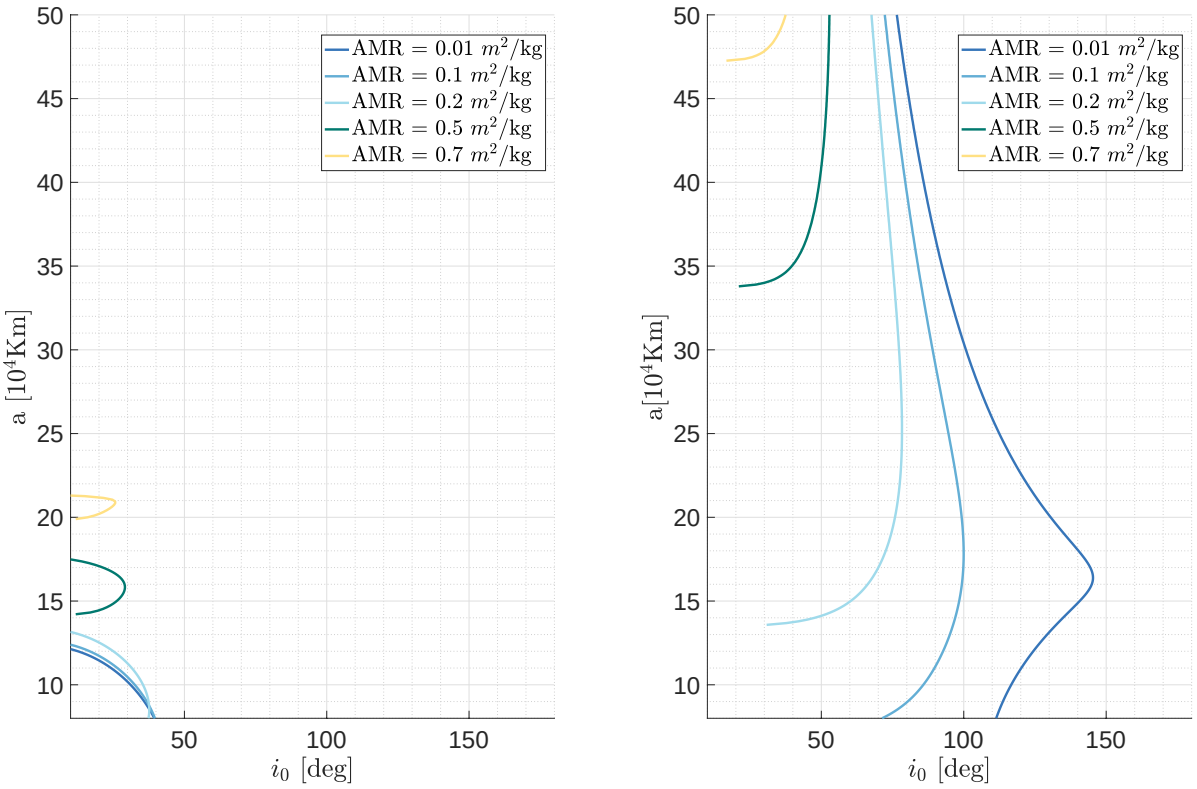

Figure 4.9: Bifurcation map of the resonant term ψ_1 with AMR $= 0.5\ m^2$/kg. On the bottom are reported the peculiar phase space appearing in the five identified regions.

Case study : AMR $= 0.3\ m^2$/kg

With reference to Figure 4.12, Figure 4.11, and Figure 4.13, the dynamical behaviour in the regions identified by the newly derived bifurcations is described. The yellow bold lines are generated from the bifurcation condition on the two equilibrium points along the first solution of Equation (4.42), while the green bold one to the equilibrium present along the second solution of Equation (4.42) (see Figure 4.3 for comparison). The characteristics of the equilibrium points in the region (II)(Figure 4.11), are listed in Table 4.5:

Table 4.5: Equilibrium points in region (II) of Figure 4.11 for AMR $= 0.3\ m^2$/kg.

Region	$\psi = 0$	$\psi = \pi$	Asymmetric	Total
A	2 S and 2 U	2 U and 1 S	1 S in (A,2), 1 S in (A,4) and 1 U in (A,3)	10
B	2 S and 2 U	1 U and 2 S	1 S in (A,2) and 1 U in (A,3)	9
C	2 S and 2 U	3 S	1 U in (A,3)	8

The characteristics of the equilibrium points in the region (I)(Figure 4.12), are listed in

Table 4.6:

Table 4.6: Equilibrium points in region (I) of Figure 4.12 for AMR = 0.3 m^2/kg.

Region	$\psi = 0$	$\psi = \pi$	Asymmetric	Total
A	1 S and 1 U	3 S	1 U in (A,2)	6
B	1 S and 1 U	2 S and 1 U	-	5

The characteristics of the equilibrium points in the region (III)(Figure 4.13), are listed in Table 4.7:

Table 4.7: Equilibrium points in region (III) of Figure 4.13 for AMR = 0.3 m^2/kg.

Region	$\psi = 0$	$\psi = \pi$	Asymmetric	Total
A	1 S and 1 S	1 S in (A,2)	4	
B	1 S and 1 U	2 S	-	3

For the regions (IV), (V), (VI) and (VII), since they are all above the bifurcations, their dynamics is the same as the one presented in Chapter 3 and completely described by Table 3.4.

Case study: AMR = 0.5 m^2/kg

Figure 4.14, shows the bifurcation diagram relative to AMR = 0.5 m^2/kg. Here, the third bifurcation line (the green one), is not visible, since it is locate at higher altitudes. In the region (II), the characteristics of the equilibrium points are listed in Table 4.8:

Table 4.8: Characteristics of asymmetric bifurcation

Region	$\psi = 0$	$\psi = \pi$	Asymmetric	Total
A	2 S and 2 U	2 U and 1 S	1 S in (A,2) and 1 U in (A,3)	9
B	2 S and 2 U	3 S	1 U in (A,3)	8
C	2 S and 2 U	2 S and 1 U	-	7

To summarise, although the position of the bifurcations depends on AMR, the number of asymmetric points and their stability behaviour holds the same as represented in Fig-

ure 4.10. In fact, above each bifurcation branch, an asymmetric equilibrium is added. In particular, as reported in Table 4.9 and in reference to Figure 4.10:

Table 4.9: Characteristics of asymmetric bifurcation

Bifurcation branch	Equilibrium added
First Y	1 U
Second Y	1U and 1 S
First G (region I)	2 S and 1 U
First G (region II)	1 S

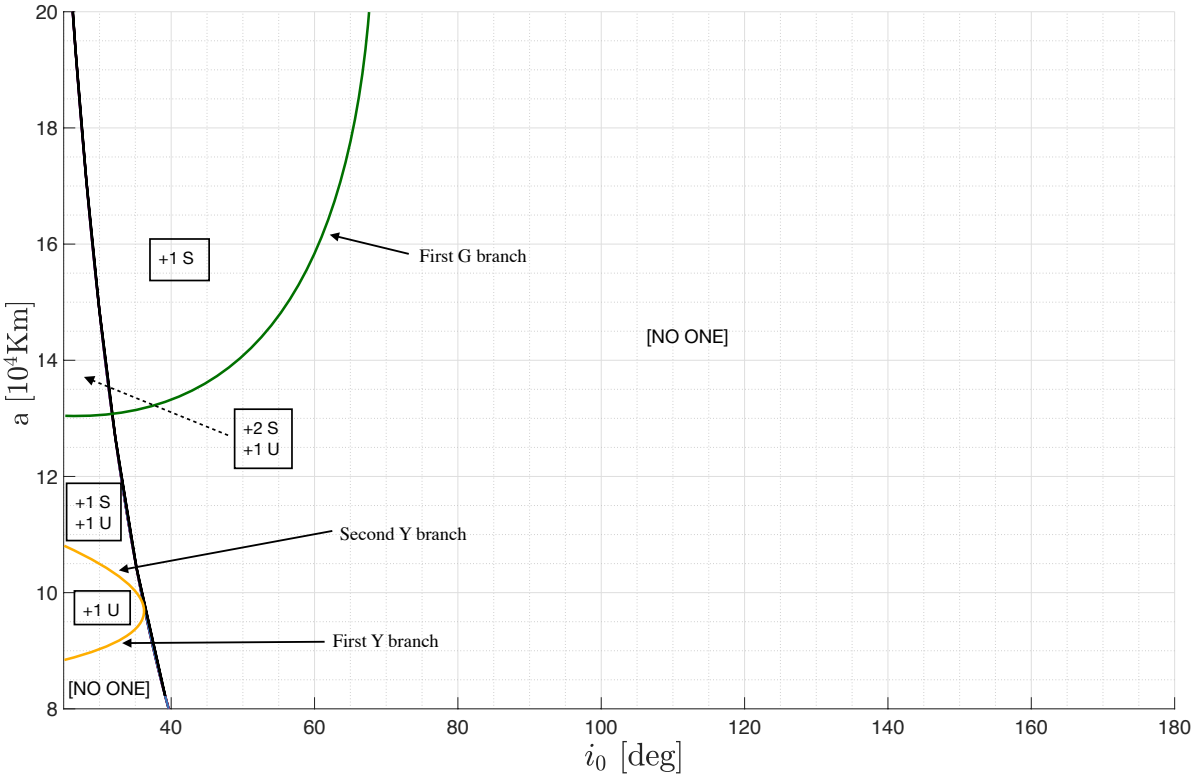

Figure 4.10: Number of asymmetric equilibrium points with their stability added by region identified by the bifurcation lines.

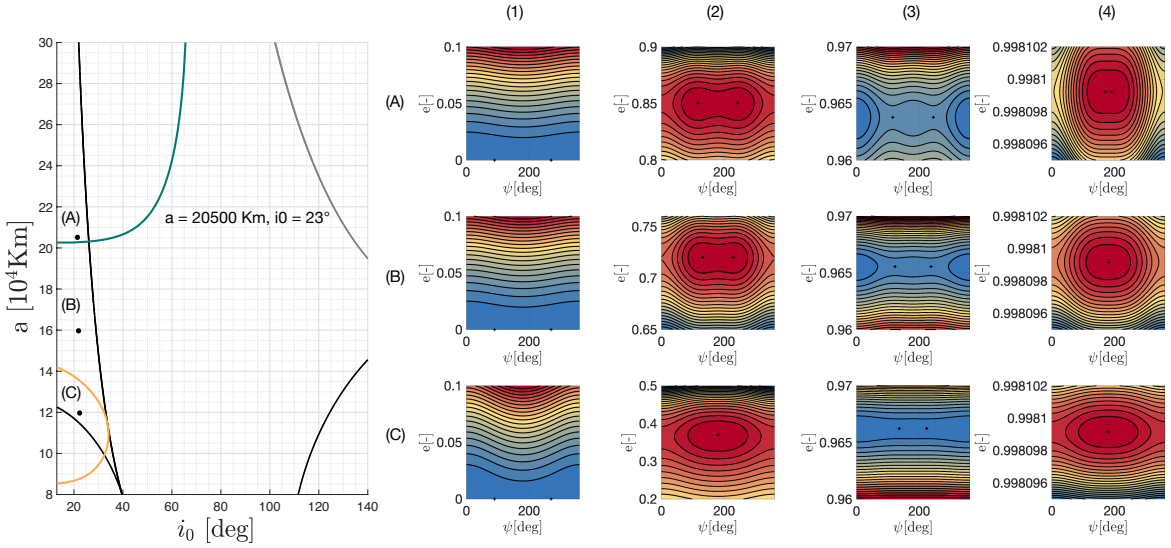

Figure 4.11: Bifurcation map of the resonant term ψ_1 with AMR $= 0.3\ m^2/\text{kg}$. On the bottom are reported the peculiar phase space appearing in the region (II).

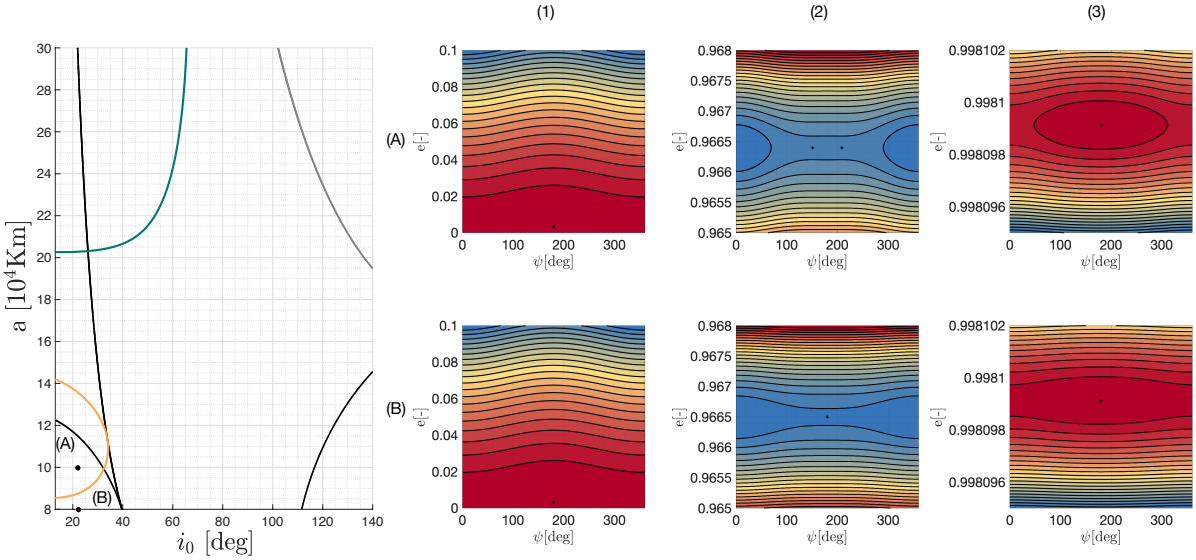

Figure 4.12: Bifurcation map of the resonant term ψ_1 with AMR $= 0.3\ m^2/\text{kg}$. On the bottom are reported the peculiar phase space appearing in the region (I).

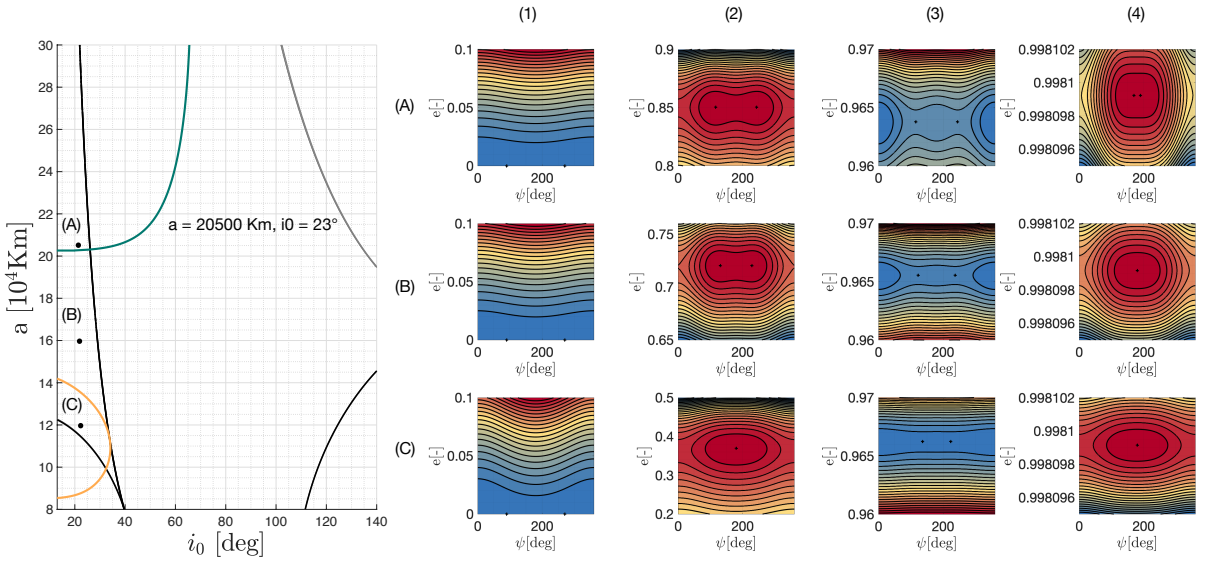

Figure 4.13: Bifurcation map of the resonant term ψ_1 with AMR $= 0.3\ m^2/\text{kg}$. On the bottom are reported the peculiar phase space appearing in the region (III).

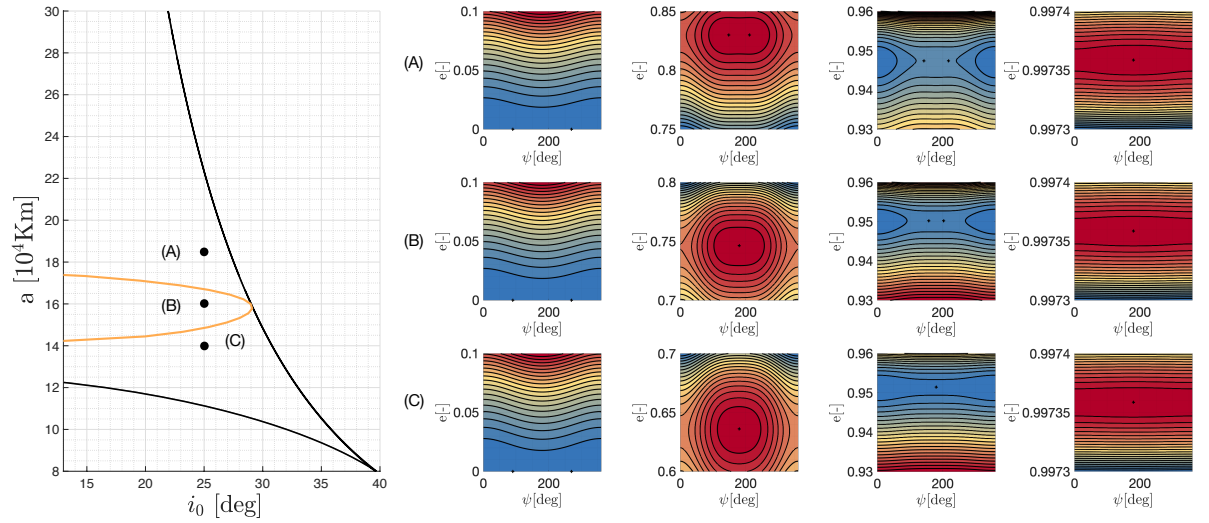

Figure 4.14: Bifurcation map of the resonant term ψ_1 with AMR $= 0.5\ m^2/\text{kg}$. On the bottom are reported the peculiar phase space appearing in the region (II).

Note on the trans-critical bifurcation

The so called trans-critical bifurcation limits the (IV) area. It is important to note that, if the discriminant AMR is exceeded in this area, the stable asymmetric points do not collapse to $\psi = \pi$, but rather to $\psi = 0$, since they must adhere to the stability behavior of the SRP-J_2 dynamics that is specific to that region. This phenomena is reported in Figure 4.15 for increasing AMR. The phase spaces (A) correspond to a point in the area (IV), while the phase spaces (B) relate to the region (III) (and to the other regions):

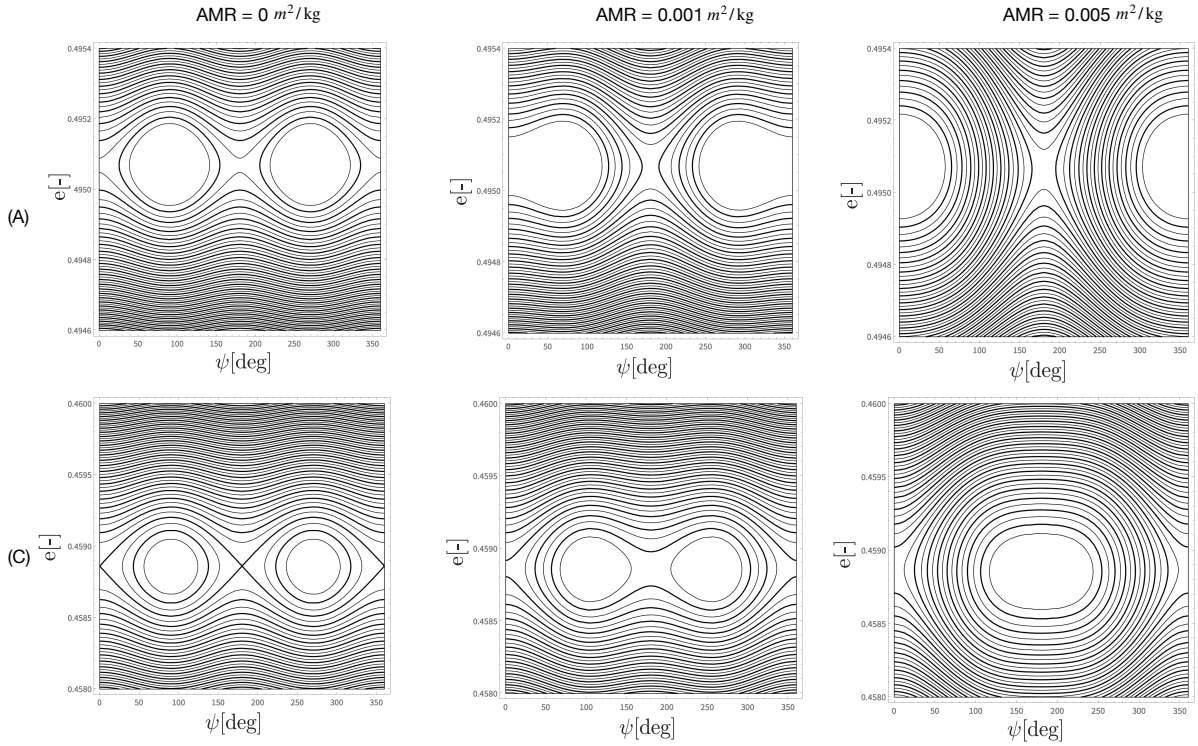

Figure 4.15: Up : asymmetric points collapsing in $\psi = 0$ in region (IV) and, down : asymmetric points collapsing in $\psi = \pi$ in region (III)(and to the other regions).

Dynamical structure at AMR $\geq \sigma^*_{i,j}$

If for a given initial condition (a, $i_{e=0}$, $e^{eq}_{i,j=1}$):

$$\text{AMR} \geq \sigma^*_{i,1} = \frac{5}{4}\frac{(1+c_\varepsilon)}{P_\odot c_R}(1+c_i)n_\odot^2 a e^{eq}_{i,j=1} \tag{4.44}$$

with $\cos i$ computed from the conservation of the second integral of motion $\Pi_{e=0}$:

$$\sqrt{1-e^2}(n_2 - n_1\cos i) = (n_2 - n_1 \cos i_{e=0}), \tag{4.45}$$

the dynamics can be completely described by the SRP-J_2 model. Hence, the bifurcation map resembles the one calculated in Figure 3.5. This is due to the fact that, as seen in Figure 4.9, the asymmetric bifurcations move upwards with rising AMR.
In the next section, it has been proven that, the harmonic contribute of the Sun gravity on the time variation of the eccentricity and inclination becomes negligible when the discriminant AMR is exceeded.

Final Remark

In previous analysis, the conditions under which the asymmetric points fall into a bifurcation on the phase space of the extended Hamiltonian model are derived. These additional points are added to the existing one, which forms the foundation of the studied map (a, i_0, AMR).
Considering the other resonances, the coefficients of Equation (4.34) are reported in Appendix D for completeness. The procedure has been outlined so that future researchers may continue with the study.

4.2.4. Validation of the Hamiltonian model

In this section the just derived model is validated against the semi-analytical propagator. As done for the semi-analytical propagator described in Chapter 2 and detailed in Appendix A, a semi-analytical propagator is modelled using as perturbing function the single-resonance Hamiltonian Equation (4.38) such that :

$$\bar{\mathcal{R}} = -\bar{\mathcal{H}}_j \tag{4.46}$$

Although the Hamiltonian is autonomous, its integration requires the position of the Sun, hence the only time dependent quantity is the ecliptic longitude of the Sun $\lambda_\odot(t)$, that here is assumed having a circular orbit lying on the ecliptic plane :

$$\lambda_\odot(t) = \lambda_{\odot,0} + n_\odot t \tag{4.47}$$

In Figure 4.16, Figure 4.17 and Figure 4.18 has been reported the time evolution for 90 years of the eccentricity and of the inclination computed with the full-dynamics semi-analytical (red line) and Hamiltonian (blu line) propagators. The initial conditions at 01/01/2001 00:01 UTC are reported in Table 4.10.
In Figure 4.19, Figure 4.20 and Figure 4.21, the phase space (e, ψ) obtained by integrating the equation of motion in the framework of dynamics driven by a single-resonance

Hamiltonian (light gray) and by the complete semi-analytical dynamics (colored lines) are compared, with initial conditions reported in Table 4.10, respectively.

Table 4.10: Initial Keplerian elements of the test cases.

Test	a km	e	$i_{e=0}$ rad	Ω rad	ω rad	f rad	AMR m^2/kg
Figure 4.16	12000	0.29	0.3491	0	0	0	0.01
Figure 4.17	12000	0.29	0.3491	0	0	0	0.1
Figure 4.18	12000	0.29	0.3491	0	0	0	≈ 0.15
Figure 4.19	12078	0.445	0.3491	0	$0, \pi/2, \pi$	0	0.01
Figure 4.19	12078	0.445	0.3491	0	$0, \pi/2, \pi$	0	0.05
Figure 4.19	12078	0.445	0.3491	0	$0, \pi/2, \pi$	0	0.5

The applicability of this model, as stated in the initial hypothesis, is near the resonance (Casanova et al. [29]). On the other hand, far from it, the coupled effect of the higher order harmonics and the combined Luni-solar perturbation deviate the dynamics from the one represented by the Hamiltonian semi-analytical propagator.
As can be seen, the propagated trajectory deviates from the Hamiltonian model due to the contribution of extra harmonics and higher order terms that are not accounted for in the Hamiltonian formulation. In addition, the extended model does not include the contribution of the Moon's gravity, as its Hamiltonian formulation lacks the same critical argument as that of the Sun and SRP. As a result, it is not possible write the Hamiltonian with respect to a rotating reference frame containing the Sun-Earth line, and it is therefore impossible to reduce the single-averaged formulation to autonomy. This may be conceivable if a procedure with a higher level of averaging (i.e. double averaging) is used and the Moon's impact on node precession, inclination, and argument of perigee fluctuation is ignored. Nevertheless, the double-averaged Hamiltonian (first about mean anomaly and second about the Sun mean anomaly) renders the SRP contribution null (see Gkolias et al. [15] and Gkolias et al.[43]). Nonetheless, the Hamiltonian model is able to retrieve valuable information on the dynamics in a quasi-analytical formulation, thereby simplifying the preliminary analysis of disposal manoeuvre design.
Regarding the computational time, the integration of the equation of motion based on the Hamiltonian formulation requires less time than the one required by the integration of the semi-analytical propagator. In Table 4.11 are reported the computational times of the integration of the Hamiltonian and the semi-analytical model of the initial conditions of Figure 4.16, Figure 4.16 and Figure 4.18 and AMR = 2 m^2/kg run on a 2.3 GHz 8-Core

Intel Core i9 CPU. It is possible to see that the CPU time required for the integration of the Hamiltonian model is approximately a sixth of the one required by the second model, and, moreover, the computational times do not depend on AMR.

Table 4.11: Computational time comparison on 2.3 GHz 8-Core Intel Core i9 CPU

Test	t_{CPU} (Hamiltonian) s	t_{CPU} (Semi-analytical) s
Figure 4.16	0.233415	1.479738
Figure 4.17	0.231110	1.480736
Figure 4.18	0.234676	1.624767
AMR = 2 m^2/kg	0.281956	1.652886

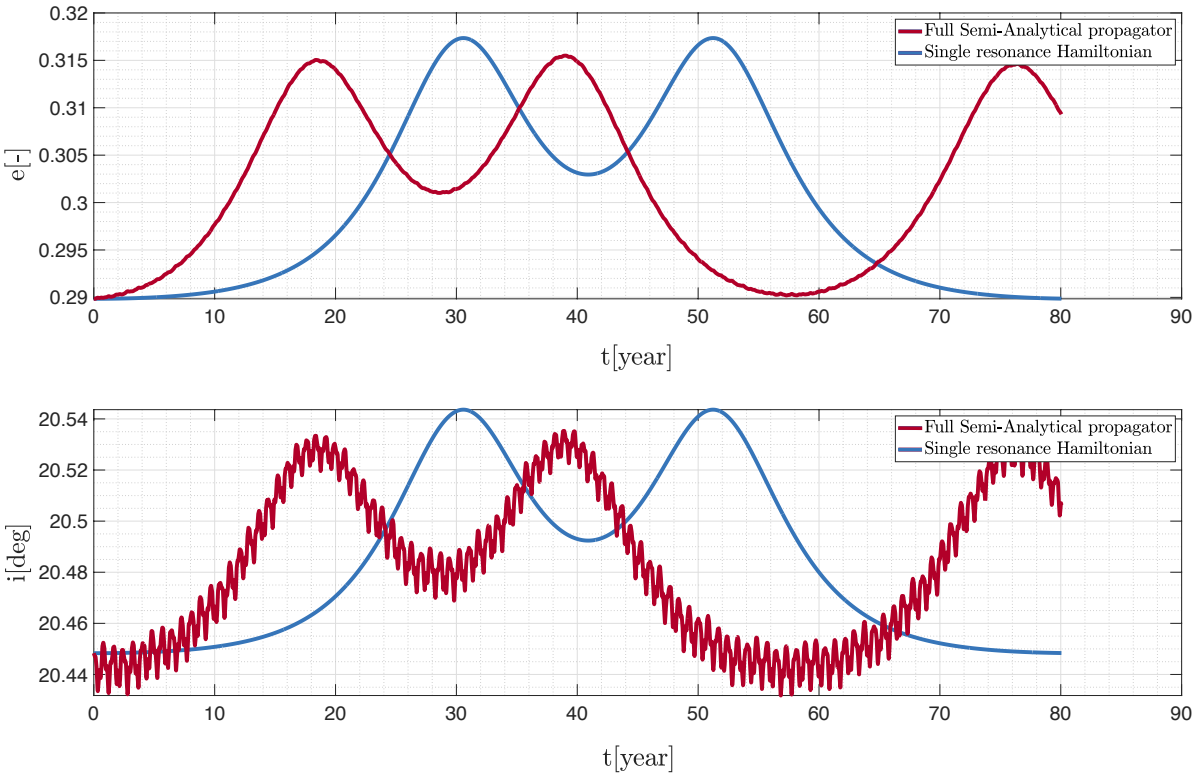

Figure 4.16: time evolution of the eccentricity and inclination propagated with the full-dynamics and with the single-resonant Hamiltonian propagators. AMR = 0.01 m^2/kg, $a = 12000$ km and $i_{e=0} = 20°$.

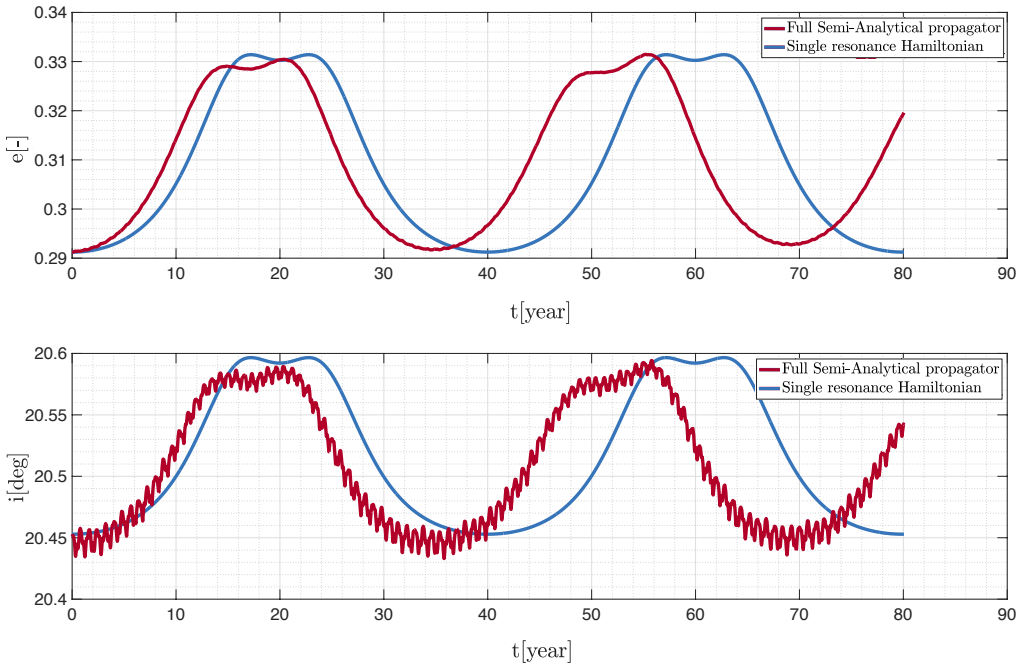

Figure 4.17: time evolution of the eccentricity and inclination propagated with the full-dynamics and with the single-resonant Hamiltonian propagators. AMR = 0.1 m^2/kg, $a = 12000$ km and $i_{e=0} = 20.0°$.

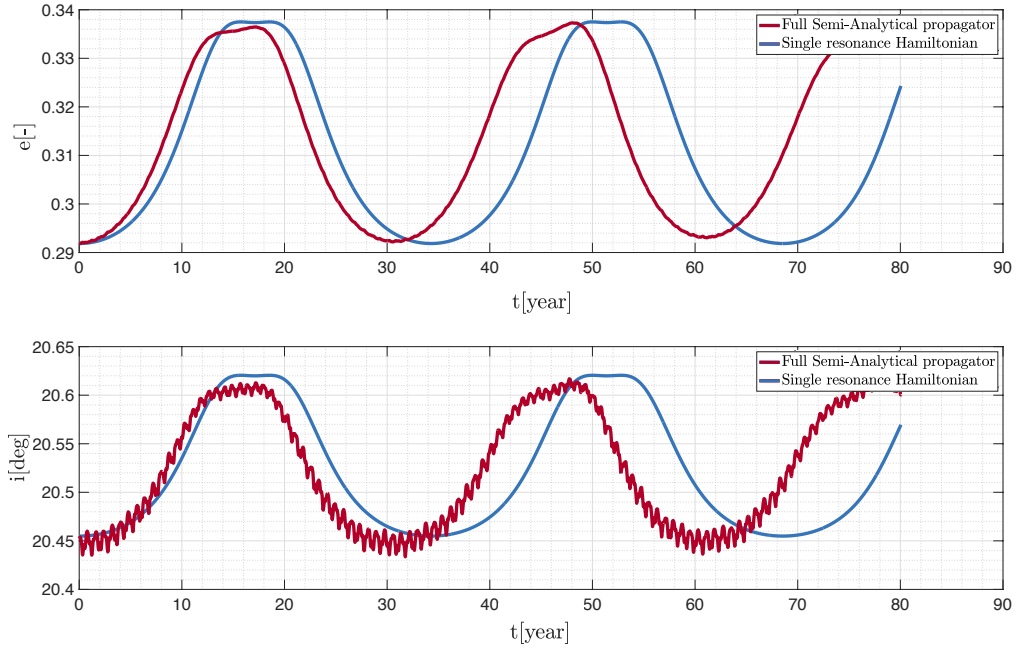

Figure 4.18: time evolution of the eccentricity and inclination propagated with the full-dynamics and with the single-resonant Hamiltonian propagators. AMR = $\sigma^*_{1,1} \approx 0.15$ m^2/kg, $a = 12000$ km and $i_{e=0} = 20.0°$.

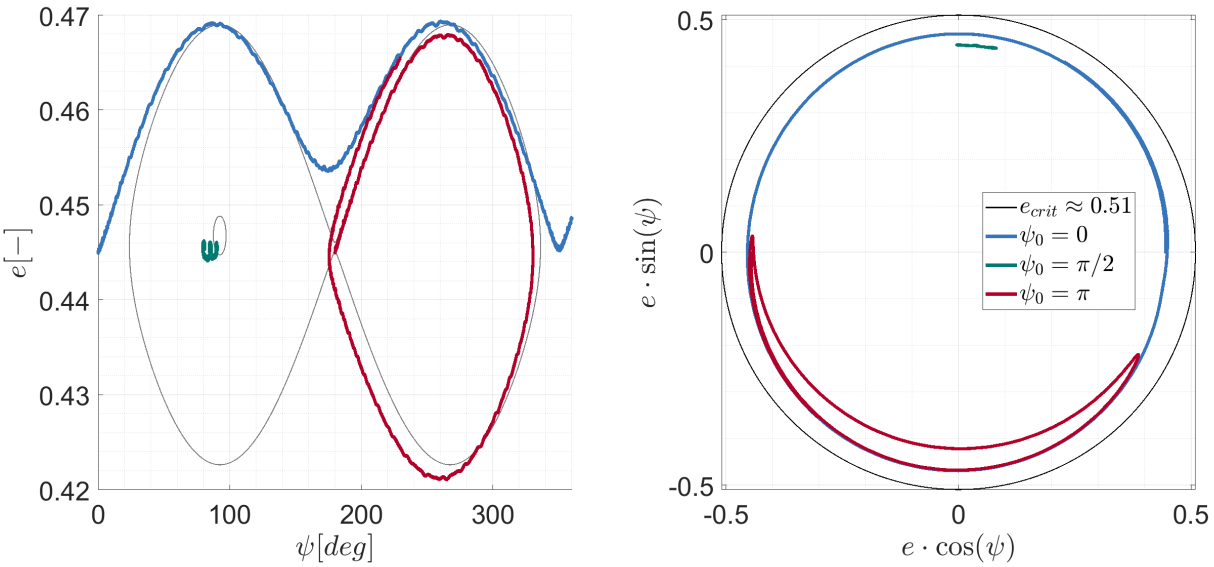

Figure 4.19: Representation in the plane (e, ψ) and in the Poincare plane ($e\cos\psi, e\sin\psi$) of the trajectories propagated with the Hamiltonian propagator (light gray) and semi-analytical propagator (coloured lines) for AMR = 0.01 m^2/kg, a = 12078 km and $i_{e=0}$ = 25.5°

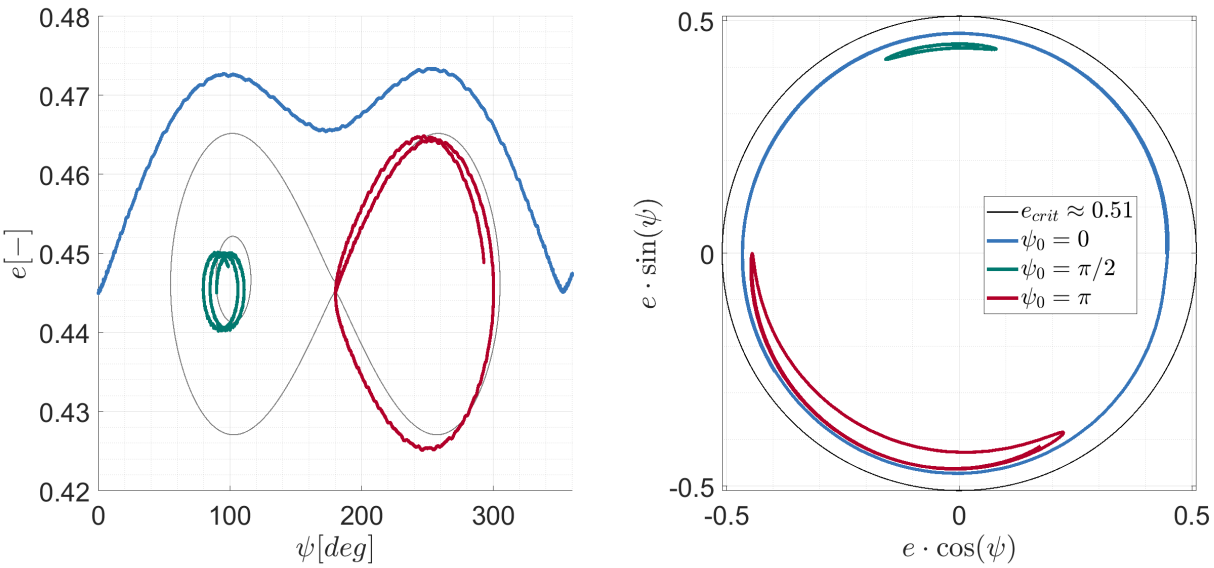

Figure 4.20: Representation in the plane (e, ψ) and in the Poincare plane ($e\cos\psi, e\sin\psi$) of the trajectories propagated with the Hamiltonian propagator (light gray) and semi-analytical propagator (coloured lines) for AMR = 0.05 m^2/kg, a = 12078 km and $i_{e=0}$ = 25.5°.

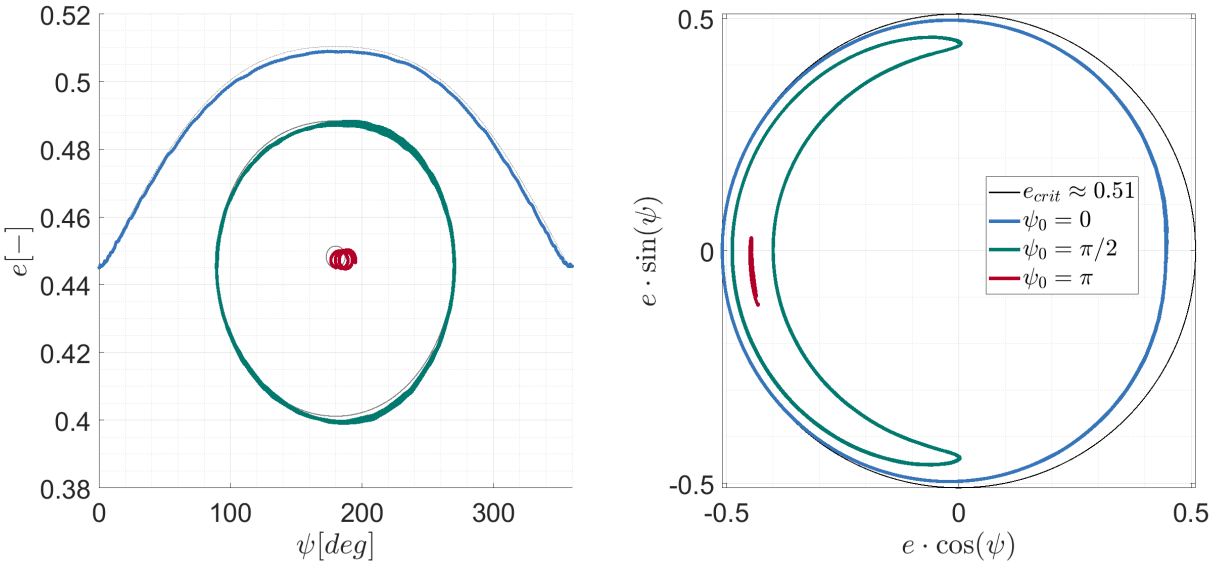

Figure 4.21: Representation in the plane (e, ψ) and in the Poincare plane ($e\cos\psi, e\sin\psi$) of the trajectories propagated with the Hamiltonian propagator (light gray) and semi-analytical propagator (coloured lines) for AMR = 0.5 m^2/kg, a = 12078 km and $i_{e=0}$ = 25.5°.

4.2.5. Effect of the discriminant AMR ($\sigma^*_{i,j}$) on the orbital dynamics

When, for a specific equilibrium point, its associated discriminant AMR is exceeded, the asymmetric equilibrium points collapse to π if the initial condition is below the trans-critical bifurcation (see Figure 4.15), and to 0 if are above the line. Figure 4.22 shows the width of the asymmetric resonance for an object having initial condition a = 12000 km, $i_{e=0}$ = 20°. The width δe has been computed solving the Equation (4.27) in the cases of $\psi = \pi$ and asymmetric point, then computing the distance between the correspondent eccentricities. It is possible to note that the width of the resonance is zero for AMR$\geq \sigma^*_{1,1} \approx 0.15\ m^2$/kg.

From a dynamical standpoint, this indicates that the oscillation induced by the harmonic of the Sun in the eccentricity depends on the initial argument of ψ: in Figure 4.23, the evolution of eccentricity and inclination for different AMR is reported; it is possible to see that if the initial point is located on the unstable point in $\psi = 0$, the oscillation with higher frequency of the Sun gravity decreases (also shown by Wang et al. [96]) with the increase of AMR, and from about the value of $\sigma^*_{i,j} \approx 0.15\ m^2$/kg they completely disappear (see also Figure 4.22). Similarly, in Figure 4.24, if the initial condition is the unstable point at $\psi = \pi$, for increasing AMR, the overall evolution of inclination and

eccentricity stabilise at constant value because the unstable point changes into a stable point.

Due to the presence of higher order perturbations and multi-resonance interactions, this is not exactly true in practice.

As final remark, it is possible to see that, when the discriminant AMR is exceeded, the Hamiltonian of the SRP overwhelms the Hamiltonian of the Sun gravity (see Equation (4.1)):

$$\left| \frac{\mathcal{H}_{\odot j}}{\mathcal{H}_{SRPj}} \right| << 1, \tag{4.48}$$

In fact, by substituting the definition of $\sigma^*_{i,j}$ in Equation (4.1) (evaluated at $\psi = \pi$ or $\psi = 0$, for any resonance):

$$\left| \frac{\mathcal{H}_{\odot j}}{\mathcal{H}_{SRPj}} \right| = \frac{5}{16} \frac{a n_\odot^2 e_{i,j}^{eq}}{P_\odot c_R \sigma^*_{i,j}} \frac{\mathcal{K}_j}{\mathcal{T}_j} = \frac{1}{4}. \tag{4.49}$$

In conclusion, for AMR $\geq \sigma^*_{i,j}$, whatever are the resonance, semimajor-axis, and inclination considered, the contribute of SRP is four times higher than the contribute of the Sun gravity. As consequence, it is reasonable to consider that the orbital dynamics is subject to the coupled SRP-J_2 model only.

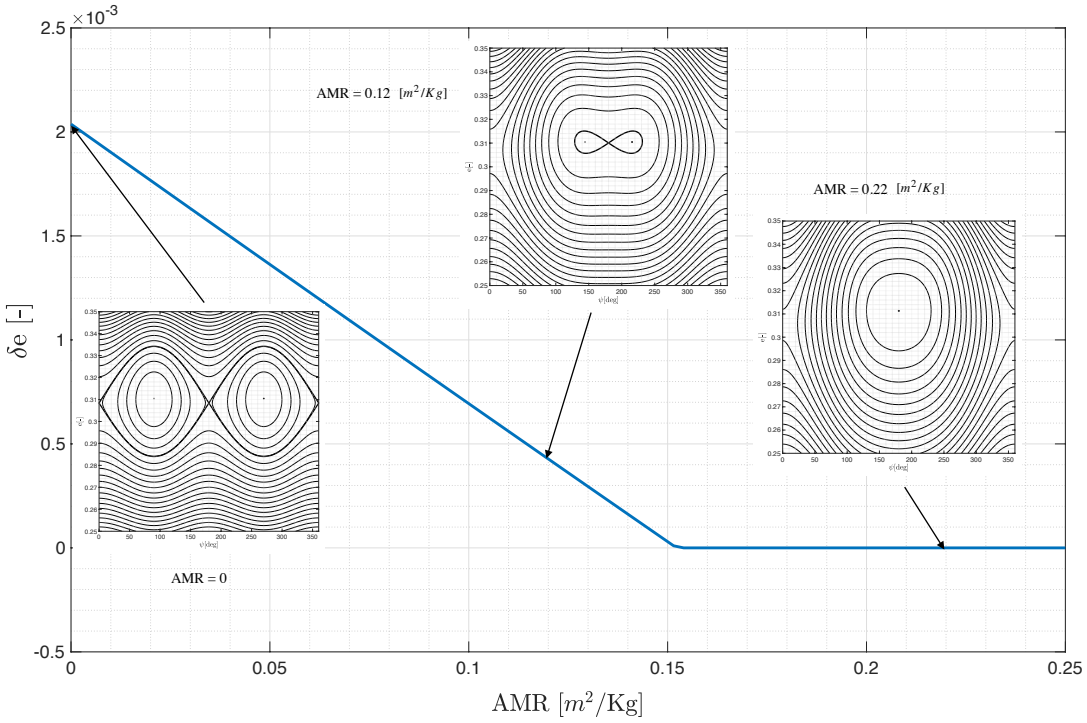

Figure 4.22: Asymmetric resonance width as function of the AMR at $a = 12000$ km, $i_0 = 20°$

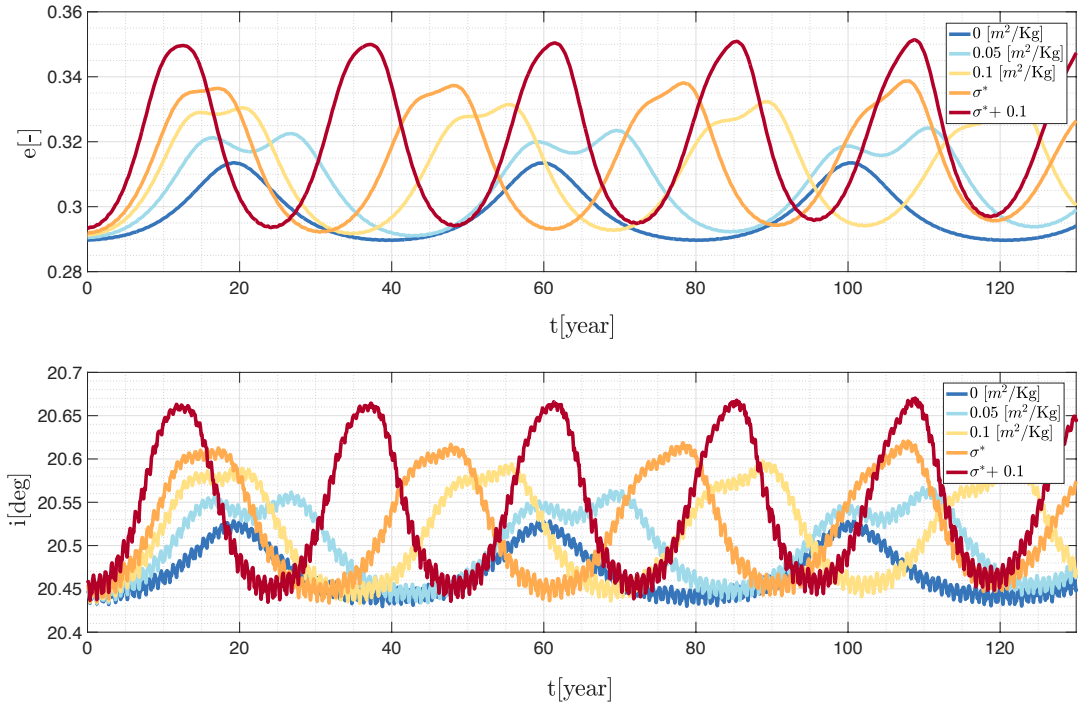

Figure 4.23: time evolution of eccentricity and inclination for different values of AMR starting from the unstable point in $\psi = 0$, $a = 12000$ km $i_{e=0} = 20°$.

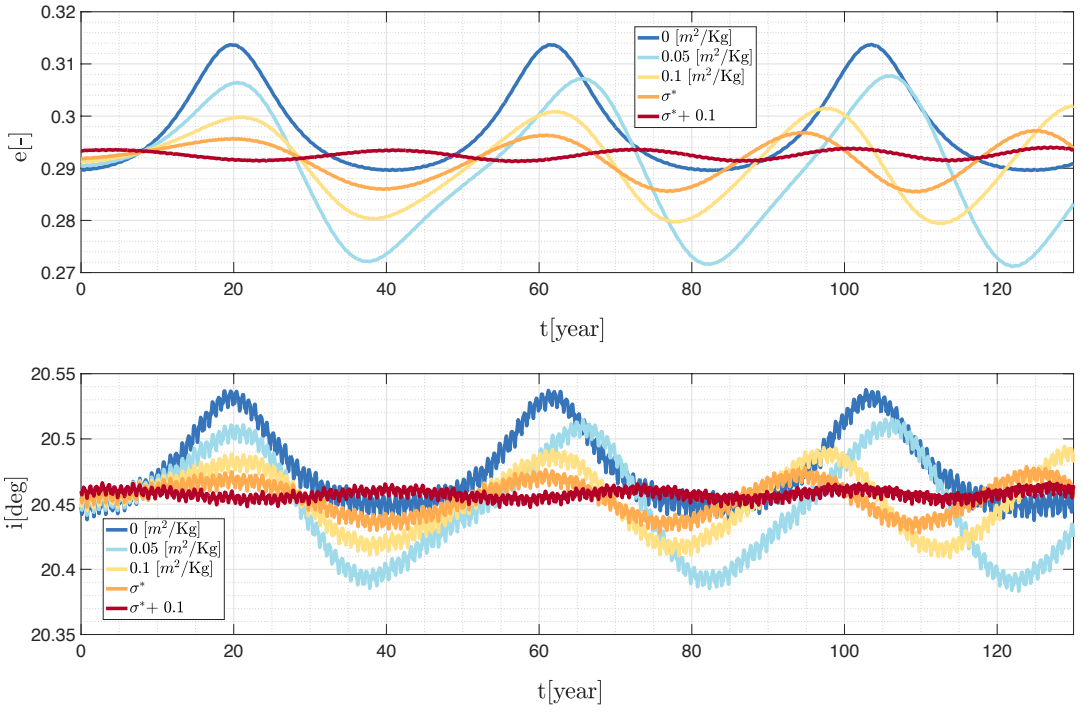

Figure 4.24: time evolution of eccentricity and inclination for different values of AMR starting from the unstable point in $\psi = \pi$, $a = 12000$ km $i_{e=0} = 20°$.

5 | Application of the extended model to de-orbiting design and debris dynamics

Using the techniques of dynamical system theory, this chapter extracts relevant information for mission design and debris analysis from the phase space portrait. As for the dynamics driven by SRP and Earth oblataness in the planar case Lucking et al. [13] and inclined case Gkolias et al. [15] models, it is shown how de-orbiting may occur within the extended SRP-J_2-Sun model. Then, in the last section, a synthetic debris population is propagated and analysed (Casanova et al. [51]), to see whether there exists a specific case of debris trapped in one of the resonances found.

5.1. State-of-art passive de-orbiting from $e = 0$

In the following Section, the state-of-art procedure to compute the minimum AMR to deorbit from a circular inclined orbit is outlined.

Phase space analysis may be used to determine the possible orbital elements and AMR for a reentry into Earth atmosphere. Given that the investigated dynamics do not affect the semi-major axis, natural de-orbiting can only occur if the eccentricity exceeds the critical value $e_{cr} = 1 - R_\oplus/a$. The minimum needed AMR is taken into account when this situation takes place at either $\psi = 0$ or $\psi = \pi$. Also, bearing the phase space behavior of Chapter 4 in mind, the steepest eccentricity growth from a circular orbit occurs at $\psi_{j,1} = \pi/2$ or $\psi_{j,1} = 3\pi/2$, following the stable direction associated with a hyperbolic equilibrium point or a libration curve associated with an elliptic equilibrium point. On the basis of this, and in line with the concept described in Lücking et al. [13] for the planar situation, the algorithm solves for the matching condition ($\mathcal{C}_{\mathrm{SRP}}$) the two-point boundary value problem described by the following equation:

$$\mathcal{H}_{\psi_j}(\Psi(e=0), \psi_{j,1}; L, \Pi) - \mathcal{H}_{\psi_j}(\Psi(e=e_{\mathrm{cr}}), \psi_{j,2}; L, \Pi) = 0, \quad \psi_{j,2} = 0 \vee \pi \tag{5.1}$$

This equation has two unknowns: the first is the value of AMR ($\mathcal{C}_{\text{SRP}}$), while the second is the value of inclination at the critical condition. Given that the inclination changes with eccentricity and that the second integral of motion Π is conserved, the final inclination reads (Gkolias et al. [15]):

$$\cos i_{cr} = \frac{\Pi}{n_1\sqrt{\mu a(1-e_{cr}^2)}} + \frac{n_2}{n_1}. \tag{5.2}$$

Re-arranging with respect to $\mathcal{C}_{\text{SRP}}$ and simplifying by variable changes substituting $\eta = \sqrt{1-e^2}$, it holds (Gkolias et al. [15]):

$$\begin{aligned} C_{\text{SRP}} = \frac{\mu\cos\psi_{j2}}{4L^{10}n_1^2\mathcal{T}_j\eta_{cr}^5 e_{cr}}\Big[&4L^9 n_1 n_3 n_\odot(\eta_{cr}-1)\eta_{cr} + \\ &-\mathcal{C}_{J_2}L^2(n_1^2-3n_2^2)\eta_{cr}^3(\eta_{cr}^3-1)\mu^3 + \\ &+6\mathcal{C}_{J_2}Ln_2\eta_{cr}(\eta_{cr}^4-1)\mu^3\Pi + 3\mathcal{C}_{J_2}(\eta_{cr}^5-1)\mu^3\Pi^2\Big] \end{aligned} \tag{5.3}$$

The minimum AMR to de-orbit from a circular inclined orbit is computed solving for $a \in [7000; 15000]$ $[km]$, $i_0 \in [0; 90°]$ and $\psi = 0$, the $\mathcal{C}_{\text{SRP}}$ from Equation (5.3). On the basis of its sign, it allocates the de-orbiting at the final critical angle $\psi = 0$ (if positive) or $\psi = \pi$ (if negative).

5.2. Passive de-orbiting from $e = 0$ in the extended model framework

Similar to what was done in the previous Section in the context of SRP-J_2 framework (and by several authors (see Section 1.1.1, including Giovannini and Colombo in [79]), in this Section, the procedure to calculate the lowest AMR necessary to de-orbit from a circular orbit within the context of the extended Hamiltonian model is given.
Starting from the initial angular configuration that lead to the steepest increase in eccentricity ($\psi_{j_1} = \pi/2 \vee 3\pi/2$), the minimum AMR required to reach $e = e_{cr} = 1 - R_\oplus/a$ and the final angular configuration that corresponds to the maximum eccentricity increase, is determined. The final condition is determined considering the derivative of the eccentricity with respect to the critical angle along an invariant curve (see Equation (4.27) for the explicit terms):

$$\frac{\mathrm{d}e}{\mathrm{d}\psi} = -\frac{\partial\mathcal{H}_j/\partial\psi_j}{\partial\mathcal{H}_j/\partial e}, \tag{5.4}$$

which, from the classical mathematical analysis theory, it is zero at a point of maximum or minimum. In particular, in the framework of the first resonance and in the extended model of resonance, at $\psi = 0$ and π there is a minimum. Instead at:

$$\cos\psi_{cr,j} = -\frac{8}{15}\frac{\mathcal{C}_{\mathrm{SRP}}}{an_{\odot}^2 e_{cr}}\left(\frac{\mathcal{T}_j}{\mathcal{K}_j}\right)_{e=e_{cr}} = \gamma_{cr}\mathcal{C}_{\mathrm{SRP}}, \tag{5.5}$$

the eccentricity reaches its maximum. Where for compactness:

$$\gamma_{cr} = -\frac{8}{15}\frac{1}{an_{\odot}^2 e_{cr}}\left(\frac{\mathcal{T}_j}{\mathcal{K}_j}\right)_{e=e_{cr}}, \tag{5.6}$$

given that it depends only on e_{cr}, a and the resonance j which are defined as input conditions.

By exploiting the conservation of $L = \sqrt{\mu a}$, Π and of the Hamiltonian, the following equation:

$$\mathcal{H}_j(0, \psi_{j1}; \mathit{\Pi}, L, \mathcal{C}_{\mathrm{SRP}}) = \mathcal{H}_j(e_{cr}, \psi_{j,cr}; \mathit{\Pi}, L, \mathcal{C}_{\mathrm{SRP}}), \tag{5.7}$$

is solved for $\mathcal{C}_{\mathrm{SRP}}$ (or equivalently AMR), where the initial condition is a circular orbit at a prescribed a, $i_{e=0}$, and $\psi_{j,1} = \pi/2 \vee 3\pi/2$ (although the initial Hamiltonian does not depend on the angular condition). The final condition is at e_{cr} and the angular configuration is matched such that the maximum eccentricity condition is exactly the critical one. The inclination at the critical eccentricity is computed exploiting the conservation of Π (proven in Appendix C):

$$\cos i_{cr} = \frac{\Pi_0}{n_1 L\sqrt{1-e_{cr}^2}} + \frac{n_2}{n_1}, \tag{5.8}$$

where n_1, n_2 depend on the resonance, and $\Pi_0 = L(-n_2 + n_1\cos i_{e=0})$. Therefore Equation (5.7) can be solved analytically. The analytical solution is derived thereafter.

First, the Hamiltonian formulation written in a more compact shape:

$$\begin{aligned}\mathcal{H}_j(\Psi_i, \psi_i; \mathit{\Pi}, L) = \Gamma_{J_2}\delta_i^{J_2}(\Psi_i; \mathit{\Pi}, L) + \Gamma_{\mathrm{SRP}}\mathcal{C}_{\mathrm{SRP}}\delta_i^{\mathrm{SRP}}(\Psi_i; \mathit{\Pi}, L)\cos\psi_{i,j} + \\ + \Gamma_{\odot}\delta_i^{\odot}(\Psi_i; \mathit{\Pi}, L)\cos 2\psi_{i,j} + n_3 n_{\odot}(\Psi_i + K).\end{aligned} \tag{5.9}$$

with:

$$\begin{aligned}\Gamma_{J_2} &= \frac{\mathcal{C}_{J_2}\mu^3}{4n_1^7 L^3}, & \delta_i^{J_2} &= \frac{(n_1^4\Psi_i^2 - 3(\mathit{\Pi} + n_1 n_2\Psi_i)^2)}{\Psi_i^5}, \\ \Gamma_{\mathrm{SRP}} &= -\frac{C_{\mathrm{SRP}}}{\mu}L^2, & \delta_i^{\mathrm{SRP}} &= \sqrt{1 - \frac{n_1^2\Psi_i^2}{L^2}}\mathcal{T}_{j,i}, \\ \Gamma_{\odot} &= -\frac{15}{32}\frac{L^4}{\mu^2}, & \delta_i^{\odot} &= \left(1 - \frac{n_1^2\Psi_i^2}{L^2}\right)\mathcal{K}_{j,i}.\end{aligned} \tag{5.10}$$

Then, imposing the initial condition of $e = 0$, the initial Hamiltonian is:

$$\mathcal{H}_0(\Psi_{e=0}, \psi; \Pi_{e=0}, L) = \Gamma_{J_2}\delta_i^{J_2}(\Psi_{e=0}; \Pi_{e=0}, L) + n_3 n_\odot(\Psi_{e=0} + K). \tag{5.11}$$

which is constant along the trajectory (invariant curve). The final condition reads:

$$\begin{aligned}\mathcal{H}_j(\Psi_{e=e_{cr}}, \psi_i; \Pi, L) = \Gamma_{J_2}\delta_i^{J_2}(\Psi_{e=e_{cr}}; \Pi, L) + \Gamma_{\text{SRP}}\mathcal{C}_{\text{SRP}}\delta_i^{\text{SRP}}(\Psi_i; \Pi, L)\cos\psi_{i,j} + \\ + \Gamma_\odot\delta_i^\odot(\Psi_i; \Pi, L)\cos 2\psi_{i,j} + n_3 n_\odot(\Psi_i + K).\end{aligned} \tag{5.12}$$

The final expression may be rearranged into a kind of second-order equation that is readily solved analytically:

$$\begin{aligned} a &= 2\Gamma_\odot\delta_2^\odot\gamma_{cr}^2 + \Gamma_{\text{SRP}}\gamma_{cr}\delta_2^{\text{SRP}}; \\ b &= 0; \\ c &= \Gamma_{J_2}(\delta_2^{J_2} - \delta_1^{J_2}) + n_3 n_\odot(\Psi_2 - \Psi_1) - \Gamma_\odot\delta_2^\odot; \\ \text{assembled:} \quad & a\mathcal{C}_{\text{SRP}}^2 + c = 0. \end{aligned} \tag{5.13}$$

It has been so far addressed de-orbiting along asymmetric equilibrium point orbits. If, however, the boundary conditions in terms of (a, $i_{e=0}$, AMR) are such that it takes place at $\psi = 0, \pi$, the solution equation can be reduced to:

$$\begin{aligned} C_{\text{SRP}} = \frac{\mu\cos\psi_{j2}}{4L^{10}n_1^2\mathcal{T}_j\eta_{cr}^5 e_{cr}}\Big[4L^9 n_1 n_3 n_\odot(\eta_{cr} - 1)\eta_{cr} + \\ -\mathcal{C}_{J_2}L^2(n_1^2 - 3n_2^2)\eta_{cr}^3(\eta_{cr}^3 - 1)\mu^3 + \\ +6\mathcal{C}_{J_2}Ln_2\eta_{cr}(\eta_{cr}^4 - 1)\mu^3\Pi + 3\mathcal{C}_{J_2}(\eta_{cr}^5 - 1)\mu^3\Pi^2\Big], \quad \psi_{j2} = 0 \vee \pi. \end{aligned} \tag{5.14}$$

Note that, it is not possible to apply Equation (5.13) to the de-orbiting in $\psi = 0$, because in all the dynamical regions (except from the (IV)), it does not exist a value of AMR such that $\cos\psi_{j_2} = 1$ (see Equation (5.5)). In region (IV), as explained in Chapter 3, the stability properties are exchanged due to the presence of a trans-critical bifurcation. It means that, the asymmetric points (see Figure 4.15), move toward $\psi = 0$ if AMR increases. Design of de-orbiting manoeuvre in this region could be the subject of future research.

De-orbiting algorithm

In this Section the procedure to develop a *de-orbiting map* in the extended SRP-J_2-Sun framework is described.

The solution of the two-point boundary value problem admits the de-orbiting at $\psi = \pi$, $\psi = 0$ or at $\psi \in]\pi/2, \pi[$ (where the borders are excluded because the first can be reached only if AMR $= 0$ m^2/kg, while the second implies $\cos\psi_{cr,j} = -1$). Consequently, the final angular configuration has to be determined. Following the procedure outlined in the flowchart Figure 5.1, for each $a \in [a_1, a_2]$, $i_{e=0} \in [0, 90°]$ and resonance j, it evaluates Equation (5.14)($\mathcal{C}_{\mathrm{SRP},0}$) for $\psi = 0$; if the sign of $\mathcal{C}_{\mathrm{SRP},0}$ is positive, the de-orbit occurs in $\psi = 0$, on the contrary it might take place at $\psi \in]\pi/2; \pi]$. Then, the minimum AMR assuming the re-entry at an asymmetric points is computed solving Equation (5.13)($\mathcal{C}_{\mathrm{SRP},as}$, only the positive solution). Then, if the angular configuration, computed substituting the just computed AMR in Equation (5.5), is within $]\pi/2; \pi[$, the final condition is on an asymmetric point. Otherwise, if $\cos\psi_{j_2}$ results ≤ -1, the minimum AMR should be computed imposing $\psi = \pi$ in Equation (5.14), coming to the conclusion that the object terminates in $\psi = \pi$.

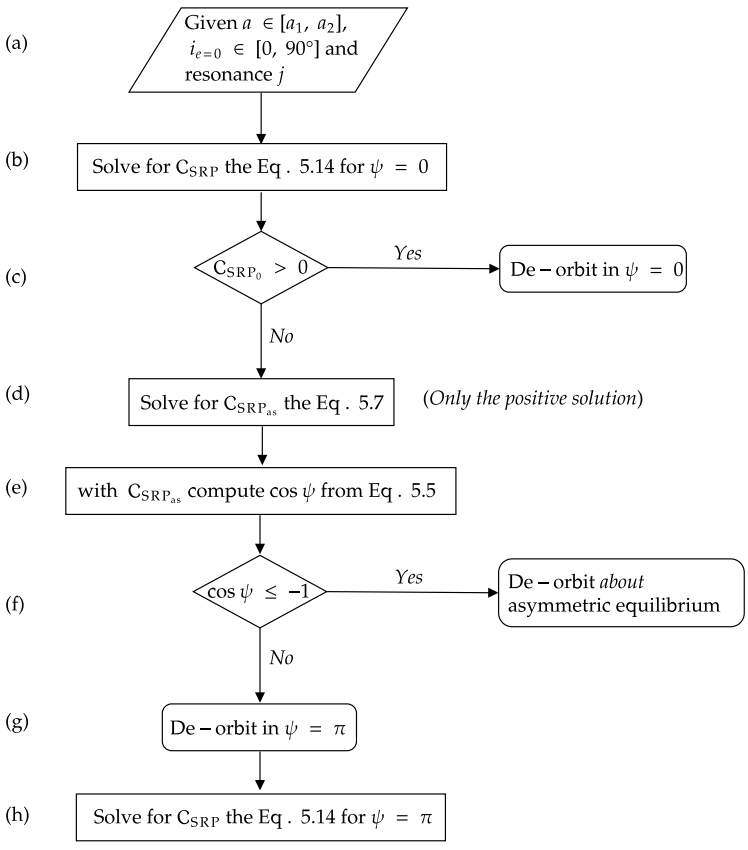

Figure 5.1: Flowchart of the new de-orbit strategy from a circular inclined orbit.

Results

Figure 5.2 shows the computations for fixed value of semi-major axis $a = 12200$ km. Despite the fact that the AMR computed in the two frameworks is quite similar, there are some differences near the position $(a, i_{e=0})$ of the bifurcation, as the AMR required for re-entry approaches 0 and, as it is well known, the Sun gravity may become significant. In particular it highlights that the bifurcation point shifts toward higher inclination under the effect of the coupled SRP-J_2-Sun dynamics (see also Figure 5.3).

The needed AMR for the re-entry configuration in an asymmetric point is more in the SRP-J_2-Sun model than in the previous model. Conversely, the opposite is true when $\psi = 0$. Moreover, it is possible to see in Figure 5.2, that the algorithm starts to compute the re-entry solution in the range $]\pi/2, \pi[$ (`if` statement (f) in Figure 5.1), when the inclination of the circular orbit is near the bifurcation point.

Note that, the comparison between the AMR computed in the inclination range between the two bifurcations (see Figure 5.2) lacks of significance because the object de-orbits to $\psi = 0$ in the case of SRP-J_2 dynamics, and to $\psi \in]\pi/2, \pi]$ for the SRP-J_2-Sun dynamics.

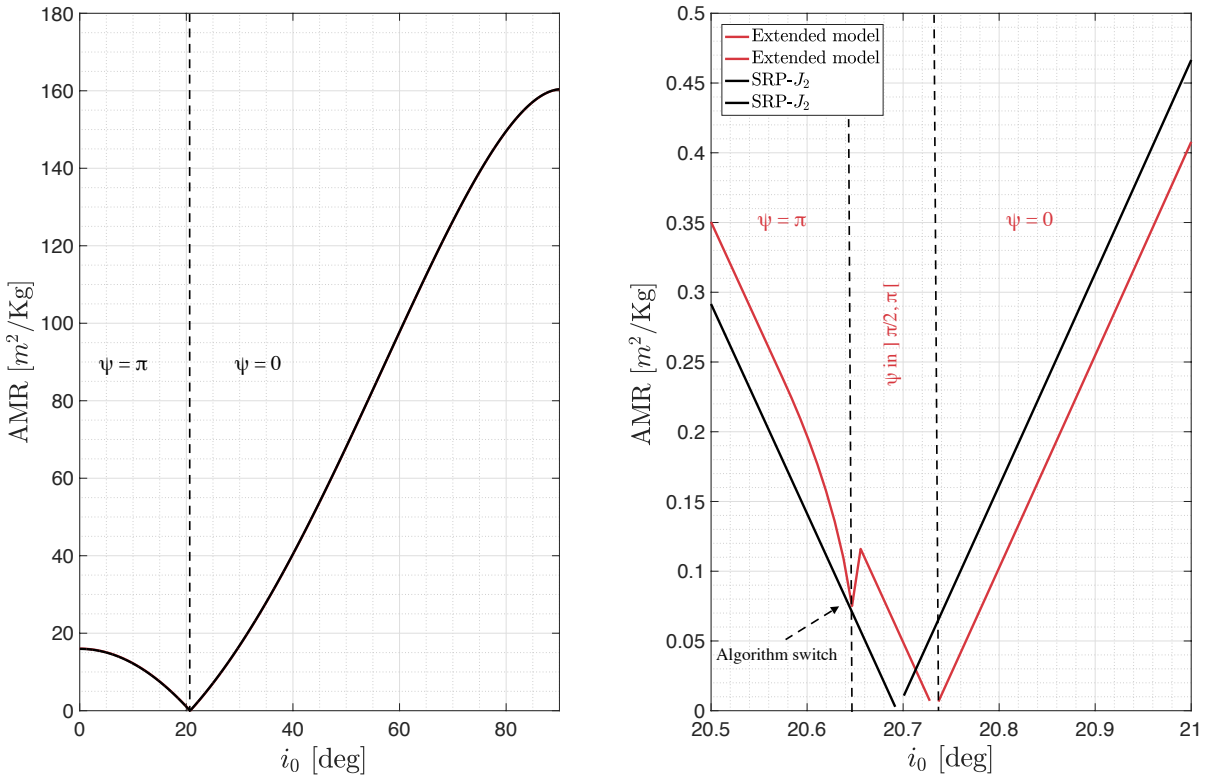

Figure 5.2: Minumum AMR to de-orbit from circular orbit with $a = 12197$ km and inclinations $i_0 \in [0, 90]$ deg computed using the SRP-J_2 and extended models.

In Figure 5.3, Figure 5.4 and Figure 5.5, the comparison of the computation on the two frameworks are reported. Figure 5.3 reports the complete de-orbiting map for all the final angular configurations; even if it is not possible to see, the bifurcation lines (in white) are not coincident: the bifurcation computed in the extended model is slightly shifted towards higher inclinations. In Figure 5.4 the final configuration is $\psi \in]\pi/2, \pi]$ and in Figure 5.5 in $\psi = 0$. The AMR estimated to de-orbit towards $\psi = 0$ in the extended model is smaller than the one computed in the literature, however the opposite is true if the final configuration is $\psi \in]\pi/2, \pi]$. Figure 5.6 and Figure 5.7 are show two example of de-orbiting orbits. In the first figure, it is possible to see the de-orbiting toward π, specifically on the left in the extended dynamics when the object re-enters at an asymmetric point, and on the right, the method derived from the literature. In the second figure, where $\psi = 0$ is used for comparison, it is possible to see that with the newly derived strategy, the required AMR is less than with the previous manoeuvre.

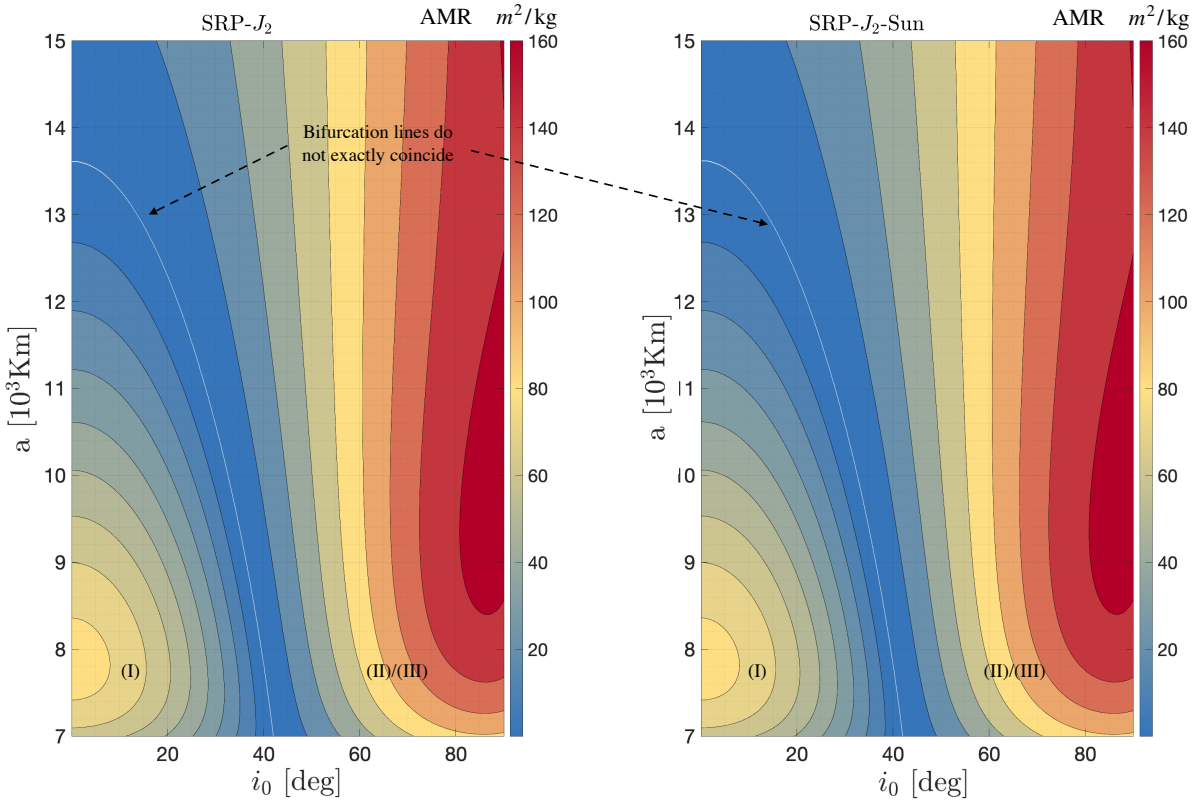

Figure 5.3: Left: de-orbiting map in the framework of SRP-J_2.,rigth: de-orbiting map in the framework of SRP-J_2-Sun.

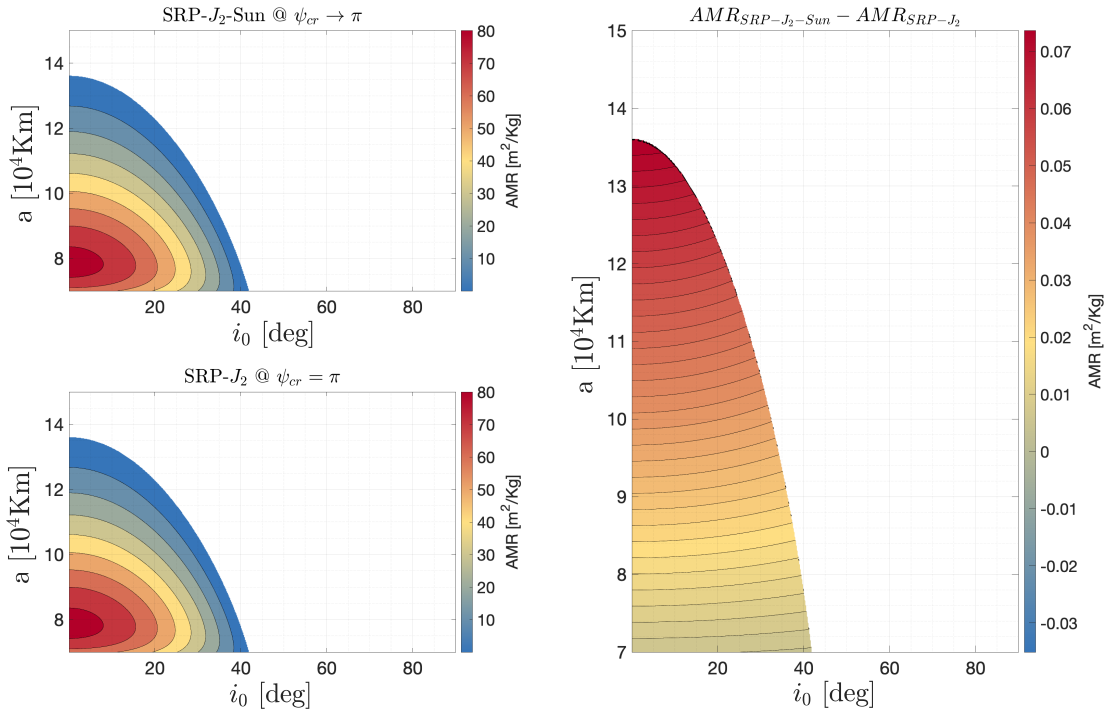

Figure 5.4: De-orbiting map in the framework of SRP-J_2-Sun near $\psi = \pi$ on the top left and on $\psi = \pi$ on the bottom left. Comparison between them on the right.

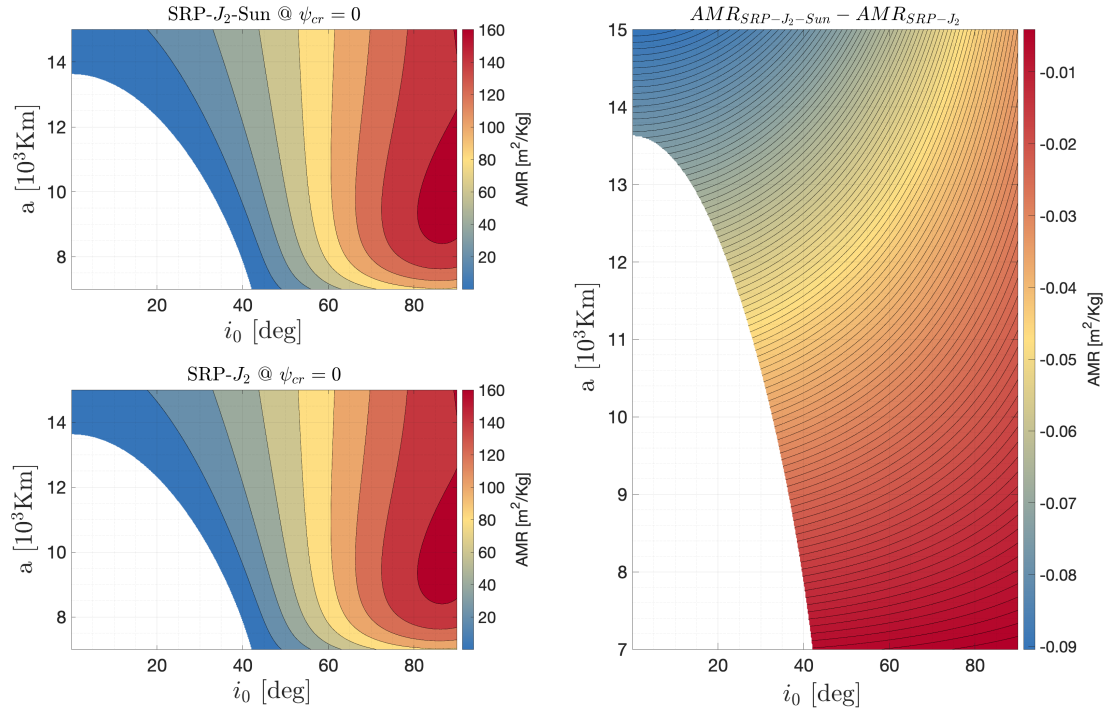

Figure 5.5: De-orbiting map in the framework of SRP-J_2-Sun on $\psi = 0$ on the top left and on $\psi = 0$ on the bottom left. Comparison between them on the right.

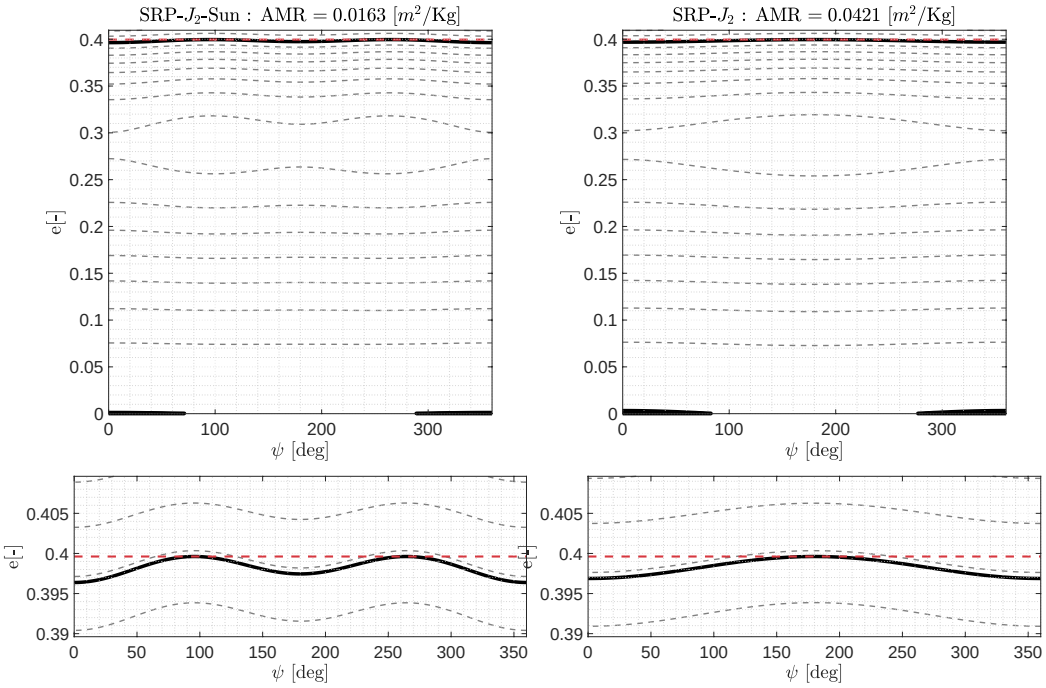

Figure 5.6: Phase space with de-orbit trajectory from $a = 10623.2$ km, $i_{e=0} = 29.77°$. Left in SRP-J_2-Sun and right in the SRP-J_2 frameworks.

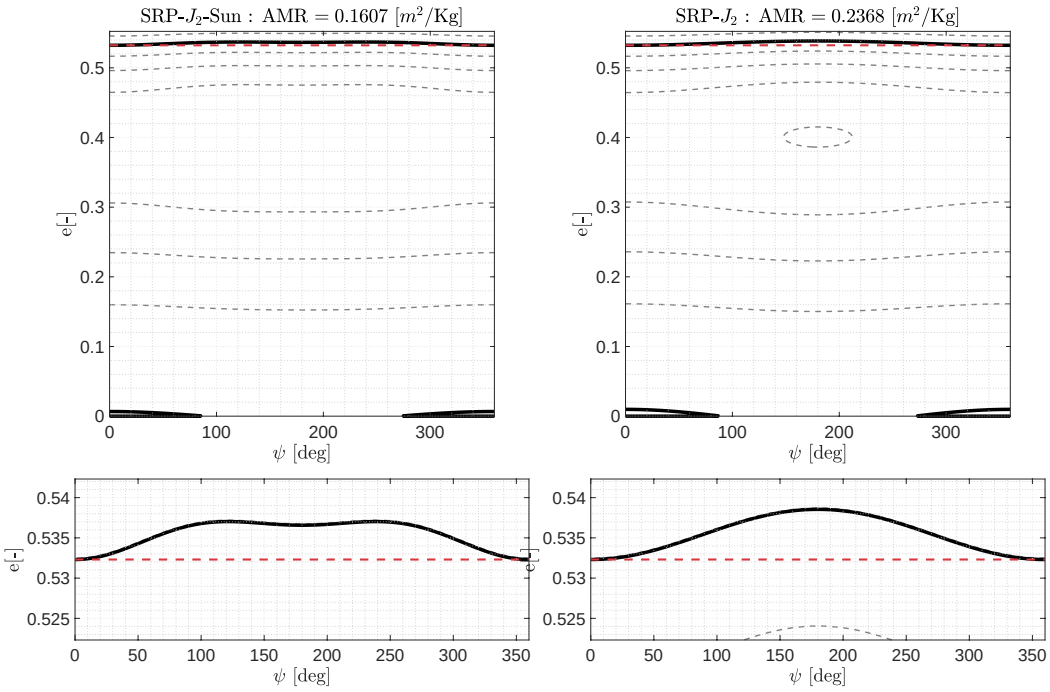

Figure 5.7: Phase space with de-orbit trajectory from $a = 13637.3$ km, $i_{e=0} = 41.90°$. Left in SRP-J_2-Sun and right in the SRP-J_2 frameworks.

5.3. De-orbiting from an unstable equilibrium at $\psi = \pi$

In the following Section, the initial orbit is assumed to be elliptical.
The strategy presented assumes that the spacecraft is initially located at the unstable equilibrium point $\psi = \pi$ of the extended model, then the spacecraft reaches a point of maximum eccentricity at the angular configuration of the asymmetric equilibrium point. As stated many times in this thesis, during the evolution of the phase space, the semi-major axis does not change under the dynamics considered, hence a natural de-orbiting can take place only if the eccentricity increases as much as to attain the critical value $e_{cr} = 1 - R_\oplus/a$. The link equation between the Hamiltonians of two generic initial and final conditions is considered:

$$\mathcal{H}_j(\Psi_1, \psi_1, j; \Pi, L, \mathcal{C}_{\text{SRP}}) = \mathcal{H}_j(\Psi_2, \psi_2, j; \Pi, L, \mathcal{C}_{\text{SRP}}), \tag{5.15}$$

where (1, 2) are the initial and final condition along an Hamiltonian level trajectory, j is the resonance considered, Π is the second integral of motion, $L = \sqrt{\mu a}$ and $\mathcal{H}_j$ expressed as in Equation (5.9) for an easier reading:

$$\begin{aligned}\mathcal{H}_j(\Psi_i, \psi_i; \Pi, L) = \Gamma_{J_2}\delta_i^{J_2}(\Psi_i; \Pi, L) + \Gamma_{\text{SRP}}\mathcal{C}_{\text{SRP}}\delta_i^{\text{SRP}}(\Psi_i; \Pi, L)\cos\psi_{i,j} + \\ + \Gamma_\odot\delta_i^\odot(\Psi_i; \Pi, L)\cos 2\psi_{i,j} + n_3 n_\odot(\Psi_i + K).\end{aligned} \tag{5.16}$$

with:

$$\begin{aligned}\Gamma_{J_2} &= \frac{\mathcal{C}_{J_2}\mu^3}{4n_1^7 L^3}, & \delta_i^{J_2} &= \frac{(n_1^4\Psi_i^2 - 3(\Pi + n_1 n_2 \Psi_i)^2)}{\Psi_i^5}, \\ \Gamma_{\text{SRP}} &= -\frac{C_{\text{SRP}}}{\mu}L^2, & \delta_i^{\text{SRP}} &= \sqrt{1 - \frac{n_1^2\Psi_i^2}{L^2}}\mathcal{T}_{j,i}, \\ \Gamma_\odot &= -\frac{15}{32}\frac{L^4}{\mu^2}, & \delta_i^\odot &= \left(1 - \frac{n_1^2\Psi_i^2}{L^2}\right)\mathcal{K}_{j,i}.\end{aligned} \tag{5.17}$$

Region of applicability

As seen in Chapter 4, the maximum eccentricity reached following the trajectory starting from an unstable point in π for a defined $(i_{e=0},\ a)$[1], depends on the value of AMR. In particular, it is maximum at AMR $= 0\ m^2/\text{kg}$ and cancels out at the associated bifurcation value (see Figure 4.22). Therefore, for each semi-major axis in the range from 9000 km to 15000 km and for eccentricities in the range $]0,\ 1[$, the resonant inclination for the

[1] the inclination of an hypothetical circular orbit is taken as coordinate since it allows to compute a reference $\Pi = (-n_1 + n_2\cos i_{e=0})\sqrt{\mu a}$, which "generates" the phase space portrait.

equilibrium $\psi = \pi$ has been computed.

Then, if it exists, the maximum eccentricity reached for a virtual [2] object with AMR = 0 m^2/kgis found at the critical angle $\psi = \pi/2$, and its value is found by solving:

$$\mathcal{H}_j(\Psi_1, \pi, j; \Pi, L, 0) = \mathcal{H}_j(\Psi_2, \pi/2, j; \Pi, L, 0). \tag{5.18}$$

For the prescribed eccentricity and semi-major axis range, the re-entry condition is achieved if $e_2 \geq e_{cr}$. On the other hand, if the maximum eccentricity is below the critical one or the eccentricity of $\psi = \pi$ is already above the critical, the point is outside the feasibility region. The graph in Figure 5.8 shows the upper and lower limit of applicability of the manoeuvre: the lower limit delimits a region in which the maximum eccentricity is below the re-entry condition, while the upper limit delimits the region in which the eccentricity of the point $\psi = \pi$ is already above the critical one. The color-bar shows the eccentricity of the stable point in $\psi = \pi$ and AMR = 0 m^2/kg . Therefore, the applicability of the manoeuvre is in between the two borders.

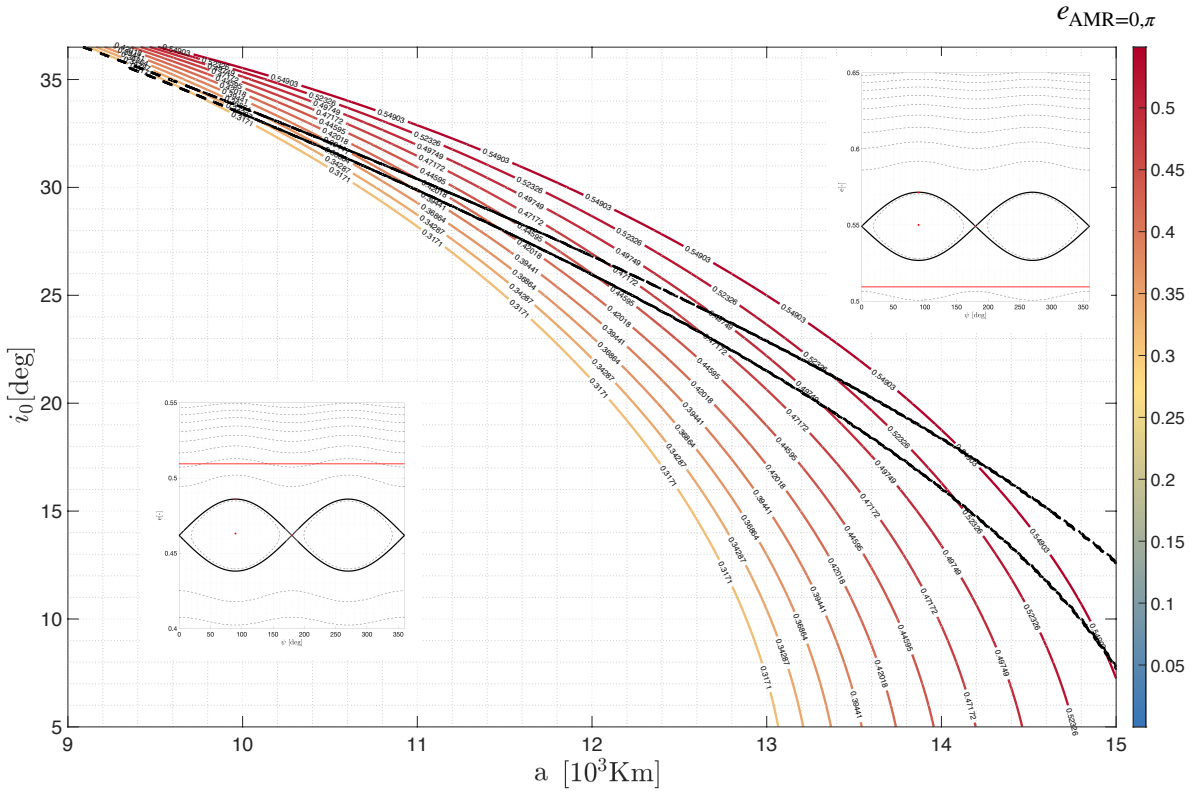

Figure 5.8: De-orbiting strategy validity limit at AMR = 0 m^2/kg

[2] an object with AMR = 0 m^2/kg does not physically exist

Initial and Final Conditions

The disposal manoeuvre starts from an unstable equilibrium point located at $\psi = \pi$ of the extended Hamiltonian model. This allows the object to exploit the double lobe dynamics which drives it toward the Earth surface at the critical angle of the asymmetric equilibrium. The initial angular configuration is the known parameter of the initial condition; the eccentricity, inclination, and AMR, are unknown. This because, fixed the semi-major axis and the angle ψ, the eccentricity of the equilibrium point (and hence its inclination) depend on the unknown AMR. An iterative technique is designed to calculate the starting condition. It is assumed as initial guess that the initial eccentricity is that of the equilibrium at $\psi = \pi$ and AMR $= 0\ m^2/\text{kg}$. The object final condition is at $e_2 = e_{cr} = 1 - R_\oplus/a$ and i_{cr} computed from the conservation of the Π.

Two-point boundary value problem

Following the idea described above, the spacecraft has to be placed in an unstable equilibrium point in $\psi_1 = \pi$ at a defined eccentricity, with initial inclination computed from the resonant condition Equation (4.34) at AMR $= 0\ m^2/\text{kg}$. As first guess, it is assumed that the eccentricity of the initial point, is the one computed at AMR $= 0\ m^2/\text{kg}$, $\psi = \pi$ (the assumption is reasonable since the very low value of AMR and under the hypothesis that AMR $< \sigma^*$). Then, the re-entry is achieved at $e_2 = e_{cr}$, reached at the angular configuration:

$$\cos\psi_{2,j} = -\frac{8}{15}\frac{\mathcal{C}_{\text{SRP}}}{a n_\odot^2 e^{\text{eq},\pi/2}}\left(\frac{\mathcal{T}_j}{\mathcal{K}_j}\right)_{e=e^{\text{eq},\pi/2}} = \gamma_{\pi/2}\mathcal{C}_{\text{SRP}}, \tag{5.19}$$

where $e^{\text{eq},\pi/2}$ is the eccentricity of the equilibrium point computed at $\psi = \pi/2$ and AMR $= 0\ m^2/\text{kg}$ (it is known from the theory developed that the eccentricity of the asymmetric point does not change below the bifurcation AMR).
Rearranging Equation (5.15) and substituting in $\cos\psi_{cr}$ the value computed in Equation (5.5), the value of $\mathcal{C}_{\text{SRP}}$ can be derived solving analytically the second order equation:

$$\begin{aligned}\Gamma_{J_2}\delta_1^{J_2}(\Psi_1;\Pi,L) - \Gamma_{\text{SRP}}\mathcal{C}_{\text{SRP}}\delta_1^{\text{SRP}}(\Psi_1;\Pi,L) + \Gamma_\odot\delta_1^\odot(\Psi_1;\Pi,L) + n_3 n_\odot\Psi_1 = \\ = \Gamma_{J_2}\delta_2^{J_2}(\Psi_2;\Pi,L) + \Gamma_{\text{SRP}}\delta_2^{\text{SRP}}(\Psi_1;\Pi,L)\gamma_{\pi/2}\mathcal{C}_{\text{SRP}}^2 + \\ +2\Gamma_\odot\delta_2^\odot(\Psi_1;\Pi,L)\gamma_{\pi/2}^2\mathcal{C}_{\text{SRP}}^2 - \Gamma_\odot\delta_2^\odot(\Psi_1;\Pi,L) + n_3 n_\odot\Psi_2.\end{aligned} \tag{5.20}$$

The above equation can be rearranged in a canonical shape:

$$\kappa_1\mathcal{C}_{\text{SRP}}^2 + \kappa_2\mathcal{C}_{\text{SRP}} + \kappa_3 = 0. \tag{5.21}$$

with the following coefficients:

$$\begin{aligned}
\kappa_1 &= 2\Gamma_{\odot}\delta_2^{\odot}(\Psi_1;\Pi,L)\gamma_{\pi/2}^2 + \Gamma_{\mathrm{SRP}}\delta_2^{\mathrm{SRP}}(\Psi_1;\Pi,L)\gamma_{\pi/2},\\
\kappa_2 &= \Gamma_{\mathrm{SRP}}\mathcal{C}_{\mathrm{SRP}}\delta_1^{\mathrm{SRP}}(\Psi_1;\Pi,L)\\
\kappa_3 &= \Gamma_{J_2}(\delta_2^{J_2}(\Psi_1;\Pi,L) - \delta_1^{J_2}(\Psi_1;\Pi,L)) + n_3 n_{\odot}(\Psi_2-\Psi_1) - \Gamma_{\odot}(\delta_1^{\odot}+\delta_2^{\odot}).
\end{aligned} \tag{5.22}$$

The solution, if exists, has to be selected positive and lower than the bifurcation value computed at that altitude and inclination.

De-orbiting algorithm

After the definition of the beginning and final conditions, as well as the equations involved in the de-orbiting design, the technique used to calculate the required AMR to assure re-entry is detailed. Following the procedure in the flowchart Figure 5.9, it is possible to compute the *de-orbiting map* presented in Figure 5.10.
For any feasible point computed in Figure 5.8, it is assumed as initial guess for the starting eccentricity, the one associated to the equilibrium point in $\psi = \pi$ and AMR $= 0\ m^2/\mathrm{kg}$. With this initial condition, it is possible to compute the $\mathcal{C}_{\mathrm{SRP}}^{(0)}$ solving the second order equation Equation (5.21). Then, since the eccentricity of the initial conditions depends on the AMR, the procedure is iterated over AMR until a defined stopping condition (i.e., $|e_1^1 - e_1^0| < \mathrm{tol} = 0.01\ e_{\mathrm{AMR}=0,\pi}$ is reached. The eccentricity of the equilibrium point $\psi = \pi$, $\mathcal{C}_{\mathrm{SRP}}^{(0)}$ is computed solving the non-linear system of equation Equation (4.27). Then, if the stopping condition is satisfied, the algorithm stops. The computed AMR is the highest value that guarantees re-entry; if a higher value is chosen, the width of the double-lobe is reduced, and hence de-orbiting is not assured.

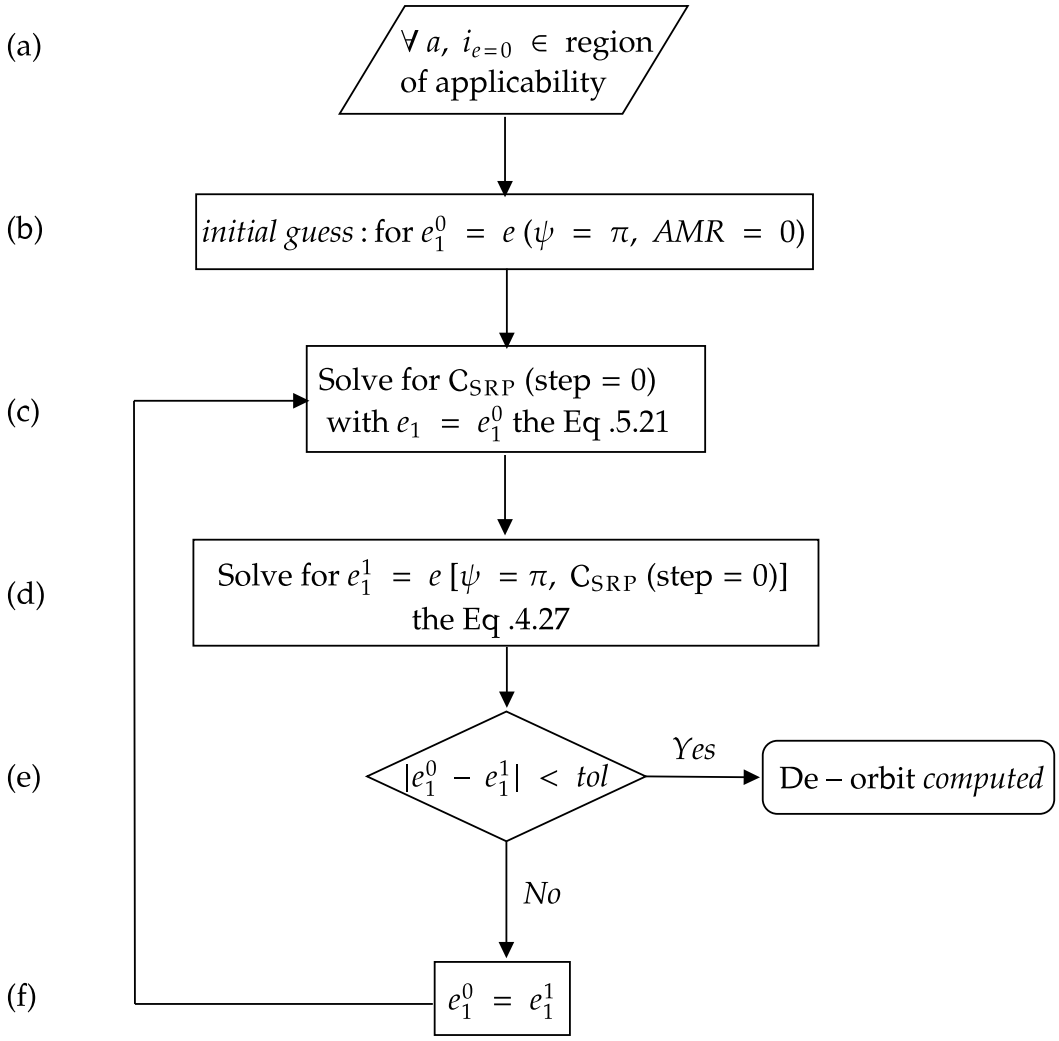

Figure 5.9: Flowchart of the new de-orbit strategy starting from an unstable condition.

Results

In Figure 5.10 the *de-orbiting map* is reported, showing that the maximum AMR which guarantees the re-entry is higher toward the upper limit and lower towards the lower limit. This may be explained by the fact that the width of the double-lobe eye is inversely proportional to the AMR; hence, if the object is closer to the critical condition, the width of the lobe that assures re-entry is smaller, resulting in a greater maximum AMR. The computed AMR is intended as a maximum value, which imposes an upper restriction: if the AMR is greater than the computed maximum, the technique is inapplicable. The bottom limit is technical in nature: there is no object with AMR $= 0\ m^2/\text{kg}$.
Namely, the de-orbiting trajectory at $a \approx 12000$ km for $i_0 = 25.99°$ on the left and $i_0 = 26.38°$ on the right, are reported in Figure 5.11.

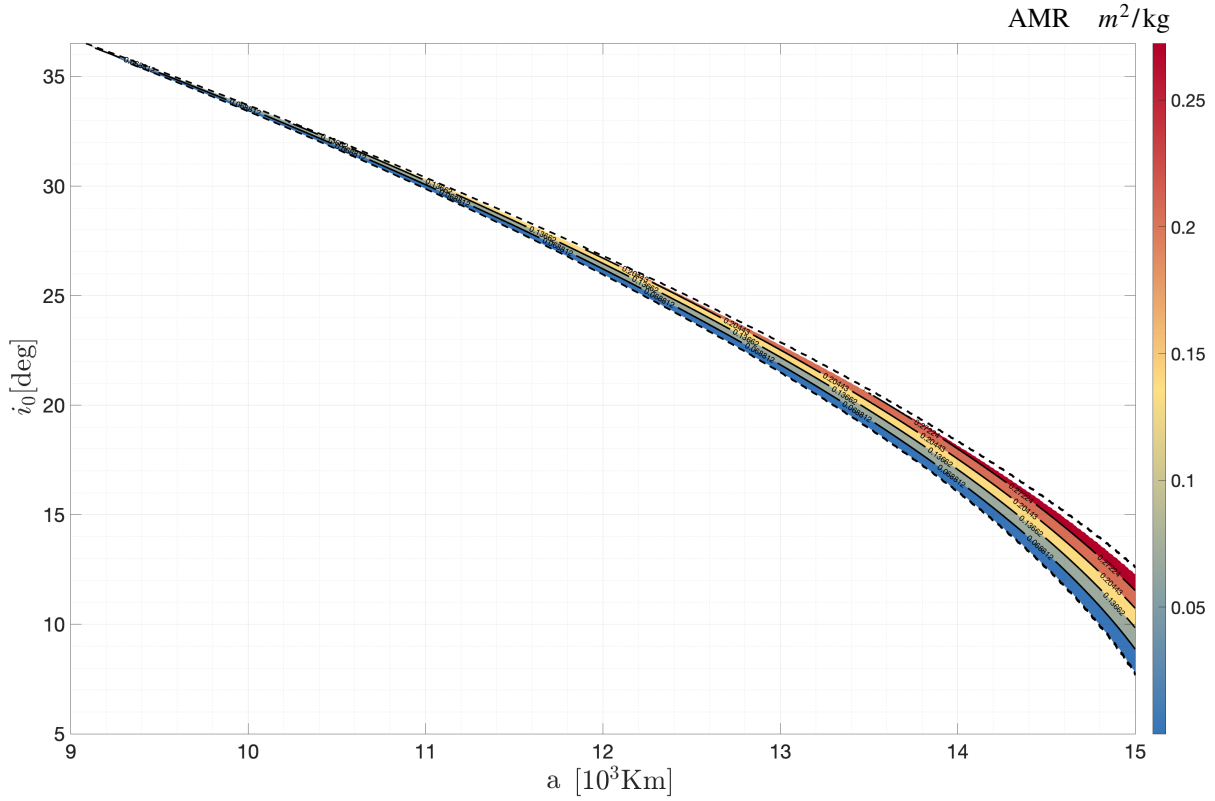

Figure 5.10: Maximum AMR for deorbit from a given a and inclination of initially circular orbit i_0

The maximum AMR sufficient for the de-orbiting in the first case is AMR $= 0.0012\ m^2/\text{kg}$ while in the second case AMR $= 0.1063\ m^2/\text{kg}$. The computed value is intended to be used together with technology limitations, for example the minimum AMR achievable for a spacecraft has to be under that value to guarantee the de-orbit.

Practical use

This innovative strategy is exploitable only if the spacecraft is placed initially on the unstable point in $\psi = \pi$. This could be performed if, for example, during the mission life the spacecraft is placed in $\psi = \pi$ with AMR $\geq \sigma^*_{i,j}$, hence at a stable equilibrium of the SRP-J_2 framework. Then, once the mission is finished, to start the disposal manoeuvre, the spacecraft reduces its AMR until it goes below $\sigma^*_{i,j}$. By following the double-lobe Hamiltonian curve, it is driven toward the Earth atmosphere.

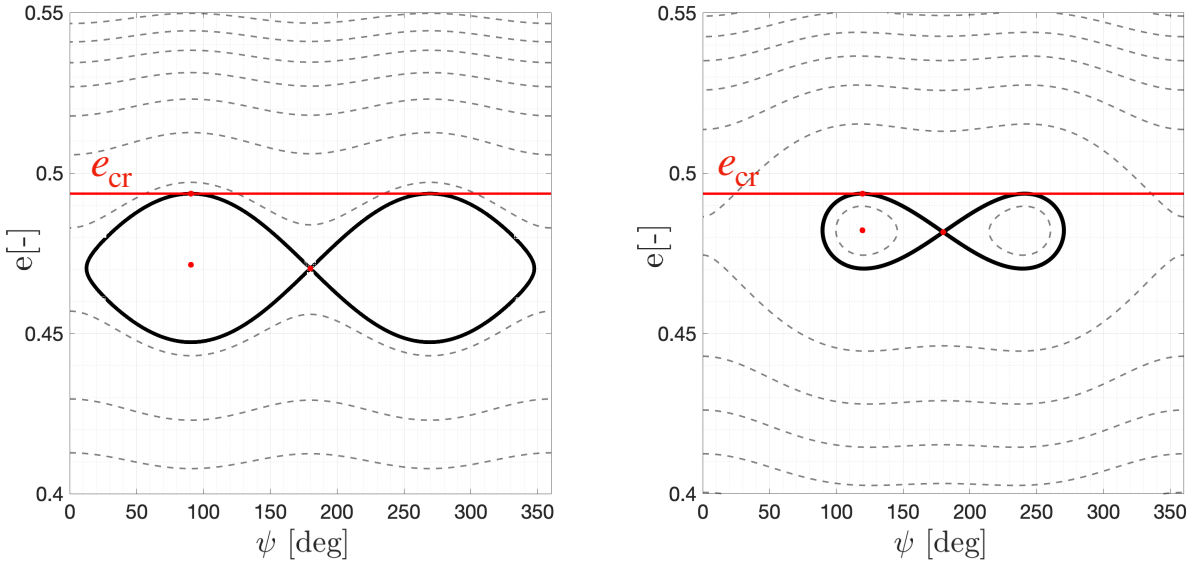

Figure 5.11: Example of de-orbiting configuration at 12000 km for $i_0 = 25.99°$, AMR $= 0.0012\ m^2/\text{kg}$ on the left and $i_0 = 26.38°$, AMR $= 0.1063\ m^2/\text{kg}$ on the right.

5.4. Debris analysis

In this Section the theoretical results obtained in Chapter 4 are applied to the debris dynamics in order to deepen the knowledge about the mechanism which drives the low/medium AMR debris to accumulate in space. In particular, under certain circumstances, the debris accumulate in peculiar regions of the space as consequence of the interaction with the coupled SRP-J_2-Sun perturbation.
As suggested by Alessi et al. [14] and similarly to what was done in Schaus et al. [71] for the case of the "resonant reentry corridors", it is interesting to analyse the space debris catalog to see whether there exists a specific case trapped in one of the resonances found. Whereas a database of small debris with high AMR is not yet available, the NASA standard breakup model (Bade et al. [66]) is used to generate a fictitious debris population, which is then propagated by the semi-analytical model described in Chapter 2 and Appendix A. Then the resulting distribution of the objects is explained through the mathematical model presented in this thesis.

5.4.1. Dynamical Mapping

In this Section, the dynamical mapping tool is used to provide an overview of the debris dynamics, which are analysed in depth in following sections. This work examines a dynamical indicator related with the development of the orbit eccentricity, which is

primarily responsible for the perigee variation and, therefore, the re-entry time (Gkolias and Colombo [69]):

$$\Delta e = |e_{MAX} - e_{min}| \tag{5.23}$$

For the scope of this analysis, only the dynamical map (e, i) is investigated with a grid of 150 $\times$ 150 initial conditions in the ranges $e \in [0, 0.5]$ and $i \in [0°, 90°]$. In particular in Figure 5.12 an object with AMR = 0.01 m^2/kg is propagated from a = 13000 km. For the value of AMR considered, at that semi-major axis, the value of $\sigma^*_{1,1}$ is greater than the considered AMR, hence the phase space presents *asymmetric* equilibrium points near $\psi = \pi/2$.

The first three maps in the figure, are integrated starting from critical angle of $\psi = 0$, $\pi/2$ and π in order to make the map highlight the resonances. Note that, for the first resonance, since the critical angle is the sum of Ω and ω, in this case it has been decided to take $\Omega_0 = 0$ while varying the initial ω_0.

The top right map of Figure 5.12 presents on the left portion of the plot a peculiar resonant branch. Differently from the case $\psi = 0$ and $\psi = \pi$, an object propagated with initial $\psi = \pi/2$ shows in its dynamical map the center of the stable *asymmetric* point, while the other two plots show the center of other two equilibrium points (*symmetric*), but in this case are unstable. The stability behaviour is described by the values of Δe, indeed in the plot of $\psi = \pi/2$, the resonant branch in the left corner presents a low Δe route (the eye center of the asymmetric point) between two high Δe branches which are the upper and lower eyelids. The center of the resonance has also been computed solving Equation (4.40) for $\psi = \pi/2$ and compared with the real position of the center of the asymmetric point computed by solving Equation (4.23).

In the bottom left map, it is possible to see a small portion of the resonant branch which has a smaller value of Δe. This because, increasing the AMR from 0 to $\sigma^*_{1,1}$ the asymmetric stable point moves from $\psi = \pi/2$ to $\psi = \pi$, this results in the dynamical map of $\psi = \pi$ in a increasingly stable resonant center.

In the last plot of Figure 5.12 the angle-averaged Δe plot is presented as the mean value of the three Δe computed.

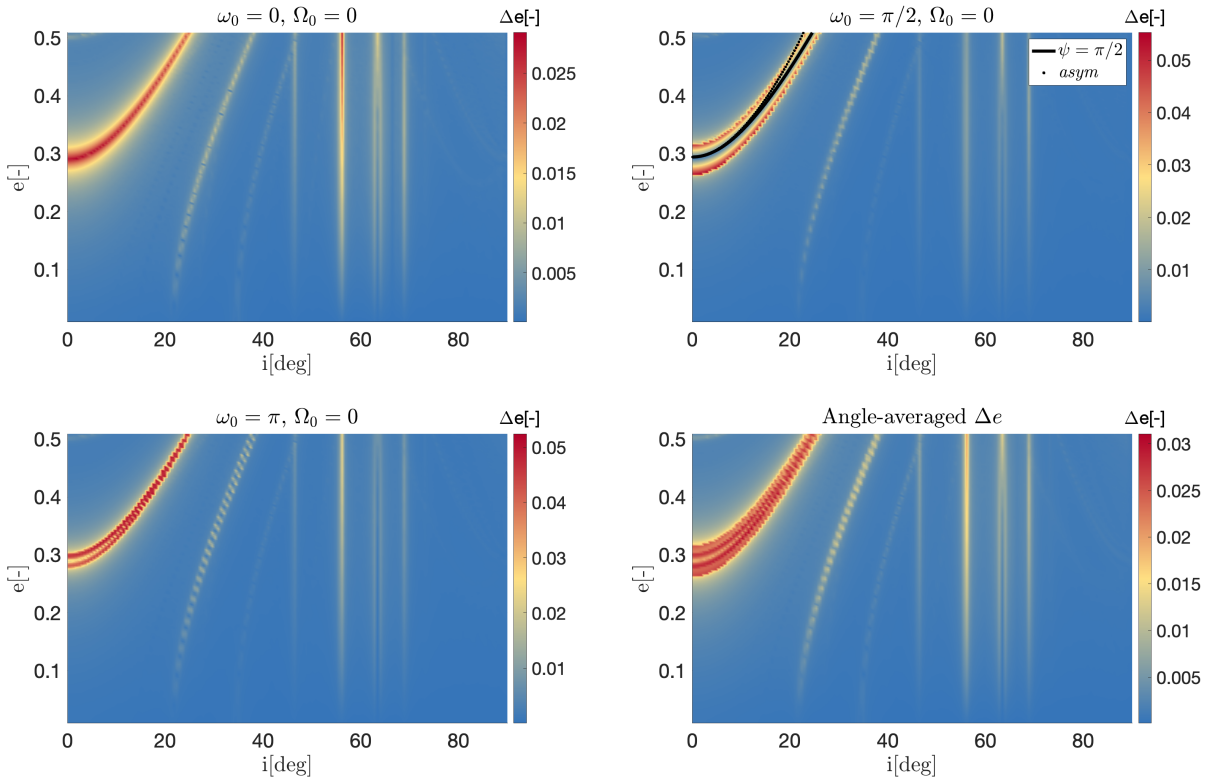

Figure 5.12: Cartography analysis reporting the value of Δe in the plane (e,i) for AMR = 0.01 m^2/kg at a = 13000 km. Dashed black line the analytical position of the first resonance computed with Equation (4.40).

The dynamics that causes the capture of debris

In Figure 5.13, Figure 5.14 and Figure 5.15, the dynamics an object is propagated from three initial critical angle and for three AMR using the semi-analytical propagator defined in Appendix A, and then compared to their Hamiltonian phase space at $i_0 = 20°$. From the first two plot it is possible to see that near $\psi = \pi/2$ the object (depicted in green) stays near the stable point, while, this is not true if it is propagated starting from $\psi = 0$ (blue line) and $\psi = \pi$ (red line) which are unstable points. The object considered in Figure 4.21 has AMR = 5 m^2/kg, which is greater than the discriminant $\sigma^* \approx 0.15$ m^2/kg at $a = 13000$ km and $i = 20°$, hence the object placed initially in $\psi = \pi/2$ won't librate around an asymmetric stable point but rather around the stable point in $\psi = \pi$, typical of the SRP-J_2 model.

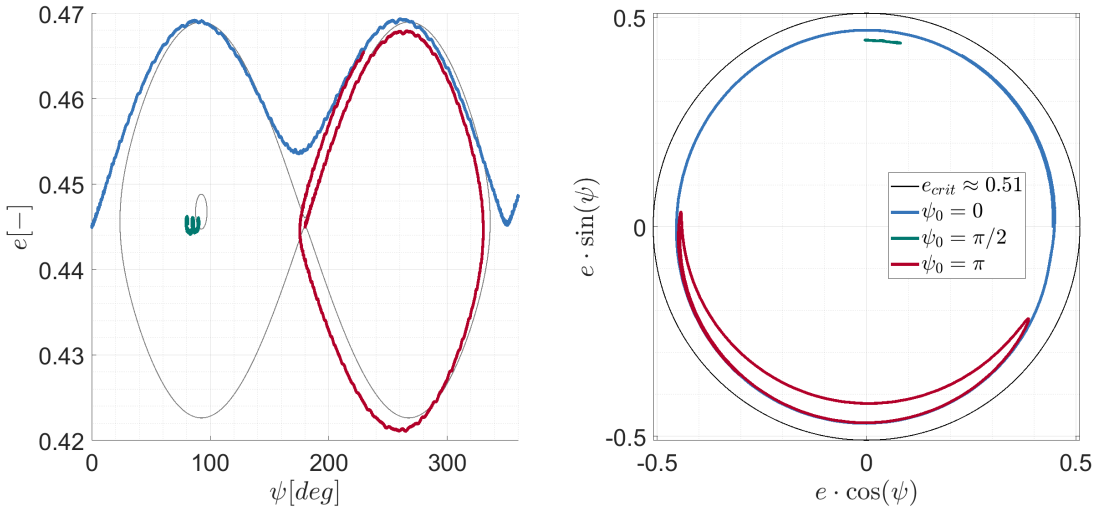

Figure 5.13: Representation in the plane (e, ψ) and in the Poincare plane ($e\cos\psi, e\sin\psi$) of the trajectories propagated with the Hamiltonian propagator (light gray) and semi-analytical propagator (coloured lines) for AMR $= 0.01\ m^2/\text{kg}$, $a = 12078$ km and $i_{e=0} = 25.5°$

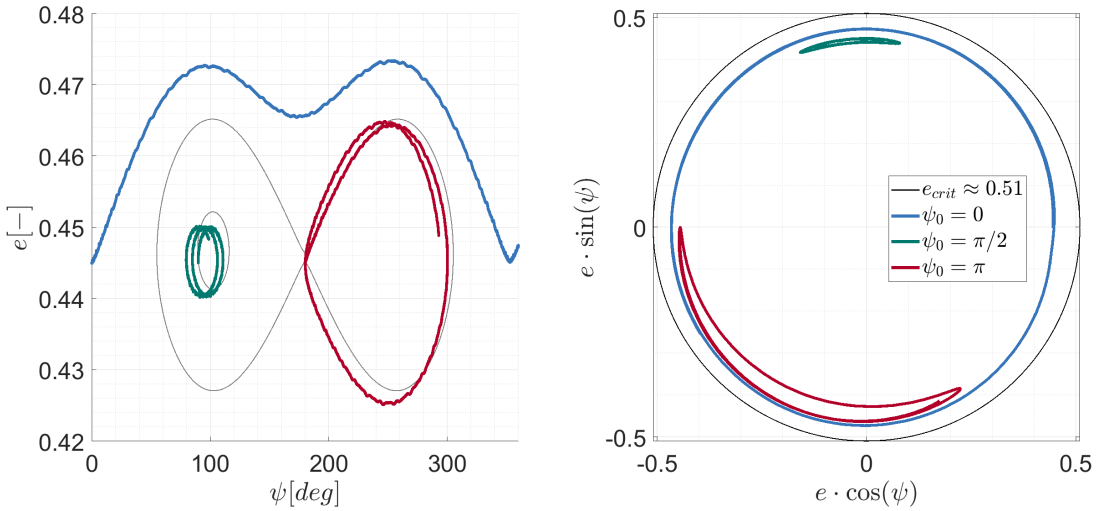

Figure 5.14: Representation in the plane (e, ψ) and in the Poincare plane ($e\cos\psi, e\sin\psi$) of the trajectories propagated with the Hamiltonian propagator (light gray) and semi-analytical propagator (coloured lines) for AMR $= 0.05\ m^2/\text{kg}$, $a = 12078$ km and $i_{e=0} = 25.5°$.

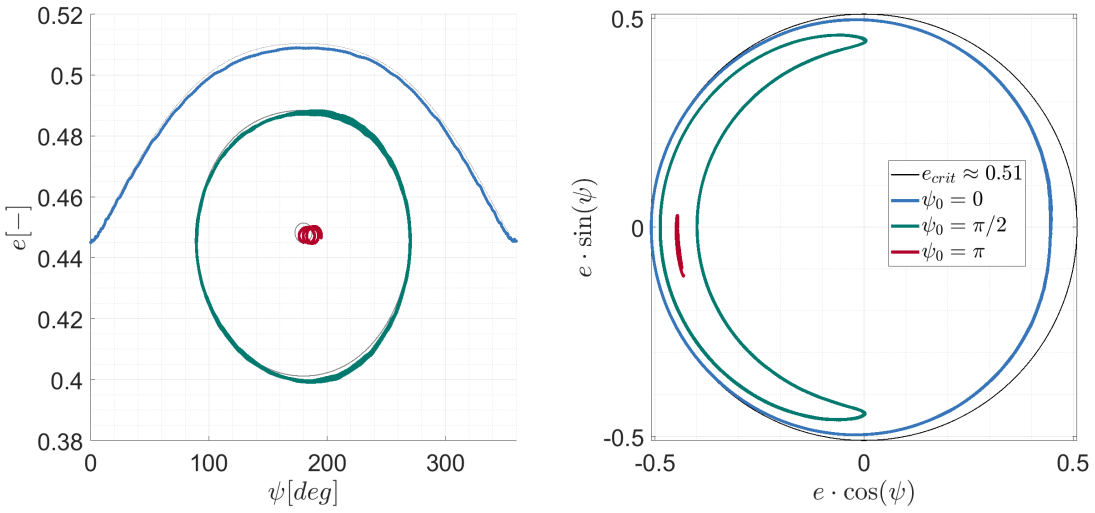

Figure 5.15: Representation in the plane (e, ψ) and in the Poincare plane ($e\cos\psi, e\sin\psi$) of the trajectories propagated with the Hamiltonian propagator (light gray) and semi-analytical propagator (coloured lines) for AMR = 0.5 m^2/kg, a = 12078 km and $i_{e=0}$ = 25.5°.

From this preliminary analysis, it is possible to conclude that, if a debris having AMR $< \sigma^*_{i,j}$ is propagated from $\psi = \pi$ or from an *asymmetric* equilibrium, it orbits evolve around the asymmetric point. Theredore, the debris remains trapped in that region of space.

5.4.2. NASA breakup model

In this part, the NASA breakup model formulation is presented, following what is described in Johnson et al. [67], Bade et al. [66] and Strasbery et al. [97].
In the standard NASA breakup model, the characteristic length, L_c, is used as independent variable to define the features of the fragmentation cloud. The properties of the generated fragments (i.e., mass, AMR, velocity variation) are taken from suitably built L_c-dependent distribution functions; hence, they are different for fragments with the same characteristic length. For this reason, at each run, the NASA breakup model provides different results for the same initial conditions. Different expressions are used for explosions and collisions, in order to take into account the dependence on the nature of the fragmentation event. While collisions tend to generate a considerable number of small fragments with high relative velocities, explosions usually generate larger fragments with lower speed. The model also allows distinguishing between catastrophic and non-catastrophic collisions. Here, a catastrophic collision is considered for values of the impact energy per target mass exceeding 40 J/g, since, under these conditions, the collision is

assumed to cause the complete fragmentation of both the impactor and the target (Bade et al. [66]). According to the implementation in Bade et al. [66], the number of produced fragments, N_f, of a given size L_c or larger can be computed through Equation (5.24), depending on the nature of the considered fragmentation event. For the scope of this thesis, only fragmentation due to explosion is considered (Bade et al. [66]):

$$N_f = 6SL_c[m]^{1.6}, \tag{5.24}$$

with S an empirically derived unitless factor between 0.1 and 1 (dependent on the explosive body type) and the reference mass of the collision. The AMR distribution is modelled as a *lognormal* distribution function, with mean value μ_{AMR} m^2/kg and standard deviation σ_{AMR} m^2/kg. Expressions for these parameters can be found in the cited literature such as Strasbery et al. [97], Krisko [66] and Johnson et al. [67]. The magnitude of the velocity variation, Δv, is defined as a function of the AMR and, similarly, its distribution is modelled as a *lognormal* distribution function. Again, the expressions for the mean value $\mu_{\Delta v}$ km/s and the standard deviation $\sigma_{\Delta v}$ km/s are included in the literature used.

Synthetic population

In this work, the synthetic population used for analysis is generated by the explosion of a spacecraft, which generates a population comprised of 100 evenly spaced bins on a logarithmic scale ranging from 1 mm to 10 cm. The parameter S has been chosen equal to $S = 0.002$ in order to limit the population to 10726 elements. The number of fragments N_f vs L_c and the distribution of AMR_{SC} and Δv_{SC} are reported in Figure 5.16.

5.4.3. Results discussion

Combining the NASA standard breakup model with the dynamical mapping and utilizing the extended Hamiltonian model (see Casanova et al. [51]), some test cases are analysed to provide deeper insight in the debris dynamics.
For all the tests described later, the final propagated debris population shown has been selected as those debris which are at:

- $a_{\text{deb}} \in [a_0 - 100 \text{ km}; , a_0 + 100 \text{ km}]$;
- $i_{\text{deb}} \in [i_0 - 0.05 \text{ deg}, i_0 + 0.05 \text{ deg}]$;
- $\text{AMR} < \sigma^*_{1,1}(a_0, i_0, e^{eq}_{1,1})$.

This has been done in order to compare the debris population with a "mean" phase space

having as Keplerian parameters the mean value of the filtered population parameters (final population of 1086 elements).

Figure 5.18 shows the propagated population which was propagated (from 21/03/2020 00:01 UTC to 21/03/2120) including all the perturbation listed in Appendix A and with AMR depending on the Standard NASA Breakup Model. The initial conditions of the population before the fragmentation was characterised by $a = 13000$ km, $e = 0.438671$, $i = 19.4074°$, $\Omega = 0°$, $f = 0°$ and $\omega = 0, \pi/2$ and π respectively. With reference to Figure 5.12, the spacecraft has been virtually exploded at the center of each resonance branch, and it has been evaluated how it evolves under the effect of the dynamics detailed in the Appendix A and compare it with a representative phase space.

Since the initial $a = 13000$ km and the corresponding $i_{e=0} = 18.3886°$ are located in the dynamical region (II) of fig. 3.5, the equilibrium points $\psi = 0$ and π are unstable, instead, the asymmetric point in $\psi \in]\pi/2, \pi[$ is stable. Figure 5.17 reports the phase space used to determine the initial condition of the synthetic population.

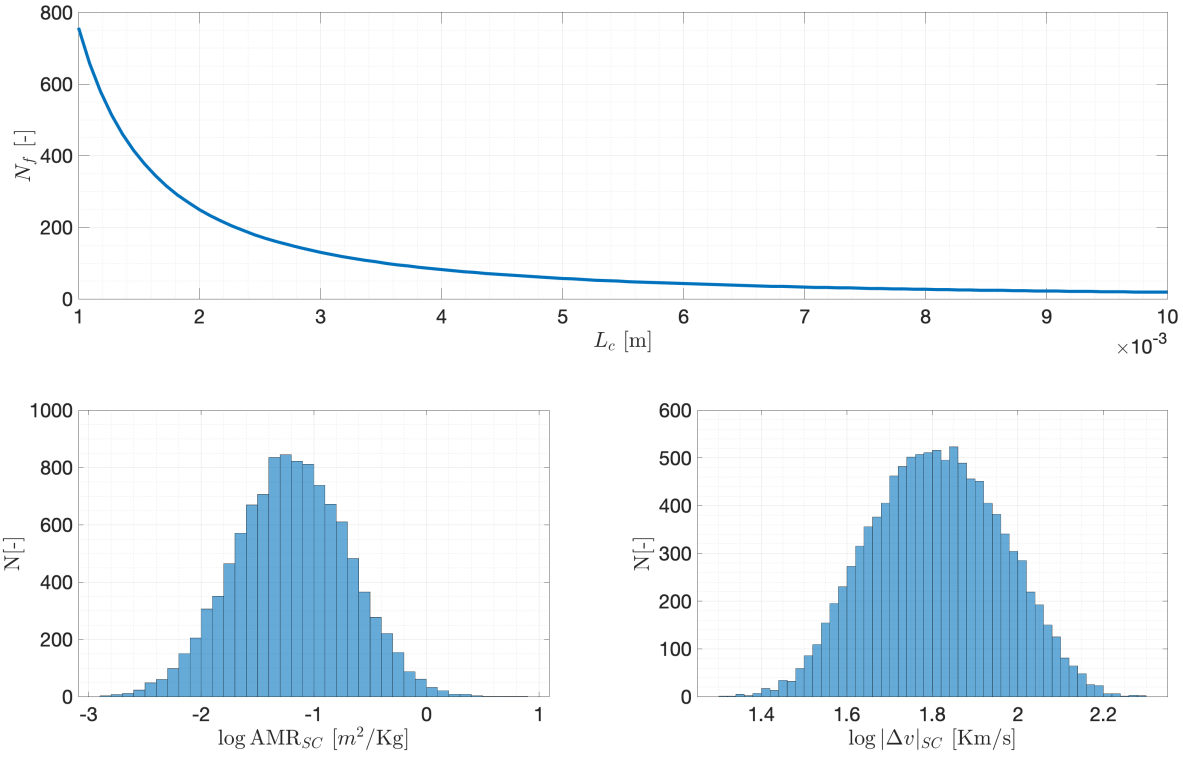

Figure 5.16: Up: number of fragment per characteristic length. Down: distribution of AMR and velocity variation among the fragments generated from the breakup.

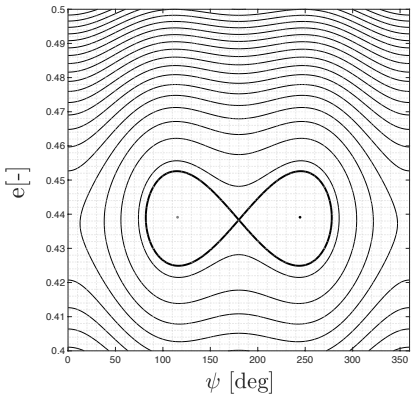

Figure 5.17: Reference phase space of the initial population generated at $a = 13000$ km, $i_{e=0} = 18.3886°$ and AMR $= 0.1\ m^2/\text{kg}$.

From the analysis of the case (2) of Figure 5.18 it is possible to conclude that if the fragmentation occurs near an stable stable point of the considered triplet (a, $i_{e=0}$, AMR), those some debris continue to librate around asymmetric stable points, instead, if the fragmentation occurs near unstable points (1) and (3) this does not take place.
Considering again the dynamical mapping in Figure 5.12 and in particular the resonance branch of the second plot with $\psi_0 = \pi/2$, in Figure 5.19, the propagated the fragments from an explosion which occurs in three peculiar points are reported. The points in which the fragmentation occurs are selected in the center and boundaries of the resonant route (see the first image of Figure 5.19). In the plots from (1) to (3) it is shown the comparison between propagated debris population and their reference phase space. The point (2) is once again the stable asymmetric point, while the other coincides with an initial point on a librating orbit around it in the phase space. As a consequence, they do not accumulate in a particular region.

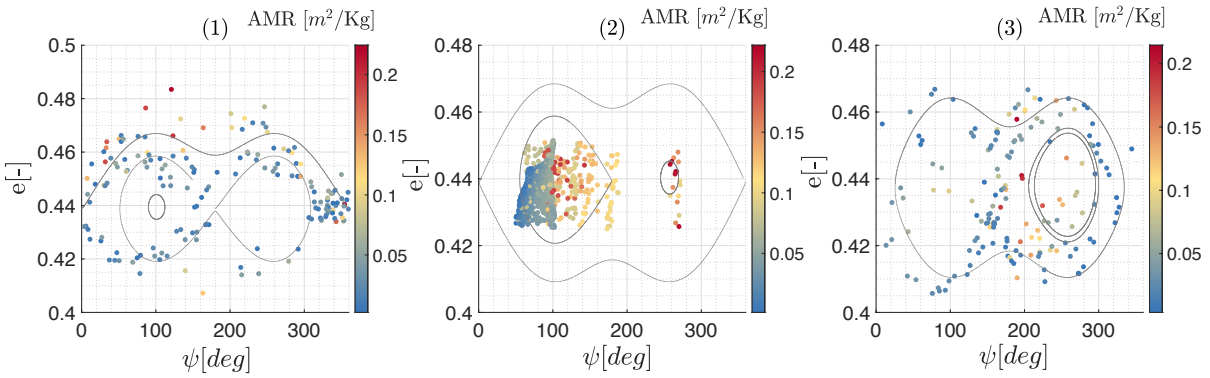

Figure 5.18: (1), (2) and (3): propagated population for 100 years from $\psi = 0$, $\psi = \pi/2$ and $\psi = \pi$ respectively, compared with a reference phase space.

As concluding notes, regarding the debris that are out of the filtering done to generate the previous plots, we can say that:

- due to the semi-major axis increase after the explosion, some of them may re-entered into the atmosphere;
- other objects with a different AMR may have been entangled at other equilibrium points positioned on various planes and semi-major axes.

To summarise, the initial condition under which a cloud of debris remains trapped in a stable point of the extended SRP-J_2-Sun model is such as it is generated near a stable point relative to the triplet (a, $i_{e=0}$, AMR). The explosion generates debris surrounding the initial point, but if it occurs near a stable point, the debris with AMR $< \sigma^*_{1,j}$ has a greater probability of remaining inside the stable point. Whether AMR $\geq \sigma^*_{1,j}$, the asymmetric equilibrium point with respect to (a, $i_{e=0}$, AMR) have collapsed to $\psi = \pi$, therefore the debris may have been entangled at stable point in $\psi = 0$ or $\psi = \pi$ depending on the dynamical area represented in Figure 3.5.

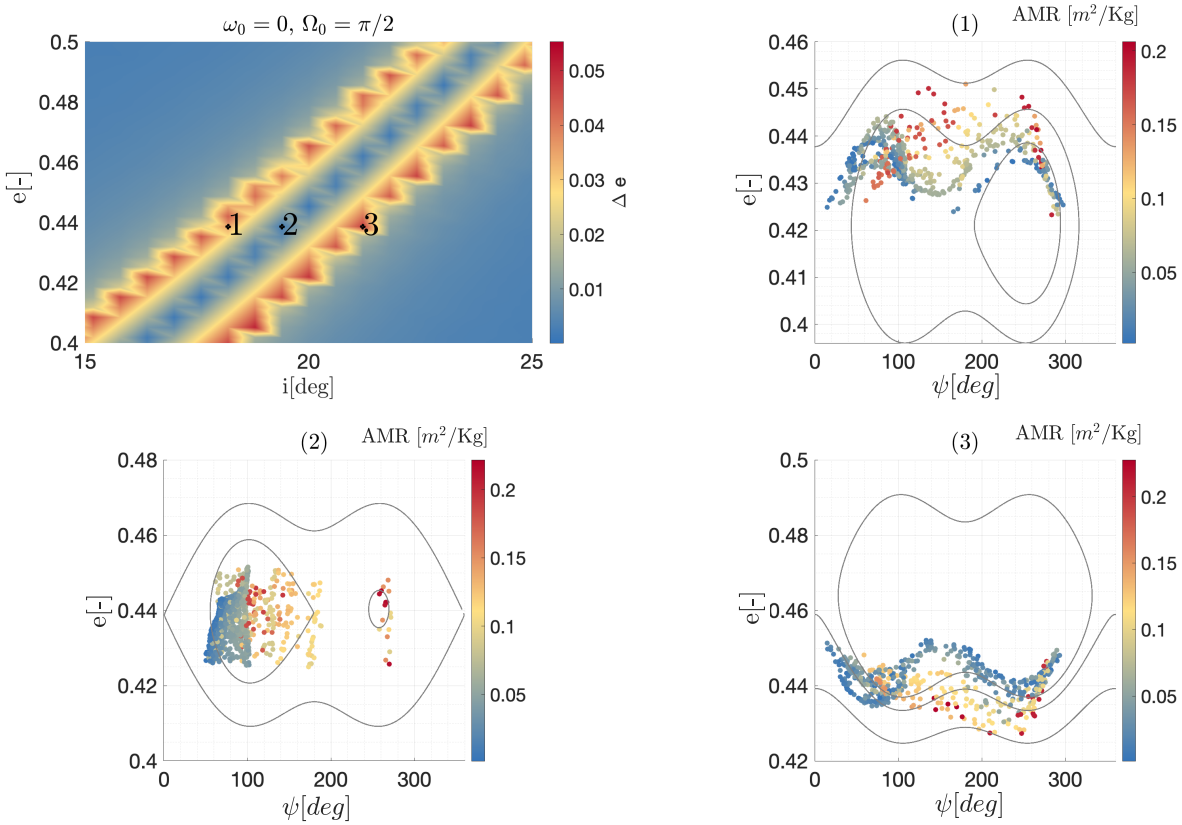

Figure 5.19: Cartography in the plane (e, i) used as initial condition for the synthetic population.(1), (2) and (3): propagated population for 100 years compared with a reference phase space.

6 | Conclusions and future works

At the conclusion of this work, it is possible to summarise the results obtained and track future research. During this research thesis, an Hamiltonian model capable of representing in a easy way as the one present in literature, the complex dynamics of low and medium AMR objects subject to the coupled SRP-Earth oblateness-Sun gravity perturbations, has been derived. Under the assumption of single resonance dynamics, and utilizing classical system theory tools, it was possible to analyse the dynamics of the extended model, and new dynamical properties that the actual model cannot capture were discovered. For example, in addition to the symmetric equilibrium points of the state-of-art model, the extended model introduces some asymmetric equilibria, which position depends on the AMR of the object. The model has been validated against a semi-analytical propagator, showing that the accuracy reduction is due to the fact that the semi-analytical propagator includes higher order terms and multiple-resonance interactions.

Despite that, the model is able to catch the main characteristics of the dynamics, almost analytically. Moreover, the integration of the model is an order of magnitude faster than the analytical one.

Then, the new phase space shape deriving from the extended model was exploited for the passive de-orbiting of dead spacecrafts. In particular, the de-orbit trajectory is designed such as it happens at these new equilibrium point. The minimum AMR computed from this strategy is, in some cases, lower than the one compute in literature, due to the fact that the strategy exploits also the effect of the Sun gravity. Two de-orbiting strategies were proposed. The first, starts from an initially circular orbit, and needs lower AMR in the cases when the de-orbiting starts from points near the bifurcation region or from points in the dynamical regions (II) and (III).

The second strategy, instead, starts from an unstable equilibrium point in $\psi = \pi$. In particular, it utilises the lowering of AMR to de-orbit rather than augmenting it. In fact, the solar sail remains open throughout the duration of the mission, and closes to ensure the de-orbiting.

Using the new phase space, it is almost possible to derive the conditions under which low/medium AMR debris accumulates in space. In particular, objects with an AMR

lower than a "discriminant" AMR, whose initial conditions are close to an asymmetric equilibrium point, could accumulate in it for an extended period of time. At the end, the theoretical assumptions are verified with the use of a synthetic population generated from the NASA standard breakup model, and propagated using a semi-analytical propagator. Although many interesting results have been obtained, there is still a long road ahead. Future researches may concentrate on:

- the dynamical analysis: the remaining five resonances of the extended Hamiltonian model have to be fully characterised, both in terms of bifurcation diagrams and bifurcation maps. This thesis has only given the general procedure that has to be followed to complete the analysis. Moreover, it could be interesting to study what happens when two or more resonances overlap-
- the mission design: the ability to modify the location of equilibrium by changing the AMR of the object may be used to plan an Earth observation mission based on an adaptive Solar Sails technology that, by varying the AMR, may change the mission working point;
- the debris dynamics: the theoretical results obtained from the merging of the Standard NASA Breakup model with the dynamical analysis of the Hamiltonian model should be compared with real data regarding low/medium AMR debris to prove what stated in the thesis.

A | Orbits Propagation Models

A.1. Order of magnitude of perturbations

According to Montenbruck and Eberhard [84], the equations used to characterised the order of magnitude of the perturbing acceleration as function of the altitude and AMR are the following:

$$\begin{aligned} a_{nm} &= (n+1)\frac{\mu_\oplus}{r^2}\frac{R_\oplus^n}{r^n}\sqrt{C_n^{m^2}+S_n^{m^2}}, \\ a_M &= \frac{2\mu_M}{d_M^3}r, \\ a_\odot &= \frac{2\mu_\odot}{d_\odot^3}r; \\ a_{SRP} &= C_R\frac{A}{m}P_\odot \end{aligned} \tag{A.1}$$

where $a_{nm}, a_M, a_\odot a_{SRP}$ are the perturbing acceleration due to gravitational non-uniformity, Moon gravity, Sun gravity and Solar Radiation Pressure respectively.

A.2. High fidelity Model

We consider a small body, say a space debris $\mathcal{S}$, subject to the gravitational attraction of the Earth, including the oblateness of our planet, the influence of the Moon, Sun and solar radiation pressure. In this work any other additional force that might affect the dynamics of the space debris are neglected, like Earth's atmosphere, solar wind, Poynting-Robertson effect (see Lhotka et al. [61] for detail).

Let $\vec{r}$ be the position of the object of mass m in a quasi-inertial, geocentric reference frame, $\vec{e} = (e_1, e_2, e_3)$, and denote by r_M, r_S the position vectors of the Moon, and the Sun, respectively. Then, the equation of motion of the is given by:

$$\frac{\mathrm{d}^2\boldsymbol{r}}{\mathrm{d}t^2} = -\frac{\mathrm{d}}{\mathrm{d}\boldsymbol{r}}[V_\mathrm{E}(\boldsymbol{r}) + V_\mathrm{M}(\boldsymbol{r},\boldsymbol{r}_\mathrm{M}) + V_\mathrm{S}(\boldsymbol{r},\boldsymbol{r}_\mathrm{S}) + V_\mathrm{SRP}(\boldsymbol{r},\boldsymbol{r}_\mathrm{S})],$$

where V_{E}, V_{M}, V_{S} are the gravitational potentials of the Earth, the Moon, and the Sun, V_{SRP} is the potential of solar radiation pressure. Details about the description of each terms is reported below and are the same given by the authors in Lhotka et al. [61].

A.2.1. Gravitational field perturbation

The geopotential V_{E} is given in a synodic reference frame, with unit vectors $\vec{f} = (f_1, f_2, f_3)$, and rotating with the same angular velocity of the Earth:

$$\begin{aligned} V_{\mathrm{E}}(r,\phi,\lambda) &= \frac{\mathcal{G}m_{\mathrm{E}}}{r}\sum_{n=0}^{\infty}\left(\frac{R_{\mathrm{E}}}{r}\right)^n\sum_{m=0}^{n}P_{nm}(\sin\phi) \\ &\quad\times\left(C_{nm}\cos m\lambda + S_{nm}\sin m\lambda\right). \end{aligned}$$

Here r, ϕ, λ are Earth-fixed spherical coordinates (radius, co-latitude, and longitude with $\lambda = 0$ corresponding to the Greenwich mean meridian), and R_E, C_{nm}, S_{nm} are the mean equatorial radius of the Earth and the (not normalized) Stokes coefficients that enter the spherical expansion of the Earth's gravitational field up to degree n and order m. The quantities P_{nm} are the associated Legendre polynomials (in the geophysical sense, see Kaula [24]).

A.2.2. Solar radiation pressure perturbation

The solar radiation pressure term is considered acting like a potential disturbing term:

$$V_{\mathrm{SRP}}\left(\boldsymbol{r},\boldsymbol{r}_{\mathrm{S}}\right) = \beta\mathcal{G}m_{\mathrm{S}}\left(\frac{1}{|\boldsymbol{r}-\boldsymbol{r}_{\mathrm{S}}|}\right).$$

Here, β is the ratio of the magnitude of radiation force over solar gravitational attraction:

$$\beta = \frac{SQA}{c}\Big/\frac{\mathcal{G}mm_{\mathrm{S}}}{R^2} \simeq 7.6\times10^{-4}\,Q\,\frac{A\ (\mathrm{m}^2)}{m\ (\mathrm{kg})},$$

In the code, $\frac{A}{m}$ is intended as the Area-To-Mass ratio of the object and Q the spectrally averaged dimensionless efficiency factor for radiation pressure.

A.2.3. Three body perturbation

The gravitational potentials due to the third-body, point-mass like interactions take the form:

$$V_k\left(\boldsymbol{r}, \boldsymbol{r}_k\right) = \mathcal{G}m_k \left(\frac{1}{\|\boldsymbol{r} - \boldsymbol{r}_k\|} - \frac{\boldsymbol{r} \cdot \boldsymbol{r}_k}{r_k^3} \right),$$

where k is M (Moon) or S (Sun). The position of the two bodies is retrieved by the routine Spice [88].

A.3. Semi-analytical Model

The single-averaged theory for Earth's satellites has been extensively studied and presented in the literature. In Particular the dynamical system adopted in PlanODyn is presented and validated in Colombo et al. [72]. Here are report the equations taken from the Appendix in Gkolias et al. [69] necessary to reproduce the calculations discussed in the present manuscript. In the following formulas $\mu_\oplus$ is the gravitational parameter of the Earth, $R_\oplus$ is the equatorial mean radius of the Earth and $(a, e, i, \Omega, \omega, M)$ the classical orbital elements of the satellite.

A.3.1. Zonal harmonics

For the secular effect of the zonal harmonics it is taken into account the first-order averaged perturbations with respect to only J_2:

$$\bar{\mathcal{R}}_\oplus = \bar{\mathcal{R}}_{J_2} \tag{A.2}$$

which from Kaula [24] is:

$$\bar{\mathcal{R}_{J_2}} = \frac{R_\oplus^2 J_2 \mu_\oplus (3\cos(2i) + 1)}{8a^3(1-e^2)^{3/2}}. \tag{A.3}$$

A.3.2. Third-body perturbations

The third-body potential implemented in Gkolias and Colombo [69], Colombo [73], [72] is expanded in powers of the parallactic factor (a/r_b), where r_b is the geocentric distance of the perturber. Terms up to the fourth order $(\mathrm{P}_2, \mathrm{P}_3, \mathrm{P}_4)$ in the expansion are retained for both the Sun and the Moon. The ephemeris of the Moon are generated from the algorithm described in Simpson et al. [83] and the ephemeris of the Sun are generated

from the algorithms described in the Chapters 25 and 26 by Meeus [98].

A.3.3. Solar radiation pressure

The single-averaged contribution of the solar radiation pressure is implemented as in Colombo [72]:

$$\begin{aligned}\bar{\mathcal{R}}_{\mathrm{SRP}} =& \frac{3}{2} a e P_{\mathrm{SRP}} C_R \frac{A}{m} \left(cos(\varepsilon)\sin(\lambda_\odot)\cos(\omega)\sin(\Omega)\right. \\ &+ \cos(\varepsilon)\cos(i)\sin(\lambda_\odot)\sin(\omega)\cos(\Omega) + \sin(\varepsilon)\sin(i)\sin(\lambda_\odot)\sin(\omega) \\ &\left. - \cos(i)\cos(\lambda_\odot)\sin(\omega)\sin(\Omega) + \cos(\lambda_\odot)\cos(\omega)\cos(\Omega)\right),\end{aligned} \tag{A.4}$$

where $\lambda_\odot$ is the ecliptic longitude of the Sun, P_{SRP} is the solar radiation pressure per unit area at 1 AU, C_R the satellite's reflectivity coefficient and A/M its area-to-mass ratio.

A.3.4. Equations of motion

The complete long-term evolution is driven by the perturbing function (Gkolias and Colombo [69], Colombo [73], [72]):

$$\bar{\mathcal{R}} = \bar{\mathcal{R}}_\oplus + \bar{\mathcal{R}}_{\mathrm{3body}} + \bar{\mathcal{R}}_{\mathrm{SRP}}, \tag{A.5}$$

obtained under the assumption that the orbital elements are constant over one orbit revolution of the spacecraft around the central planet. The equations of motion in orbital elements are then derived via Lagrange's planetary equations (Gkolias and Colombo [69], Colombo [73], [72]):

$$\begin{aligned}\frac{\mathrm{d}a}{\mathrm{d}t} &= \frac{2}{na}\frac{\partial\bar{\mathcal{R}}}{\partial M}, \\ \frac{\mathrm{d}e}{\mathrm{d}t} &= \frac{1}{na^2e}\left((1-e^2)\frac{\partial\bar{\mathcal{R}}}{\partial M} - \sqrt{1-e^2}\frac{\partial\bar{\mathcal{R}}}{\partial\omega}\right), \\ \frac{\mathrm{d}i}{\mathrm{d}t} &= \frac{1}{na^2\sin i\sqrt{1-e^2}}\left(\cos i\frac{\partial\bar{\mathcal{R}}}{\partial\omega} - \frac{\partial\bar{\mathcal{R}}}{\partial\Omega}\right), \\ \frac{\mathrm{d}\Omega}{\mathrm{d}t} &= \frac{1}{na^2\sin i\sqrt{1-e^2}}\frac{\partial\bar{\mathcal{R}}}{\partial i}, \\ \frac{\mathrm{d}\omega}{\mathrm{d}t} &= -\frac{1}{na^2\sin i\sqrt{1-e^2}}\cos i\frac{\partial\bar{\mathcal{R}}}{\partial i} + \frac{\sqrt{1-e^2}}{na^2e}\frac{\partial\bar{\mathcal{R}}}{\partial e}, \\ \frac{\mathrm{d}M}{\mathrm{d}t} &= n - \frac{1-e^2}{na^2e}\frac{\partial\bar{\mathcal{R}}}{\partial e} - \frac{2}{na}\frac{\partial\bar{\mathcal{R}}}{\partial a}.\end{aligned} \tag{A.6}$$

Therefore, the variation of the mean elements is described by (Gkolias and Colombo [69], Colombo [73], [72]):

$$\frac{d\vec{\alpha}}{dt} = f\left(\vec{\alpha}, \frac{d\mathcal{R}}{dt}\right). \tag{A.7}$$

B | Hessian terms of the commensurability equation

The coefficients of the SRP and J_2 contributes have been taken from Alessi et al [14]. The Sun gravitational contributes are original.

Hessian term of commensurability equation of SRP-J_2

The differential contributes of to the commensurability equation of the SRP-J_2 model are (Alessi et al. [14]):

$$\begin{aligned}
\frac{\partial \dot{\Omega}_{(J_2,j)}}{\partial e} =& -6\frac{J_2 r_\oplus^2 ne}{a^2(1-e^2)^3}\cos i + \frac{C_{\mathrm{SRP}}}{na(1-e^2)^{3/2}\sin i}\frac{\partial \mathcal{T}_j}{\partial i}\cos\psi_j \\
&- \frac{J_2 r_\oplus^2 n}{a^2(1-e^2)^2}\frac{\partial \cos i}{\partial e} + C_{\mathrm{SRP}}\frac{e}{na\sqrt{1-e^2}}\frac{\partial \mathcal{T}_j}{\partial i}\cos\psi_j\frac{\partial}{\partial e}\frac{1}{\sin i} \\
&+ C_{\mathrm{SRP}}\frac{e}{na\sqrt{1-e^2}\sin i}\cos\psi_j\frac{\partial}{\partial e}\frac{\partial \mathcal{T}_j}{\partial i}, \\
\frac{\partial \dot{\omega}_{(J_2,j)}}{\partial e} =& 3\frac{J_2 r_\oplus^2 ne}{a^2(1-e^2)^3}(5\cos^2 i - 1) \\
&- \frac{C_{\mathrm{SRP}}}{na\sqrt{1-e^2}}\left(\frac{\mathcal{T}_j}{e^2} - \frac{\cos i}{(1-e^2)^2\sin i}\frac{\partial \mathcal{T}_j}{\partial i}\right)\cos\psi_j \\
&+ \frac{15}{2}\frac{J_2 r_\oplus^2 n\cos i}{a^2(1-e^2)^2}\frac{\partial \cos i}{\partial e} + C_{\mathrm{SRP}}\frac{\sqrt{1-e^2}}{nae}\cos\psi_j\frac{\partial \mathcal{T}_j}{\partial e} \\
&- C_{\mathrm{SRP}}\frac{e}{na\sqrt{1-e^2}}\frac{\partial \mathcal{T}_j}{\partial i}\cos\psi_j\frac{\partial}{\partial e}\frac{1}{\tan i} \\
&+ C_{\mathrm{SRP}}\frac{e}{na\sqrt{1-e^2}\tan i}\cos\psi_j\frac{\partial}{\partial e}\frac{\partial \mathcal{T}_j}{\partial i},
\end{aligned} \tag{B.1}$$

where:

$$\begin{aligned}\frac{\partial \cos i}{\partial e} =& \frac{e\Pi}{n_1\sqrt{\mu a}(1-e^2)^{3/2}},\\ \frac{\partial \sin i}{\partial e} =& \frac{1}{\tan i}\frac{\partial \cos i}{\partial e},\end{aligned} \tag{B.2}$$

and $\frac{\partial \mathcal{T}_j}{\partial i}$ and $\frac{\partial}{\partial e}\frac{\partial \mathcal{T}_j}{\partial i}$ can be derived by applying the half-angle trigonometric formulae.

Hessian term of commensurability equation of SRP-J_2-Sun

The differential contributes of to the commensurability equation of the SRP-J_2-Sun model are:

$$\begin{aligned}\frac{\partial \dot{\Omega}_{(J_2,j)}}{\partial e} =& -6\frac{J_2 r_\oplus^2 ne}{a^2(1-e^2)^3}\cos i + \frac{C_{\mathrm{SRP}}}{na(1-e^2)^{3/2}\sin i}\frac{\partial \mathcal{T}_j}{\partial i}\cos\psi_j\\ &- \frac{3}{2}\frac{J_2 r_\oplus^2 n}{a^2(1-e^2)^2}\frac{\partial \cos i}{\partial e} + C_{\mathrm{SRP}}\frac{e}{na\sqrt{1-e^2}}\frac{\partial \mathcal{T}_j}{\partial i}\cos\psi_j\frac{\partial}{\partial e}\frac{1}{\sin i}\\ &+ C_{\mathrm{SRP}}\frac{e}{na\sqrt{1-e^2}\sin i}\cos\psi_j\frac{\partial}{\partial e}\frac{\partial \mathcal{T}_j}{\partial i},\\ \frac{\partial \dot{\omega}_{(J_2,j)}}{\partial e} =& 3\frac{J_2 r_\oplus^2 ne}{a^2(1-e^2)^3}(5\cos^2 i - 1)\\ &- \frac{C_{\mathrm{SRP}}}{na\sqrt{1-e^2}}\left(\frac{\mathcal{T}_j}{e^2} - \frac{\cos i}{(1-e^2)^2\sin i}\frac{\partial \mathcal{T}_j}{\partial i}\right)\cos\psi_j\\ &+ \frac{15}{2}\frac{J_2 r_\oplus^2 n\cos i}{a^2(1-e^2)^2}\frac{\partial \cos i}{\partial e} + C_{\mathrm{SRP}}\frac{\sqrt{1-e^2}}{nae}\cos\psi_j\frac{\partial \mathcal{T}_j}{\partial e}\\ &- C_{\mathrm{SRP}}\frac{e}{na\sqrt{1-e^2}}\frac{\partial \mathcal{T}_j}{\partial i}\cos\psi_j\frac{\partial}{\partial e}\frac{1}{\tan i}\\ &+ C_{\mathrm{SRP}}\frac{e}{na\sqrt{1-e^2}\tan i}\cos\psi_j\frac{\partial}{\partial e}\frac{\partial \mathcal{T}_j}{\partial i}.\end{aligned} \tag{B.3}$$

The contribute to the stability of the Sun gravity is:

$$
\begin{aligned}
\frac{\partial \dot{\Omega}_{\odot_j}}{\partial e} =& -\frac{15}{32} e \frac{e^2-2}{(1-e^2)^{3/2}} \frac{n_1 n_\odot^2}{n} \csc i \frac{\partial \mathcal{K}_j}{\partial i} \cos 2\psi + \\
&+ \frac{15}{32} \frac{e^2}{\sqrt{1-e^2}} \frac{n_1 n_\odot^2}{n} \frac{\partial \mathcal{K}_j}{\partial i} \cos 2\psi_j \frac{\partial}{\partial e} \frac{1}{\sin i} + \\
&+ \frac{15}{32} \frac{e^2 \csc i}{\sqrt{1-e^2}} \frac{n_1 n_\odot^2}{n} \frac{\partial}{\partial e} \frac{\partial \mathcal{K}_j}{\partial i} \cos 2\psi_j, \\
\frac{\partial \dot{\omega}_{\odot_j}}{\partial e} =& \frac{15}{32} \frac{e}{(1-e^2)^{3/2}} \frac{n_\odot^2}{n} \left[2(e^2-1)\mathcal{K}_j + (e^2-2) \frac{\partial \mathcal{K}_j}{\partial i} \cot i \right] + \\
&+ \frac{15}{16} \frac{n_\odot^2}{n} \sqrt{1-e^2} \frac{\partial}{\partial e} \mathcal{K}_j \cos 2\psi_j + \\
&- \frac{15}{32} \frac{e^2}{\sqrt{1-e^2}} \frac{n_1 n_\odot^2}{n} \frac{\partial \mathcal{K}_j}{\partial i} \cos 2\psi_j \frac{\partial}{\partial e} \frac{1}{\tan i} + \\
&- \frac{15}{32} \frac{e^2}{\sqrt{1-e^2}} \frac{n_1 n_\odot^2}{n} \frac{1}{\tan i} \frac{\partial}{\partial e} \frac{\partial \mathcal{K}_j}{\partial i} \cos 2\psi_j
\end{aligned}
\tag{B.4}
$$

where (Alessi et al. [14]):

$$
\begin{aligned}
\frac{\partial \cos i}{\partial e} =& \frac{e\Pi}{n_1 \sqrt{\mu a}(1-e^2)^{3/2}}, \\
\frac{\partial \sin i}{\partial e} =& \frac{1}{\tan i} \frac{\partial \cos i}{\partial e}, \quad \frac{\partial \csc i}{\partial e} = \quad -\frac{1}{\sin i^2} \frac{\partial \sin i}{\partial e}
\end{aligned}
\tag{B.5}
$$

and $\frac{\partial \mathcal{T}_j}{\partial i}$, $\frac{\partial}{\partial e}\frac{\partial \mathcal{T}_j}{\partial i}$ and $\frac{\partial \mathcal{K}_j}{\partial i}$ can be derived by applying the half-angle trigonometric formulae.

C | Second integral of Motion derivation

We want to focus the attention on the derivation of the second integral of motion equation. Let us consider the equation of motion of the eccentricity and inclination from eq. (3.23), and divide the first by the second under the hypotheses of isolated resonance (the contrary holds the same, Alessi et al. [14]):

$$\frac{\mathrm{d}i}{\mathrm{d}e} = \frac{e\sin i}{1-e^2}\frac{\frac{\partial\cos\psi_j}{\partial\Omega} - \cos i\frac{\partial\cos\psi_j}{\partial\omega}}{\frac{\partial\cos\psi_j}{\partial\omega}} = \frac{e\sin i}{1-e^2}\left(\frac{\partial\cos\psi_j/\partial\Omega}{\partial\cos\psi_j/\partial\omega} - \cos i\right), \tag{C.1}$$

which, whit the adopted convention by Gkolias et al. [69], it reads:

$$\frac{\mathrm{d}i}{\mathrm{d}e} = \frac{e\sin i}{1-e^2}\left(\frac{n_2}{n_1} - \cos i\right). \tag{C.2}$$

The above differential can be exactly solved by the method of separation of variables and integrated from $e = 0$ and e and from $i_{e=0}$ and i:

$$\int_{i_0}^{i} \frac{\frac{n_2}{n_1} - \cos i}{\sin i}\mathrm{d}i = \int_{e=0}^{e} \frac{1-e^2}{e}\mathrm{d}e \tag{C.3}$$

which is:

$$\ln\left(-n_2 + n_1\cos i\right) - \ln\left(-n_2 + n_1\cos i_{e=0}\right) = -\frac{1}{2}\ln\left(1-e^2\right) \tag{C.4}$$

bringing on the left the quantity related to the final state and elevating:

$$\sqrt{1-e^2}(n_2 - n_1\cos i) = (n_2 - n_1\cos i_{e=0}), \tag{C.5}$$

which is nothing but the a-dimensional version of the Π in eq. (3.17), which is multiplied by $\sqrt{\mu a}$ to have the unit of a momentum. From eq. (C.5) we can also note that the integral of motion is constant once the resonance has been chosen since a is constant due to the conservative nature of the acting forces.

In conclusion, the eq. (C.1) can be generalised with the perturbing function or equivalently the disturbing Hamiltonian $\mathcal{R} = -\mathcal{H}$:

$$\frac{\mathrm{d}i}{\mathrm{d}e} = \frac{e \sin i}{1 - e^2} \left(\frac{\partial \mathcal{R} / \partial \Omega}{\partial \mathcal{R} / \partial \omega} - \cos i \right), \tag{C.6}$$

The eq. (C.6) has also been derived by Giovannini in [79].

D | Commensurability equation coefficients

The coefficients for the J_2 and SRP contributes are taken from Alessi et al. [14].

Resonance $j = 2$

Table D.1: Coefficients of the quadratic equation $c_1 \cos^2 i + c_2 \cos i + c_3 = 0$ associated to the extended model for **j=2**. In the table, $\beta = \sqrt{1-e^2}$, $\gamma = \cos^2\left(\frac{\epsilon}{2}\right)$, $\rho = \sin^2\left(\frac{\epsilon}{2}\right)$. Note that eq. (4.34) is multiplied by $16a^5\beta^5 en$.

Effect	c_1	c_2	c_3
J_2	$-60C_\oplus e\beta$	$-24C_\oplus e\beta$	$+4e\beta\,(3C_\oplus - 4a^5\beta^4 n n_\odot)$
SRP		$+8C_{\mathrm{SRP}}a^4\beta^4\gamma\cos\psi$	$-8C_{\mathrm{SRP}}a^4\beta^4\gamma(1-2e^2)\cos\psi$
$\odot$	$+15a^5\gamma^2 e\beta^4 n_\odot^2\cos 2\psi$	$-30a^5\gamma^2 e\beta^4 n_\odot^2\cos 2\psi$	$+15a^5\gamma^2 e\beta^4(2e^2-1)n_\odot^2\cos 2\psi$

Resonance $j = 3, 4$

According to Gkolias et al. [69], the coefficient n_2 relative to the RAAN (Ω) is null. The contribute of the Sun gravity on the variation of the argument of perigee is:

$$\dot{\omega}_\odot = \left[-\frac{15}{8}a^5\beta^4 e n_\odot^2 \chi(e^2+\beta^2)\sin i^2 + \frac{15}{8}a^5\beta^4 e^2 n_\odot^2\chi \right]\cos 2\psi_3, \tag{D.1}$$

with $\chi = \cos\varepsilon^2 - 2\sin\varepsilon^2 - 1$.

In order to have the same nomenclature as in the other example, the eq. (D.2) has to be multiplied by $\sin i/(15\mathcal{C}_\oplus e\beta)$:

$$\dot{\omega}_\odot = \left[-\frac{1}{8\mathcal{C}_\oplus}a^5\beta^3 n_\odot^2\chi(e^2+\beta^2)\sin i^3 + \frac{1}{8\mathcal{C}_\oplus}a^5\beta^3 e n_\odot^2\chi\sin i \right]\cos 2\psi_{3,4}, \tag{D.2}$$

Table D.2: Coefficients of the quadratic equation $s_0 \sin i^3 + s_1 \sin i^2 + s_2 \sin i + s_3 = 0$ associated with the equilibrium point at ψ_j for **j=3,4**. In the table, $\beta = \sqrt{1-e^2}$, $\gamma = \cos^2\left(\frac{\epsilon}{2}\right)$, $\rho = \sin^2\left(\frac{\epsilon}{2}\right)$. Note that eq. (4.34) is multiplied by $16a^5\beta^5 en$.

j	s_1	s_2	s_3
3	$-\frac{2C_{\mathrm{SRP}}}{15C_\oplus e}a^4\beta^3 \sin\epsilon\cos\psi$	$-\frac{4}{15C_\oplus}\left(3C_\oplus - a^5\beta^4 n n_s\right)$ $+\frac{1}{8\mathcal{C}_\oplus}a^5\beta^3 e n_\odot^2 \chi \sin i \cos\psi$	$\frac{2C_{\mathrm{SRP}}}{15C_\oplus}ea^4\beta^3 \sin\epsilon\cos\psi$
4	$\frac{2C_{\mathrm{SRP}}}{15C_\oplus e}a^4\beta^3 \sin\epsilon\cos\psi$	$-\frac{4}{15C_\oplus}\left(3C_\oplus + a^5\beta^4 n n_s\right)$ $+\frac{1}{8\mathcal{C}_\oplus}a^5\beta^3 e n_\odot^2 \chi \sin i \cos\psi$	$-\frac{2C_{\mathrm{SRP}}}{15C_\oplus}ea^4\beta^3 \sin\epsilon\cos\psi$

and $s_0 = -\frac{1}{8\mathcal{C}_\oplus}a^5\beta^3 n_\odot^2 \chi (e^2+\beta^2)\sin i^3 \cos\psi$.

Resonance $j = 5$

Table D.3: Coefficients of the quadratic equation $c_1 \cos^2 i + c_2 \cos i + c_3 = 0$ associated to the extended model for **j=5**. In the table, $\beta = \sqrt{1-e^2}$, $\gamma = \cos^2\left(\frac{\epsilon}{2}\right)$, $\rho = \sin^2\left(\frac{\epsilon}{2}\right)$.

Effect	c_1	c_2	c_3
J_2	$60C_\oplus e\beta$	$-24C_\oplus e\beta$	$-4e\beta\left(3C_\oplus - 4a^5\beta^4 n n_\odot\right)$
SRP		$+8C_{\mathrm{SRP}}a^4\beta^4\rho\cos\psi$	$+8C_{\mathrm{SRP}}a^4\beta^4\rho(1-2e^2)\cos\psi$
$\odot$	$+15a^5\rho^2 e\beta^4 n_\odot^2 \cos 2\psi$	$+30a^5\rho^2 e\beta^6 n_\odot^2 \cos 2\psi$	$-15a^5\rho^2 e\beta^4(2e^2-1)n_\odot^2 \cos 2\psi$

Resonance $j = 6$

Table D.4: Coefficients of the quadratic equation $c_1 \cos^2 i + c_2 \cos i + c_3 = 0$ associated to the extended model for **j=6**. In the table, $\beta = \sqrt{1-e^2}$, $\gamma = \cos^2\left(\frac{\epsilon}{2}\right)$, $\rho = \sin^2\left(\frac{\epsilon}{2}\right)$.

Effect	c_1	c_2	c_3
J_2	$-60C_\oplus e\beta$	$-24C_\oplus e\beta$	$+4e\beta\left(3C_\oplus + 4a^5\beta^4 n n_\odot\right)$
SRP		$+8C_{\mathrm{SRP}}a^4\beta^4\rho\cos\psi$	$-8C_{\mathrm{SRP}}a^4\beta^4\rho(1-2e^2)\cos\psi$
$\odot$	$+15a^5\rho^2 e\beta^4 n_\odot^2 \cos 2\psi$	$-30a^5\rho^2 e\beta^4 n_\odot^2 \cos 2\psi$	$+15a^5\rho^2 e\beta^4(2e^2-1)n_\odot^2 \cos 2\psi$

Bibliography

[1] J.-C Liou and J K Weaver. "Orbital dynamics of High Area Mass Ratio debris and their distribution in the geosynchronous region". In: *4th European Conference on Space Debris (ESA SP-587). 18-20 April 2005*. D. Danesy, Aug. 2005. URL: https://ui.adsabs.harvard.edu/abs/2005ESASP.587..285L.

[2] Anselmo L. and Pardini C. "Orbital evolution of geosynchronous objects with high area-to-mass ratios". In: *4th European Conference on Space Debris, pp. 279–284, Darmstadt, Germany, 18-20 April 2005*. 2005. DOI: 10.1016/j.asr.2007.02.03.

[3] S. Valk, A. Lemaître, and F. Deleflie. "Semi-analytical theory of mean orbital motion for geosynchronous space debris under gravitational influence". In: *Advances in Space Research* 43 (7 Apr. 2009), pp. 1070–1082. ISSN: 02731177. DOI: 10.1016/j.asr.2008.12.015.

[4] A. Lemaître, N. Delsate, and S. Valk. "A web of secondary resonances for large A/m geostationary debris". In: *Celestial Mechanics and Dynamical Astronomy* 104 (Aug. 2009), pp. 383–402. DOI: 10.1007/s10569-009-9217-2.

[5] Aaron J. Rosengren and Daniel J. Scheeres. "Prediction of HAMR Debris Population Distribution Released from GEO Space". In: *Proceedings of the Advanced Maui Optical and Space Surveillance Technologies Conference, held in Wailea, Maui, Hawaii, September 11-14, 2012, Ed.: S. Ryan, The Maui Economic Development Board, id.11*. 2012. URL: https://ui.adsabs.harvard.edu/abs/2012amos.confE..11R.

[6] T. Schildknecht, R. Musci, and Tim Flohrer. "Properties of the high area-to-mass ratio space debris population at high altitudes". In: *Advances in Space Research* 41 (Dec. 2008), pp. 1039–1045. DOI: 10.1016/j.asr.2007.01.045.

[7] Sven Flegel. "Multi-Layer Insulation as Contribution to Orbital Debris". en. PhD thesis. Dec. 2013. DOI: 10.24355/dbbs.084-201409150901-0. URL: https://doi.org/10.24355/dbbs.084-201409150901-0.

[8] G. Drolshagen, T. Nehls, and R. Noomen. "The small size debris population in the GEO belt". In: *5th European Conference on Space Debris Darmstadt, Germany - Noordwijk Duration: 30 Mar 2009 - 2 Apr 2009*. ESA/ ESTEC. URL: https://ntrs.nasa.gov/citations/20170003811.

[9] W.D. McClain and D.A. Vallado. *Fundamentals of Astrodynamics and Applications*. Space Technology Library. Springer Netherlands, 2001. ISBN: 9780792369035. URL: https://books.google.it/books?id=PJLlWzMBKjkC.

[10] R.H. Battin. *An Introduction to the Mathematics and Methods of Astrodynamics*. AIAA education series. American Institute of Aeronautics and Astronautics, 1999. ISBN: 9781563473425. DOI: 10.2514/5.9781600861543.0000.0000. URL: https://books.google.it/books?id=vxaxngEACAAJ.

[11] Howard D. Curtis. "Chapter 10 - Introduction to orbital perturbations". In: *Orbital Mechanics for Engineering Students (Fourth Edition)*. Ed. by Howard D. Curtis. Fourth Edition. Aerospace Engineering. Butterworth-Heinemann, 2020, pp. 1–54. ISBN: 978-0-08-102133-0. DOI: https://doi.org/10.1016/B978-0-08-102133-0.00001-5. URL: https://www.sciencedirect.com/science/article/pii/B9780081021330000015.

[12] A. Krivov and Juan Getino. "Orbital evolution of high-altitude balloon satellites". In: *Astronomy and Astrophysics* 318 (Jan. 1997), pp. 308–314. URL: https://ui.adsabs.harvard.edu/abs/1997A&26A...318..308K.

[13] Charlotte Lcking, Camilla Colombo, and Colin R McInnes. "A passive satellite deorbiting strategy for medium earth orbit using solar radiation pressure and the J2 effect". In: *Acta Astronautica* 77 (2012), pp. 197–206. DOI: 10.1016/j.actaastro.2012.03.026.

[14] Elisa Maria Alessi, Camilla Colombo, and Alessandro Rossi. "Phase space description of the dynamics due to the coupled effect of the planetary oblateness and the solar radiation pressure perturbations". In: *Celestial Mechanics and Dynamical Astronomy* 131 (Sept. 2019). DOI: 10.1007/s10569-019-9919-z.

[15] Ioannis Gkolias, Elisa Maria Alessi, and Camilla Colombo. "Dynamical taxonomy of the coupled solar radiation pressure and oblateness problem and analytical deorbiting configurations". In: *Celestial Mechanics and Dynamical Astronomy* 132.11-12 (Nov. 2020). DOI: 10.1007/s10569-020-09992-2. URL: https://doi.org/10.1007/s10569-020-09992-2.

[16] P. Musen, R. Bryant, and A. Bailie. "Perturbations in perigee height of Vanguard I". In: *Science* 131.3404 (1960), pp. 935–936. DOI: 10.1126/science.131.3404.935.

[17] Irwin I. Shapiro and Harrison M. Jones. "Perturbations of the Orbit of the Echo Balloon". In: *Science* 132.3438 (1960), pp. 1484–1486. ISSN: 00368075, 10959203. URL: http://www.jstor.org/stable/1707154.

[18] Peter Musen. "The influence of the solar radiation pressure on the motion of an artificial satellite". In: *Journal of Geophysical Research* 65.5 (1960), pp. 1391–1396. DOI: 10.1029/JZ065i005p01391.

[19] W.J. Boulton. "The effect of solar radiation pressure on the orbit of a cylindrical satellite". In: *Planetary and Space Science* 32.3 (1984), pp. 287–296. ISSN: 0032-0633. DOI: 10.1016/0032-0633(84)90164-8. URL: https://www.sciencedirect.com/science/article/pii/0032063384901648.

[20] F Mignard and M Henon. "About an unsuspected integrable problem". In: *Celestial mechanics* 33.3 (1984), pp. 239–250. DOI: 10.1007/BF01230506.

[21] Teppei Oyama, Hiroshi Yamakawa, and Yoshiharu Omura. "Orbital Dynamics of Solar Sails for Geomagnetic Tail Exploration". In: *Journal of Spacecraft and Rockets* 45 (Mar. 2008). DOI: 10.2514/1.31274.

[22] Daniel Jay Scheeres. "Orbit mechanics about asteroids and comets". In: *Journal of Guidance, Control, and Dynamics* 35.3 (2012), pp. 987–997. DOI: 10.2514/1.57247.

[23] G. E. Cook. "Luni-Solar Perturbations of the Orbit of an Earth Satellite". In: *Geophysical Journal International* 6.3 (Apr. 1962), pp. 271–291. ISSN: 0956-540X. DOI: 10.1111/j.1365-246X.1962.tb00351.x. eprint: https://academic.oup.com/gji/article-pdf/6/3/271/1832732/6-3-271.pdf. URL: https://doi.org/10.1111/j.1365-246X.1962.tb00351.x.

[24] William M Kaula. *Theory of Satellite Geodesy: Applications of Satellites to Geodesy*. Blaisdell Publishing Company, 1966. ISBN: 9780486414652.

[25] Francois Mignard. "Radiation pressure and dust particle dynamics". In: *Icarus* 49.3 (1982), pp. 347–366. ISSN: 0019-1035. DOI: https://doi.org/10.1016/0019-1035(82)90041-0. URL: https://www.sciencedirect.com/science/article/pii/0019103582900410.

[26] Camilla Colombo, Charlotte Bewick, and Colin McInnes. "Orbital dynamics of high area-to-mass ratio spacecraft with J2 and solar radiation pressure for novel Earth observation and communication services". In: *Acta Astronautica* 81 (Dec. 2012), pp. 137–150. DOI: 10.1016/j.actaastro.2012.07.009.

[27] Camilla Colombo and Colin McInnes. "Orbital Dynamics of Smart-Dust Devices with Solar Radiation Pressure and Drag". In: *Journal of Guidance, Control, and Dynamics* 34 (Nov. 2011), pp. 1613–1631. DOI: 10.2514/1.52140.

[28] Camilla Colombo, Charlotte Lücking, and Colin R McInnes. "Orbital dynamics of high area-to-mass ratio spacecraft with J2 and solar radiation pressure for novel Earth observation and communication services". In: *Acta Astronautica* 81.1 (2012), pp. 137–150. ISSN: 0094-5765. DOI: https://doi.org/10.1016/j.actaastro.2012.07.009. URL: https://www.sciencedirect.com/science/article/pii/S009457651200272X.

[29] Daniel Casanova, Alexis Petit, and A. Lemaître. "Long-term evolution of space debris under the J_2 effect, the solar radiation pressure and the solar and lunar

perturbations". In: *Celestial Mechanics and Dynamical Astronomy* 123 (Aug. 2015). DOI: 10.1007/s10569-015-9644-1.

[30] Jerome Daquin et al. "The dynamical structure of the MEO region: long-term stability, chaos, and transport". In: *Celestial Mechanics and Dynamical Astronomy* 124 (Apr. 2016). DOI: 10.1007/s10569-015-9665-9.

[31] Elisa Maria Alessi and Camilla Colombo. "Dynamical System Description of the Solar Radiation Pressure and J_2 Phase Space for End-Of-life Design and Frozen Orbit Design". In: *69th International Astronautical Congress, Bremen, Germany, 01-05/1/2018*. URL: https://re.public.polimi.it/retrieve/handle/11311/1066710/318984/ALESE01-18.pdf.

[32] Tong Luo, Xu Ming, and Camilla Colombo. "Heliotropic frozen orbits design for high area-to-mass ratio spacecraft". In: *Journal of Astronomical Telescopes, Instruments, and Systems* 5 (Sept. 2019), p. 1. DOI: 10.1117/1.JATIS.5.3.036003.

[33] Ch. Hubaux and A. Lemaître. "The impact of Earth's shadow on the long-term evolution of space debris". In: *Celestial Mechanics and Dynamical Astronomy* 116 (1 2013), pp. 79–95. DOI: 10.1007/s10569-013-9480-0.

[34] Elisa Maria Alessi et al. "The H2020 project ReDSHIFT: overview, first results and perspective". In: *7th European Conference on Space Debris, June 2017*. June 2017.

[35] Henri Andoyer. "Memoires et observations. Contribution à la théorie des petites planètes dont le moyen mouvement est sensiblement double de celui de Jupiter". In: *Bulletin Astronomique, Serie I* 20 (1902), pp. 321–356.

[36] Jacques Henrard and A. Lemaitre. "A second fundamental model for resonance". In: *Celestial Mechanics* 30 (1983), pp. 197–218. DOI: 10.1007/BF01234306.

[37] Sławomir Breiter. "Extended fundamental model of resonance". In: *Celestial Mechanics and Dynamical Astronomy* 85 (2003), pp. 209–218. DOI: 10.1023/A:1022569419866.

[38] Sławomir Breiter. "Lunisolar resonances revisited". In: *Celestial Mechanics and Dynamical Astronomy* 81 (1-2 2001), pp. 81–91. ISSN: 09232958. DOI: 10.1023/A:1013363221377.

[39] Alessandra Celletti and Cătălin B. Galeş. "A Study of the Lunisolar Secular Resonance (Formula presented.)" In: *Frontiers in Astronomy and Space Sciences* 3 (Mar. 2016). ISSN: 2296987X. DOI: 10.3389/fspas.2016.00011.

[40] O. Winter and C. Murray. "Resonance and chaos: I. First-order interior resonances". In: *Astronomy and Astrophysics* 319 (Feb. 1997), pp. 290–304. URL: https://adsabs.harvard.edu/full/1997A&A...319..290W.

[41] Othon Cabo Winter and Carl D. Murray. "Resonance and chaos: II. Exterior resonances and asymmetric libration". In: *Astronomy and Astrophysics* 328 (1997), pp. 399–408. URL: https://ui.adsabs.harvard.edu/abs/1997A&A...319..290W.

[42] C. Beaugé, S. J. Aarseth, and S. Ferraz-Mello. "Resonance capture and the formation of the outer planets". In: *Monthly Notices of the Royal Astronomical Society* 270.1 (Sept. 1994), pp. 21–34. ISSN: 0035-8711. DOI: 10.1093/mnras/270.1.21. eprint: https://academic.oup.com/mnras/article-pdf/270/1/21/3888688/mnras270-0021.pdf. URL: https://doi.org/10.1093/mnras/270.1.21.

[43] Ioannis Gkolias, Martin Lara, Camilla Colombo, et al. "An ecliptic perspective for analytical satellite theories". In: *Advances in the Astronautical Sciences* 167 (2018), pp. 337–351.

[44] Marielle M. Pellegrino, Daniel J. Scheeres, and Brett J. Streetman. "Characterizing doubly-averaged dynamical models in medium earth orbit". In: *Acta Astronautica* 194 (2022), pp. 126–144. ISSN: 0094-5765. DOI: https://doi.org/10.1016/j.actaastro.2021.12.057. URL: https://www.sciencedirect.com/science/article/pii/S0094576521007037.

[45] Martin Lara et al. "Long-term evolution of Galileo operational orbits by canonical perturbation theory". In: *Acta Astronautica* 94 (2 2014), pp. 646–655. ISSN: 00945765. DOI: 10.1016/j.actaastro.2013.09.008.

[46] Alessandra Celletti, Catalin Gales, and Giuseppe Pucacco. "Bifurcation of lunisolar secular resonances for space debris orbits". In: *SIAM Journal on Applied Dynamical Systems* 15.3 (2016), pp. 1352–1383. DOI: 10.48550/arXiv.1512.0217+.

[47] Camilla Colombo, Francesca Scala, and Ioannis Gkolias. "Surfing in the phase space of Earth Oblateness and third body perturbations". In: *29th AAS/AIAA Space Flight Mechanics Meeting, Kaanapali, Maui, HI, USA, Jan 13-17, 2019*. Jan. 2019. ISBN: 9780877036593.

[48] Anne Lemaitre. *Resonances: Models and Captures. Lect. Notes Phys.* Ed. by Jean J. Souchay and Rudolf Dvorak. Vol. 790. Springer Berlin Heidelberg, 2010, pp. 1–62. ISBN: 978-3-642-04457-1. DOI: 10.1007/978-3-642-04458-8. URL: http://link.springer.com/10.1007/978-3-642-04458-8.

[49] P.M. Cincotta, C.M. Giordano, and C. Simó. "Phase space structure of multidimensional systems by means of the mean exponential growth factor of nearby orbits". In: *Physica D: Nonlinear Phenomena* 182.3 (2003), pp. 151–178. ISSN: 0167-2789. DOI: https://doi.org/10.1016/S0167-2789(03)00103-9. URL: https://www.sciencedirect.com/science/article/pii/S0167278903001039.

[50] S. Breiter, I. Wytrzyszczak, and B. Melendo. "Long-term predictability of orbits around the geosynchronous altitude". In: vol. 35. Elsevier Ltd, 2005, pp. 1313–1317. DOI: 10.1016/j.asr.2005.02.033.

[51] Daniel Casanova, Anne Lemaitre, and Alexis Petit. *AAS 15-236 Analysis of the evolution of space debris through a synthetic population*. DOI: 10.1007/s10569-015-9644-1.

[52] S. Valk et al. "Global dynamics of high area-to-mass ratios GEO space debris by means of the MEGNO indicator". In: *Advances in Space Research* 43 (May 2009), pp. 1509–1526. DOI: 10.1016/j.asr.2009.02.014.

[53] Alessandra Celletti, Giuseppe Pucacco, and Tudor Vartolomei. "Proper elements for space debris". In: *Celestial Mechanics and Dynamical Astronomy* 134.2 (Mar. 2022). DOI: 10.1007/s10569-022-10064-w. URL: https://doi.org/10.10072Fs10569-022-10064-w.

[54] Alessandra Celletti et al. "Dynamical models and the onset of chaos in space debris". In: *International Journal of Non-Linear Mechanics* 90 (Apr. 2017). DOI: 10.1016/j.ijnonlinmec.2016.12.015.

[55] Alessandra Celletti and Catalin Gales. "Dynamical investigation of minor resonances for space debris". In: *Celestial Mechanics and Dynamical Astronomy* (Apr. 2015). DOI: 10.1007/s10569-015-9636-1.

[56] L. Anselmo and C. Pardini. "Dynamical evolution of high area-to-mass ratio debris released into GPS orbits". In: *Advances in Space Research* 43.10 (2009), pp. 1491–1508. ISSN: 0273-1177. DOI: https://doi.org/10.1016/j.asr.2009.01.017. URL: https://www.sciencedirect.com/science/article/pii/S0273117709000635.

[57] Yue Wang, Xuhui Luo, and Xiaojie Wu. "Long-term evolution and lifetime analysis of geostationary transfer orbits with solar radiation pressure". In: *Acta Astronautica* 175 (2020), pp. 405–420. ISSN: 0094-5765. DOI: https://doi.org/10.1016/j.actaastro.2020.06.007. URL: https://www.sciencedirect.com/science/article/pii/S0094576520303635.

[58] Alessandra Celletti and Cătălin Galeş. "On the Dynamics of Space Debris: 1:1 and 2:1 Resonances". In: *Journal of Nonlinear Science* 24.6 (Sept. 2014), pp. 1231–1262. DOI: 10.1007/s00332-014-9217-6. URL: https://doi.org/10.1007%2Fs00332-014-9217-6.

[59] Alessandra Celletti and Cătălin Galeş. "A study of the main resonances outside the geostationary ring". In: *Advances in Space Research* 56.3 (2015). Advances in Asteroid and Space Debris Science and Technology - Part 1, pp. 388–405. ISSN: 0273-1177. DOI: https://doi.org/10.1016/j.asr.2015.02.012. URL: https://www.sciencedirect.com/science/article/pii/S0273117715001234.

[60] J Henrard. "Capture into resonance: an extension of the use of adiabatic invariants". In: *Celestial Mechanics* 27 (1982), pp. 3–22. DOI: 10.1007/BF01228946.

[61] C. Lhotka, A. Celletti, and C. Galeş. "Poynting–Robertson drag and solar wind in the space debris problem". In: *Monthly Notices of the Royal Astronomical Society* 460.1 (Apr. 2016), pp. 802–815. ISSN: 0035-8711. DOI: 10.1093/mnras/stw927. eprint: https://academic.oup.com/mnras/article-pdf/460/1/802/13773028/stw927.pdf. URL: https://doi.org/10.1093/mnras/stw927.

[62] R S Gomes. "Resonance trapping and evolution of particles subject to Poynting-Robertson drag: adiabatic and non-adiabatic approaches". In: *Celestial Mech Dyn Astr* 61 (1995), pp. 97–113. DOI: 10.1007/BF00051690.

[63] Alexander J. Mustill and Mark C. Wyatt. "A general model of resonance capture in planetary systems: first- and second-order resonances". In: *Monthly Notices of the Royal Astronomical Society* 413 (1 2011), pp. 554–572. DOI: 10.1111/j.1365-2966.2011.18201.x.

[64] Konstantin Batygin. "Capture of Planets Into Mean Motion Resonances and the Origins of Extrasolar Orbital Architectures". In: *arXiv: Earth and Planetary Astrophysics* (2015). DOI: 10.1093/MNRAS/STV1063.

[65] Alessandra Celletti and Cătălin Galeş. "Dynamics of Resonances and Equilibria of Low Earth Objects". In: *SIAM Journal on Applied Dynamical Systems* 17.1 (2018), pp. 203–235. DOI: 10.1137/17M1118671. eprint: https://doi.org/10.1137/17M1118671. URL: https://doi.org/10.1137/17M1118671.

[66] A. Bade et al. "Breakup model update at nasa/jsc". In: (Jan. 2000), pp. 125–138.

[67] N.L. Johnson et al. "NASA's new breakup model of evolve 4.0". In: *Advances in Space Research* 28.9 (2001), pp. 1377–1384. ISSN: 0273-1177. DOI: https://doi.org/10.1016/S0273-1177(01)00423-9. URL: https://www.sciencedirect.com/science/article/pii/S0273117701004239.

[68] Stefan Frey and Camilla Colombo. "Transformation of satellite breakup distribution for probabilistic orbital collision hazard analysis". In: *Journal of Guidance, Control, and Dynamics* 44 (1 2021), pp. 88–105. ISSN: 15333884. DOI: 10.2514/1.G004939.

[69] Ioannis Gkolias and Camilla Colombo. "Towards a sustainable exploitation of the geosynchronous orbital region". In: *Celestial Mechanics and Dynamical Astronomy* 131 (4 2019). DOI: 10.1007/s10569-019-9895-3.

[70] Elisa Maria Alessi et al. "Solar Radiation Pressure Resonances in Low Earth Orbits". In: *Monthly Notices of the Royal Astronomical Society* 473 (Oct. 2017), pp. 2407–2414. DOI: 10.1093/mnras/stx2507.

[71] Volker Schaus et al. "On the practical exploitation of perturbative effects in low Earth orbit for space debris mitigation". In: *Advances in Space Research* 63.7 (2019), pp. 1979–1991. DOI: 10.1016/j.asr.2019.01.020.

[72] Camilla Colombo. *Planetary orbital dynamics (PlanOdyn) suit for long term propagation in perturbed environment.* URL: https://indico.esa.int/event/111/contributions/340/.

[73] Camilla Colombo. "Long-Term Evolution of Highly-Elliptical Orbits: Luni-Solar Perturbation Effects for Stability and Re-entry". In: *Frontiers in Astronomy and Space Sciences* 6 (July 2019). ISSN: 2296987X. DOI: 10.3389/fspas.2019.00034.

[74] Charlotte Lcking, Camilla Colombo, and Colin R. McInnes. "A passive satellite deorbiting strategy for medium earth orbit using solar radiation pressure and the J 2 effect". In: *Acta Astronautica* 77 (2011), pp. 197–206. DOI: 10.1016/j.actaastro.2012.03.026.

[75] Camilla Colombo, Charlotte Bewick, and Colin McInnes. "Orbital dynamics of high area-to-mass ratio spacecraft with J2 and solar radiation pressure for novel Earth observation and communication services". In: *Acta Astronautica* 81 (Dec. 2012), pp. 137–150. DOI: 10.1016/j.actaastro.2012.07.009.

[76] Charlotte Lucking, Camilla Colombo, and Colin McInnes. "Solar radiation pressure augmented deorbiting from high altitude sun-synchronous orbits". In: *4S Symposium 2012, Small Satellites Systems and Services*. SVN, June 2012. URL: https://strathprints.strath.ac.uk/41241/.

[77] Charlotte Lücking, Camilla Colombo, and Colin McInnes. "A passive de-orbiting strategy for high altitude CubeSat missions using a deployable reflective balloon". In: *8th IAA Symposium on Small Satellites*. Winner of best paper award. DEU, Apr. 2011. URL: https://strathprints.strath.ac.uk/41233/.

[78] Charlotte Lücking, Camilla Colombo, and Colin R. McInnes. "Solar radiation pressure-augmented deorbiting: Passive end-of-life disposal from high-altitude orbits". In: *Journal of Spacecraft and Rockets* 50 (6 2013), pp. 1256–1267. ISSN: 15336794. DOI: 10.2514/1.A32478.

[79] Cecilia Giovannini and Camilla Colombo. "Master thesis : Solar sail strategies for satellite's direct and modulating deorbiting". In: Feb. 2019, p. 124.

[80] Elisa Maria Alessi et al. "Natural highways for end-of-life solutions in the LEO region". In: *Celestial Mechanics and Dynamical Astronomy* 130 (Apr. 2018). DOI: 10.1007/s10569-018-9822-z.

[81] G. Schettino et al. "Exploiting dynamical perturbations for the end-of-life disposal of spacecraft in LEO". In: *Astronomy and Computing* 27 (2019), pp. 1–10. ISSN:

2213-1337. DOI: https://doi.org/10.1016/j.ascom.2019.02.001. URL: https://www.sciencedirect.com/science/article/pii/S2213133718300945.

[82] Francesca Scala, Camilla Colombo, and Ioannis Gkolias. "Design of disposal orbits for high altitude spacecraft with a semi-analytical model". In: Feb. 2019.

[83] David G. Simpson. "An alternative lunar ephemeris model for on-board flight software use". In: *Flight Mechanics Symposium* (1999), p. 175. URL: https://ui.adsabs.harvard.edu/abs/1999flme.symp..175S.

[84] O. Montenbruck and E. Gill. *Satellite Orbits: Models, Methods, and Applications*. Physics and astronomy online library. Springer Berlin Heidelberg, 2000. ISBN: 9783540672807. URL: https://books.google.it/books?id=hABRnDlDkyQC.

[85] J.R. Dormand and P.J. Prince. "A family of embedded Runge-Kutta formulae". In: *Journal of Computational and Applied Mathematics* 6.1 (1980), pp. 19–26. ISSN: 0377-0427. DOI: https://doi.org/10.1016/0771-050X(80)90013-3. URL: https://www.sciencedirect.com/science/article/pii/0771050X80900133.

[86] J. Verner. "Numerically optimal Runge-Kutta pairs with interpolants". In: *Numerical Algorithms* 53 (Mar. 2010), pp. 383–396. DOI: 10.1007/s11075-009-9290-3.

[87] Charles H. Acton. "Ancillary data services of NASA's Navigation and Ancillary Information Facility". In: *Planetary and Space Science* 44.1 (1996). Planetary data system, pp. 65–70. ISSN: 0032-0633. DOI: https://doi.org/10.1016/0032-0633(95)00107-7. URL: https://www.sciencedirect.com/science/article/pii/0032063395001077.

[88] SAIC admin@space-track.org. *Space-Track.org*. URL: https://www.space-track.org/.

[89] SAIC connectbycnes.fr. *stelacnes*. URL: https://www.connectbycnes.fr/en/stela.

[90] Davide Amato, Aaron Rosengren, and Claudio Bombardelli. "THALASSA: a fast orbit propagator for near-Earth and cislunar space". In: *Space Situational Awareness, Orbital Debris, and Conjunction Analysis I, AIAA 2018-1970*. Jan. 2018. DOI: 10.2514/6.2018-1970.

[91] H. Andoyer. "Mémoires et observations. Contribution à la théorie des petites planètes dont le moyen mouvement est sensiblement double de celui de Jupiter". In: *Bulletin Astronomique, Serie I* 20 (Apr. 2023), pp. 321–356.

[92] K. Vogtmann, A. Weinstein, and V.I. Arnol'd. *Mathematical Methods of Classical Mechanics*. Graduate Texts in Mathematics. Springer New York, 1997. ISBN: 9780387968902. DOI: 10.1007/978-1-4757-1693-1. URL: https://books.google.it/books?id=Pd8-s6r0t%5C_cC.

[93] M. Guardia, T.M. Seara, and M.A. Teixeira. "Generic bifurcations of low codimension of planar Filippov Systems". In: *Journal of Differential Equations* 250.4 (2011), pp. 1967–2023. ISSN: 0022-0396. DOI: https://doi.org/10.1016/j.jde.2010.11.016. URL: https://www.sciencedirect.com/science/article/pii/S0022039610004456.

[94] V.I. Arnold et al. *Dynamical Systems V: Bifurcation Theory and Catastrophe Theory*. Encyclopaedia of mathematical sciences. Springer Berlin Heidelberg, 2013. ISBN: 978-3-642-57884-7. URL: https://books.google.it/books?id=8-LtCAAAQBAJ.

[95] Sadovskiĭ and Delos. "Bifurcation of the periodic orbits of Hamiltonian systems: An analysis using normal form theory." In: *Physical review. E, Statistical physics, plasmas, fluids, and related interdisciplinary topics* 54 2 (1996), pp. 2033–2070. DOI: https://doi.org/10.1103/PhysRevE.54.2033.

[96] Yue Wang, Xuhui Luo, and Xiaojie Wu. "Long-term evolution and lifetime analysis of geostationary transfer orbits with solar radiation pressure". In: *Acta Astronautica* 175 (Oct. 2020), pp. 405–420. DOI: 10.1016/j.actaastro.2020.06.007.

[97] Eugene G. Stansbery et al. "A Comparison of Catastrophic On-Orbit Collisions". In: *Proceedings of the Advanced Maui Optical and Space Surveillance Technologies Conference, held in Wailea, Maui, Hawaii, September 17-19, 2008, Ed.: S. Ryan, The Maui Economic Development Board., id.E50*. 2008. URL: https://ui.adsabs.harvard.edu/abs/2008amos.confE..50S.

[98] Jean H. Meeus. *Astronomical Algorithms*. Willmann-Bell, Incorporated, 1991. ISBN: 0943396352.